MEDIEVAL SEISMICITY ON THE HIMALAYAN FRONTAL THRUST FAULT AT LAL DHANG, UTTARAKHAND, INDIA

A DISSERTATION IN
Geosciences
and
Chemistry

Presented to the Faculty of the University
of Missouri-Kansas City in partial fulfillment of
the requirements for the degree

DOCTOR OF PHILOSOPHY

by
ROBYN L. DANIELS

B.S., University of Missouri-Kansas City, 2014

Kansas City, Missouri
2019

MEDIEVAL SEISMICITY ON THE HIMALAYAN FRONTAL THRUST FAULT AT LAL DHANG, UTTARAKHAND, INDIA

Robyn L. Daniels, Candidate for the Doctor of Philosophy Degree

University of Missouri-Kansas City, 2019

ABSTRACT

The Himalayan Frontal Thrust Fault (HFT) lies at the active, tectonic boundary between Eurasia and the Indian subcontinent. Continuous convergence between the landmasses causes strain to accumulate on the fault, which is intermittently released during seismic events. Throughout the last two centuries, several large-magnitude earthquakes have occurred on the HFT without producing measurable vertical offsets at the ground surface, leading many to refer to these events as blind-thrust earthquakes. However, large fault scarps along the HFT indicate that past ruptures of the fault were not blind and may have been much greater in magnitude.

Recent paleoseismological studies have aimed to characterize the earthquakes that generated these features. One of these studies focused on defining the seismic parameters of a specific segment of the fault by comparing findings across several sites, including the site of Lal Dhang in Uttarakhand, India. The results of this study point to lingering uncertainties

specific to the site of Lal Dhang that warrant additional research, including poor temporal constraint of past fault ruptures, disparities in deformational structures when compared to surrounding sites, discrepancies in fault scarp height as compared to apparent net slip measurements, and questions surrounding local interactions between fluvial terrace development and fault scarp generation.

The goal of this research was to conduct a comprehensive and detailed analysis of the seismic history at the site of Lal Dhang. The work was distributed across three intersecting objectives: 1) development of an age model for previous earthquakes on the segment of the HFT that includes Lal Dhang, 2) determination of the faulting sequence, timing, and seismic parameters of previous earthquakes at the site, and 3) investigation of the interaction between local tectonic and fluvial landscape development. Data produced through this study have narrowed the constraint on rupture timing at the site of Lal Dhang and along the western section of the CSG. Results presented here include improved estimates for coseismic slip and vertical separation at the site of Lal Dhang, which are comparable to surrounding sites, and a model for local fault scarp generation and associated landscape development. Implications for future research are considered and discussed.

APPROVAL PAGE

The faculty listed below, appointed by the Dean of the School of Graduate Studies, have examined a dissertation titled "Medieval Seismicity on the Himalayan Frontal Thrust Fault at Lal Dhang, Uttarakhand, India," presented by Robyn L. Daniels, candidate for the Doctor of Philosophy degree, and certify that in their opinion it is worthy of acceptance.

Supervisory Committee

Tina M. Niemi, Ph.D., Committee Chair
Department of Geosciences

Kathleen V. Kilway, Ph.D., Co-discipline Advisor
Department of Chemistry

James B. Murowchick, Ph.D.
Department of Geosciences

Jejung Lee, Ph.D.
Department of Geosciences

J. David Van Horn, Ph.D.
Department of Chemistry

CONTENTS

ILLUSTRATIONS

ACKNOWLEDGMENTS

This research would not have been possible without support received from so many, whether that support was logistical, financial, or academic. Thanks to the University of Missouri-Kansas City (UMKC): Office of Research, School of Graduate Studies, College of Arts & Sciences, and Department of Geosciences for providing funding for various aspects of this project. The Office of Research provided financial assistance to the project through a generous grant to my Committee Chair and Advisor, Tina M. Niemi. The School of Graduate Studies contributed funds to the project through three substantial Student Research Grants for the years 2015-2018, and also through several student travel grants in conjunction with the College of Arts & Sciences and the Department of Geosciences. These funds, in addition to travel grants received from the Geological Society of America and the National Science Foundation allowed for the presentation of this research at several professional meetings and conferences. Two Newcomb Student Research Awards through the UMKC Department of Geosciences were instrumental in funding the logistical aspects of this project, and a Graduate Teaching Assistant scholarship through the College of Arts & Sciences and the Department of Geosciences facilitated the completion of my program of study.

All work associated with this research was completed in collaboration with the Wadia Institute of Himalayan Geology (WIHG) in Dehradun, Uttarakhand, India. Thanks to the Director, WIHG, for financial and administrative support given to this project through the CAP Himalayan Institute Projects. Thanks also to the Disaster Mitigation and Management

Center of Uttarakhand, India, and its Executive Director, Piyoosh Rautela, for collaborating on this project and for providing critical logistical support during field campaigns. We are also very grateful to the Indian Forest Service for facilitating this research by permitting and overseeing excavation within the bounds of the National Forest, and for subsequent environmental restoration of excavated areas.

My sincere gratitude to the faculty and students from UMKC and WIHG that assisted on this project, which include: Professors R. Jayangondaperumal and P. Srivastava from WIHG, Professor Tina M. Niemi from UMKC, Lauren Murphy, Kaylee Thomas, Arjun Pandey, A. Aravind, and Atul Agnihotri, and to the many local workers and drivers that assisted us daily during field campaigns. Special thanks to Tina M. Niemi, my Committee Chair and Advisor, for her endless academic, professional, and emotional support throughout my time at UMKC. The members of my doctoral committee, Professors Tina M. Niemi, Kathleen V. Kilway, James B. Murowchick, Jejung Lee, and J. David Van Horn are some of the most supportive, encouraging, helpful and generally remarkable people, and I am grateful that I was able to learn under their leadership. I couldn't have done it without your guidance.

Thank you all very much.

DEDICATION

This dissertation is dedicated to my friends and family, who offered endless support as I conducted this research. Special appreciation is owed to my husband, Michael, and to my children, Lacey, Kelsey, Brady and Drake, who light up my life daily.

All my love…

CHAPTER 1

INTRODUCTION

The Himalayan Frontal Thrust Fault (HFT) is the youngest and southernmost member of a thrust fault complex that strikes approximately northwest-southeast at the tectonic boundary between Eurasia and the Indian subcontinent. The fault system forms an arc along the compressional boundary between the two land masses, where collision first occurred in the Paleogene, approximately 50 Ma. Strain resulting from collision has led to the uplift of the Himalaya, and the concomitant development of the southward propagating thrust fault system, which accommodates approximately half of the 45 mm/yr of total convergence (Ader et al., 2012). The fault zone consists of three, subparallel, northward-dipping, ~2500-km-long thrust faults along which the upper crust of the Indian plate has been folded and fractured along its northern margin and forced southward due to collision with the Eurasian landmass. Continuous convergence has resulted in recurrent episodes of thrust fault displacement, producing an extensive orogenic wedge that expands southward above the crystalline basement of the Indian plate. The zone comprises, from oldest to youngest and from north to south, the Main Central Thrust Fault (MCT), the Main Boundary Thrust Fault (MBT) and the HFT. The faults are in sequence, meaning that they young toward the foreland, with the active boundary located at the foremost fault and the older faults becoming dormant in a progressive succession from the hinterland toward the foreland. The MCT, MBT and HFT are connected in the subsurface along a common, basal detachment called the Main

Himalayan Thrust Fault (MHT), which marks the boundary between the Eurasian and Indian crustal masses at depth (Zhang & Klemperer, 2010).

Individual earthquakes on the HFT are limited to segments of the fault that can measure up to hundreds of kilometers in length. Over the last two centuries, several large magnitude earthquakes have occurred on segments of the fault and are referenced in the earthquake catalogues (e.g., Ambraseys, 2000; Ambraseys & Douglas, 2004; Iyengar, Sharma, & Siddiqui, 1999; Khattri, 1987; Pant, 2002). However, these ruptures have not produced substantial vertical offsets at the ground surface, leading many to refer to these events as "blind-thrust earthquakes". The generation of large fault scarps during previous earthquakes on the HFT provides evidence that earlier ruptures were not blind and may have been much greater in magnitude, indicating a change in seismic behavior over time that has fueled much scientific interest and inquiry. Segments that have not experienced a recent great magnitude ($M_w \geq 8.0$) earthquake, signaling a potential for impending rupture, are of particular scientific significance. In these areas, known as seismic gaps, paleoseismological studies are conducted for investigation of the nature and timing of the most recent great earthquake (MRE) on each associated fault segment. The data generated during these investigations provide evidence used to describe the seismic parameters of previous large-magnitude earthquakes, and to inform projections for the expected areal extent, magnitude and recurrence intervals of future ruptures. Because the HFT lies at the base of the Himalaya, and at the edge of the fertile Indo-Gangetic plain, the surrounding area is home to some of the most concentrated human populations in the world and therefore proper seismic hazard

assessment and risk management are critical, especially when consideration is given to the rudimentary construction techniques practiced within the region.

Previous Studies

Several paleoseismological studies have recently been conducted along the section of the HFT known as the Central Seismic Gap (CSG) (Kumahara & Jayangondaperumal, 2013; Kumar et al., 2001; Kumar et al., 2006; Malik et al., 2010; Rajendran, John, & Rajendran, 2015). This is the segment of the fault in north-central India and western Nepal that lies between the areas affected by the 1905 CE Kangra (Himachal Pradesh, India) and 1934 CE Nepal-Bihar earthquakes (Khattri, 1987). Investigations have been concentrated in this area due to lack of a great 20th century rupture, an increase in microseismicity over the last several decades, and the prevalence of large fault scarps that suggest significant coseismic slip in past events. In 2006, Kumar et al. published a paleoseismological study that included six sites along the western section of the CSG, including the site of Lal Dhang in the state of Uttarakhand, India. The study evaluated geomorphological and paleoseismological evidence for the MRE at each location and compared the data across the sites, with the goal of identifying trends and correlations for the western section of the CSG. Kumar et al.'s (2006) conclusions point to a $M_w \geq 8.0$ earthquake on this segment of the fault near the turn of the 15th century, followed by a hiatus in great ruptures extending to the present day. However, due to a lack of radiocarbon samples collected from deposits capping the fault strands, some question remains regarding the age of the overlying sediments and therefore the timing of the MRE identified in the study. It is also unclear whether the large fault scarps and associated net slip measurements along this segment of the HFT can be attributed to one megathrust

earthquake approaching M_w 9.0, or if these offsets are cumulative over more than one event. Refining estimates of seismic potential based on data from previous ruptures is particularly critical for this segment of the CSG if the most recent, great rupture occurred over 600 years ago, as suggested in the study. If these ages are accurate, another large-scale event may be imminent, as a recurrence interval of approximately 680 years has been estimated for great earthquakes on the eastern segment of the CSG in western Nepal (Mugnier et al., 2013; Sapkota et al., 2013).

The 2006 study by Kumar et al. laid important groundwork for refining our understanding of the seismic history for this segment of the HFT. This investigation aimed to build upon those findings, by taking a closer look at a specific site included in that study. Focusing the research on a single location allowed us to develop a comprehensive understanding of the nature of the MRE on this segment of the fault through the evaluation and synthesis of local geomorphological, structural and paleoseismological data. Throughout this investigation, additional data on the timing, scale and recurrence of earthquakes at the site of Lal Dhang has been generated, which has helped to address remaining uncertainties surrounding the timing and magnitude of the MRE for this section of the CSG. The methods employed in this study may become a model for the analysis of data collected at other sites along the same fault segment and could potentially apply to adjacent fault segments and beyond. Additionally, because the conclusions of this inquiry support those of the previous study, we have demonstrated the reproducibility of paleoseismological findings in the region, which has proven difficult at other sites on this segment of the fault.

OxCal Age Model

Initial research was centered on the development of an age model for the MRE in the western section of the CSG using the OxCal (Bronk Ramsey, 2009a) software program. The model is based on previously published radiocarbon data for several paleoseismic trench sites on this segment of the HFT. Kumar et al. (2006) determined probable date ranges for the MRE at five sites along the CSG based on the calibrated ages of detrital charcoal samples collected from stratigraphic units that pre-date and post-date the event horizon. The authors then used the overlap of these probable date ranges to narrow the probability of earthquake occurrence on this segment of the fault to the turn of the 15th century. However, this method neglects to consider the probability density associated with any specific time interval included in the probability distribution functions (PDFs) for the calibrated radiocarbon ages of the charcoal samples. Modeling with OxCal has provided improved temporal constraint of the MRE through the application of Bayesian statistical principles to the analysis of the PDFs of the individual radiocarbon sample ages, with respect to the sequential stratigraphic information obtained during the paleoseismological investigations. The resultant model provides a PDF for the timing of the MRE at each site, which can be compared with those of other sites along the CSG. Development of an OxCal age model has allowed for improved accuracy in the analysis of the probable date range for the MRE in the western section of the CSG and has indicated potential areas that may represent segment boundaries. This aspect of the research is critical in establishing an accurate framework by which to evaluate the conclusions of previous studies, and to analyze the findings of current and future investigations on this segment of the fault.

Paleoseismological Investigation

The seismic history of the HFT at the site of Lal Dhang in Uttarakhand, India (site 5 in the Kumar et al., 2006 study) was the focus of this investigation. The site of Lal Dhang was selected for several reasons that are associated with uncertainties surrounding the findings reported in the Kumar et al., 2006 study. These include a relatively wide date range reported by the authors for timing of past earthquakes at the site, a discrepancy between scarp height and net slip measurement identified by the authors, and the observation that the paleoseismic trench log depicted in the study for the site of Lal Dhang displays disparate deformational structures compared to the trench logs for sites that bound Lal Dhang to the east and the west. An important aspect of this research was to determine whether an explanation for these apparent incongruities might be established. In order to achieve these goals, a field investigation was conducted at the site, which included a topographic site survey, and the excavation and interpretation of a paleoseismic trench.

To begin the site investigation, an initial topographic survey of the ~10-m-high fault scarp, and the surrounding area that includes several stages of fluvial terraces associated with the adjacent Rawasan River, was completed using a Real Time Kinematic Global Positioning System for generation of an accurate topographic map and scarp profile. Test pits of approximately $1m^3$ were then excavated on the terrace surfaces and samples of charcoal and sand, where present, were collected from these pits for dating by AMS (C-14) and Optically Stimulated Luminescence (OSL), respectively, in order to determine the approximate timing of deposition and/or abandonment of each of these surfaces. Excavation of a large, paleoseismic trench across the fault scarp, at a location adjacent to the trench in the 2006

study followed. A thorough analysis of trench stratigraphy and associated deformational structures was completed, including determination of possible faulting scenarios and estimation of coseismic slip. Detrital charcoal and OSL samples were collected from strategic locations within the trench to determine both the absolute timing of faulting and folding at this location on the HFT, and how that timing fits into the sequence of earthquakes referenced in the literature. Analysis of the data followed, and results were compared to previous findings and to the OxCal age model in order to evaluate congruities and disparities in reference to previous studies.

Landscape Development

Development of the Himalayan orogenic wedge has modified regional drainage patterns, causing rivers and streams to cut paths across the mountain belt and debouche onto the Indo-Gangetic plain. As uplift occurs along the southern edge of the mountain belt, rivers and streams are captured behind new topographic highs where they run approximately parallel to the front before downcutting at a high angle to the scarp front, which is the current southern bound of the Sub-Himalayan range. This process produces natural outcrops where deformational structures, including faults, can be viewed without need for extensive excavation. This provides important information on the seismic history of an area, but also increases complexity in analyzing the geomorphology of sites along the HFT where fluvial terraces and fault scarps coexist. Because the areas that are undergoing tectonic deformation are composed of Quaternary sediments in a foreland basin that were deposited by fluvial systems, it is critical to understand the processes and mechanisms by which these forces interact. Therefore, the final objective of this research was to evaluate the history of fluvial

terrace development as it relates to earthquake occurrence and fault scarp generation at the site of Lal Dhang. In order to achieve this end, a detailed, local geomorphological study was conducted to determine the relationship between fluvial terrace development and fault scarp generation at the site, and a fault scarp generation model was developed through the synthesis of local geomorphological, paleoseismological, and structural findings. The model generated through this research may provide an important resource for future studies at other sites along the HFT with similar depositional settings and orientations to the remote stress field.

Interdisciplinary Aspects of the Research

Aspects of this research that incorporated the field of Chemistry include: 1) the chemical analysis of sediment samples for elemental distribution relating to quartz and feldspar fractions, for use in the correlation of units across deformational boundaries; and 2) the use of nuclear chemistry principles (AMS C-14 and OSL) to determine the age of samples, for use in local terrace studies and in the absolute dating of the MRE on this segment of the fault.

While paleoseismologists generally rely on parameters such as observed lithology, texture, color, etc., to identify corresponding stratigraphic units across fault contacts, the units involved in faulting at Lal Dhang and many other sites along the HFT are composed of unlithified fluvial and floodplain deposits that can be difficult to differentiate, especially in areas of deformation. These materials tend to respond to seismic events in a ductile manner, such as by folding, thinning, and stretching of the units, which can obscure stratigraphic contacts that would normally be preserved during the brittle failure of lithified materials. In

order to mitigate this potential source of error, this study incorporated chemical and physical analyses of the sediments using x-ray diffraction (XRD) and laser diffraction grain size analysis to determine if positive quantitative identification of the stratigraphic units could be achieved. The results indicate that chemical analysis by XRD was not useful in differentiating between the stratigraphic units due to a common source area and lack of any diagnostic difference in clay and quartz fractions. However, the results of the grain size analysis were distinctive across stratigraphic contacts, and therefore allowed for conclusive differentiation of the various units.

Techniques for dating sediments using OSL measurements were developed only recently (ca. 1985), and are continually improving. Many studies since that time have aimed to refine these techniques, both in general and in response to regional, geographic variables (i.e., Srivastrava & Misra, 2012). However, results of this technique for samples whose burial dates populate the lower and upper extremes of the effective range of OSL have been wrought with very large error margins, especially in areas where other problems such as incomplete bleaching in turbulent fluvial settings also exist. In this study, we dated materials that were transported in a fluvial setting, deposited, and then buried in the medieval period only hundreds of years ago. Unfortunately, the OSL samples in this study produced erroneously old depositional ages for the units, and error margins of several thousands of years. AMS (C14) dating of detrital charcoal provided superior accuracy and precision in dating the depositional age of sediments for the purposes of this study.

CHAPTER 2

A PALEOSEISMIC AGE MODEL FOR LARGE-MAGNITUDE EARTHQUAKES ON FAULT SEGMENTS OF THE HIMALAYAN FRONTAL THRUST IN THE CENTRAL SEISMIC GAP OF NORTHERN INDIA

Jayangondaperumal, R., Daniels, R.L., Niemi, T.M., (2017). A paleoseismic age model for large-magnitude earthquakes on fault segments of the Himalayan Frontal Thrust in the Central Seismic Gap of northern India. *Quaternary International*, 462, 130-137. http://dx.doi.org/10.1016/j.quaint.2017.04.008.

Abstract

Crustal collision between Eurasia and the Indian subcontinent has produced a thrust fault system that accommodates a share of the strain associated with convergence. The foremost of these faults is the Himalayan Frontal Thrust (HFT), also referred to as the Main Frontal Thrust (MFT). Discrete segments of the HFT have produced numerous, large-magnitude earthquakes throughout the last two centuries that are constrained through instrumental and historical records. Paleoseismic studies have established comparable constraint for pre-instrumental ruptures of the fault. The segment of the fault known as the Central Seismic Gap (CSG), which extends from North-Central India into Western Nepal, is of particular interest due to an apparent long-term quiescence that suggests the potential for impending large-scale rupture. Here we compile recent, paleoseismological findings from seven published trench sites into a coherent OxCal age model for large-magnitude ruptures along the CSG. Our results indicate that the western half of the CSG likely ruptured in the event corresponding to historical accounts of an earthquake in 1344 CE.

Introduction

The Himalayan thrust fault system lies at the active, tectonic boundary between Eurasia and the Indian subcontinent, and accommodates approximately half of the strain associated with convergence and the concomitant uplift of the Himalayan Mountain Range (Ader et al., 2012), which began in the middle to late Paleogene. The foremost in this series of in-sequence thrust faults, which connect across a common decollement (Figure 2.1) and are oriented transverse to convergence, is the Himalayan Frontal Thrust (HFT), also referred to as the Main Frontal Thrust (MFT). The southward-verging HFT dips to the north at ~20-45°, displacing Tertiary and Quaternary (Siwalik Group) sedimentary units from an earlier foreland basin over the Quaternary sediments of the Indo-Gangetic plain. Numerous large-magnitude earthquakes have ruptured discrete segments of this active boundary in the last two centuries, as referenced in earthquake catalogues (e.g., Ambraseys, 2000; Ambraseys & Douglas, 2004; Iyengar et al., 1999; Khattri, 1987; Pant, 2002).

Incomplete historical records and inferred rupture locations lead to uncertainties surrounding the timing and nature of earlier events, which can be addressed through paleoseismic investigation. The need for additional paleoseismological data is particularly critical along segments of the HFT that lack a large-scale 20th century rupture, such as the Central Seismic Gap (CSG), which lies between the areas affected by the 1905 CE Kangra (Himachal Pradesh, India) and 1934 CE Nepal-Bihar earthquakes (Khattri, 1987). Establishing the timing of past earthquakes along the CSG is critical in assessing regional seismic hazards for areas proximal to the HFT that have both large populations and inadequate infrastructures. While several paleoseismic studies have been conducted across

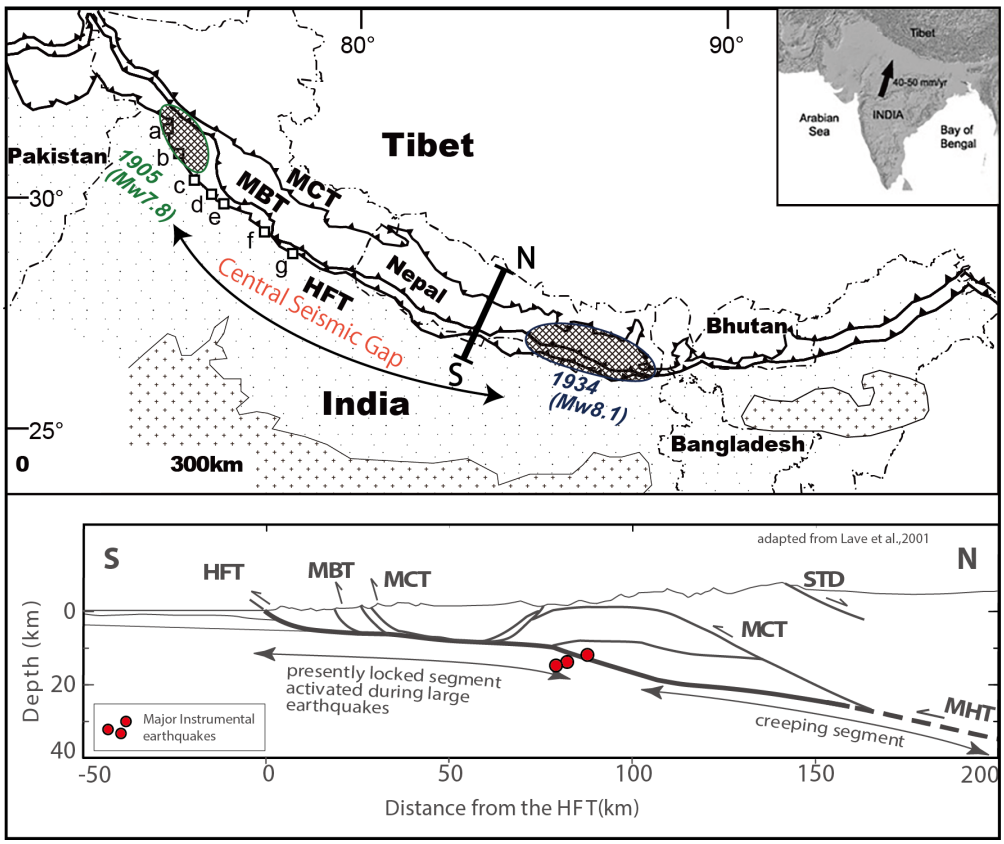

Figure 2.1: Map showing the major zones of Himalayan convergence—MCT: Main Central Thrust; MBT: Main Boundary Thrust; and HFT: Himalayan Frontal Thrust. Trench site locations are labeled as in Figure 2.2: a) Hajipur, b) Bhatpur, c) Chandigarh, d) Kala Amb, e) Rampur Ganda, f) Lal Dhang, g) Ramnagar. Schematic cross-section through central Nepal showing the main structures and instrumental thrust earthquake foci. STD: Southern Tibet Detachment; MHT: Main Himalayan Thrust; (after Lavé et al., 2001).

the HFT, along and adjacent to the CSG (Kumahara & Jayangondaperumal, 2013; Kumar et al., 2001; Kumar et al., 2006; Malik et al., 2010; Rajendran et al., 2015); a comprehensive analysis of the events interpreted in these studies has not previously been completed. In order to better constrain the timing of paleoearthquakes on the west-central, India section of the HFT, we have evaluated trench data and compiled recent radiocarbon age results from previously published studies for seven sites, including (from northwest to southeast):

Hajipur, Bhatpur, Chandigarh, Kala Amb, Rampur Ganda, Lal Dhang, and Ramnagar (Figure 2.1) (Kumahara & Jayangondaperumal, 2013; Kumar et al., 2001; Kumar et al., 2006; Malik et al., 2010; Rajendran et al., 2015). Review articles by Mugnier et al. (2013) and Bollinger, Tapponnier, Sapkota, and Klinger (2016) provided a synopsis of earthquakes along the central Himalaya and Nepal sections of the HFT, respectively. An age model was developed for each of the seven trench sites based on published radiocarbon results, with consideration given to the stratigraphic context of each trench, using the OxCal software program (Bronk Ramsey, 2009a) and the IntCal13 atmospheric calibration curve (Reimer et al., 2013).

Methods

Paleoseismic investigations of the HFT incorporate geomorphological analyses of fault scarps, calculation of local uplift rates, examination of faulting exposed in river cutbanks, excavation of paleoseismic trenches across fault scarps, etc. Trench sites are chosen based on several factors, such as: fault scarp geometry, orientation of fault scarps with relation to the direction of regional convergence and accessibility of the sites. The purpose of these excavations is to expose and document geological evidence of past ruptures of the fault, and to collect samples from strategic stratigraphic locations that will allow for dating of those ruptures.

The collection of charcoal samples for radiocarbon analysis is a common technique employed in paleoseismic studies to constrain the timing of past earthquakes, especially where these samples are abundant. However, dating and calibrating individual charcoal samples often results in "…probability distributions, which are often irregular and multimodal…"(Lienkaemper & Bronk Ramsey, 2009). Additionally, constraining the

minimum age of paleoseismic events on thrust faults using radiocarbon data can be problematic due to the potential for post-event erosion of fault scarps and associated reworking of charcoal from older units into colluvial deposits. This may result in erroneously old depositional ages for the stratigraphic units that directly overlie the faulted sediments. Modeling these data using a Bayesian statistical program (Bayes, 1763) such as OxCal, that incorporates stratigraphic relationships, can tighten the probability distributions of individual sample ages based on the constraint that samples from overlying layers are younger (Lienkaemper & Bronk Ramsey, 2009), and can increase the accuracy of results through the identification of outliers.

Here we use the OxCal "sequence" command to introduce a depositional chronology for the stratigraphic units, and the "phase" command to include all radiocarbon ages (BP) for an individual stratigraphic unit without consideration for chronological order within that unit. Resultant models are developed through an iterative process, which narrows the probability distribution functions (PDFs) for the ages of each of the calibrated samples and event horizons, and identifies outliers through assignment of an Agreement Index (AI). Here we follow the standard convention of including all radiocarbon age results with an AI $\geq$ 60% and removing all others as outliers (Bronk Ramsey, 2009b). Outliers are best identified when there are a sufficient number of additional data points, highlighting the importance of analyzing an ample number of C-14 samples in each OxCal model.

Employing a secondary dating technique such as Optically Stimulated Luminescence (OSL) can be beneficial for the verification of radiocarbon age results, and for mitigation of factors such as inherited ages of charcoal samples that may lead to overestimation of

depositional age. While OSL samples were collected for one of the trench sites in this study, this data is not included in the model due to a lack of availability across each of the sites. Additional considerations for the omission of OSL data from our model include disparities in the type of information that is garnered through radiocarbon and luminescence dating techniques, and the method by which the OxCal software program processes these types of data based on the input command method for each data type, among others. In order to create a cohesive, regional model for correlation of event(s) across multiple sites, the model presented here is based on comparable data from each site.

Various faulting patterns were observed across the trench sites, with some demonstrating in-sequence thrusting and others exhibiting out-of-sequence thrusting, or a combination of the two. Out-of-sequence thrust faulting is common in the Himalaya and has been shown to occur in other collisional tectonic settings, as well (Agard, Omrani, Jolivet, & Mouthereau, 2005; Castellarin & Cantelli, 2000; Mukherjee, 2015). It can be difficult to determine the faulting sequence when rupture of separate fault strands is believed to have occurred in the span of one event, with deformation of the same stratigraphic units across each strand. In such cases, the sequence is irrelevant to this study, which focuses only on the approximate timing of the rupture at each site. For trench sites where the stratigraphy was interpreted to suggest a multiple-event scenario, only the most recent fault strand with enough coseismic slip to indicate a large-magnitude rupture is included in this model, as this study is concerned with defining only the latest large-magnitude ruptures along this section of the HFT. The models are presented here, alongside published trench logs, in a panoptic illustration (Figure 2.2) that offers a coherent chronology for large-scale ruptures of the CSG.

Calendar date ranges at one- and two-sigma confidence intervals are shown adjacent to PDFs for earthquakes identified at each of the sites and vertical markers denoting dates of putative events in 1255 CE, 1344 CE, 1505 CE and 1555 CE are superimposed for comparison with the historical earthquake record.

Paleoseismic Data

Detailed descriptions of each of the paleoseismic trenches can be found in the original publications (Kumahara & Jayangondaperumal, 2013; Kumar et al., 2001; Kumar et al., 2006; Malik et al., 2010; Rajendran et al., 2015). Here we briefly summarize the original findings and present modeled radiocarbon age results for each of the trench sites, beginning with Hajipur (to the northwest of the CSG), and continuing eastward. Four stratigraphic units were identified in the trench at Hajipur (Malik et al., 2010), which measured approximately 18 m long, 2-2.5 m wide and 1-4.5 m deep. The oldest layer, Unit A, is a gravel layer with sand lenses. Unit B is a medium to coarse sand, and is the youngest faulted unit. Units A and B are thrust over Unit B in the footwall along a low-angle fault strand. Unit C is a colluvium layer of medium to coarse sand, and Unit D is interpreted as a channel-fill of medium to fine sand with occasional gravel-sized clasts. Units C and D cap the faulted sequence. Charcoal samples included in the model were collected from Unit B in the hanging wall (H5) and at the interface between Unit B in the footwall and the colluvium layer, Unit D (H2a). The age model gives a two-sigma confidence interval for the event occurring within the range of 1336 CE – 1771 CE, and a one-sigma confidence interval for occurrence in the range of 1406 CE – 1628 CE.

Figure 2.2: Evidence of paleoearthquakes at seven trench sites along the HFT based on published, paleoseismic trench data (Kumahara & Jayangondaperumal, 2013; Kumar et al., 2001; Kumar et al., 2006; Malik et al., 2010). NOTE: Trench logs for the Bhatpur and Kala Amb trench sites have been reversed for orientation consistent with other trench logs. One- and two-sigma confidence intervals are given for rupture dates at each site, alongside probability distribution functions developed from radiocarbon age results using the OxCal software program (Bronk Ramsey, 2009a). Vertical lines indicating dates of putative earthquakes in 1255 CE, 1344 CE, 1505 CE and 1555 CE are superimposed. Radiocarbon sample collection locations are shown on each trench log and trench sites are labeled alphabetically, corresponding to labeled locations in Figure 2.1.

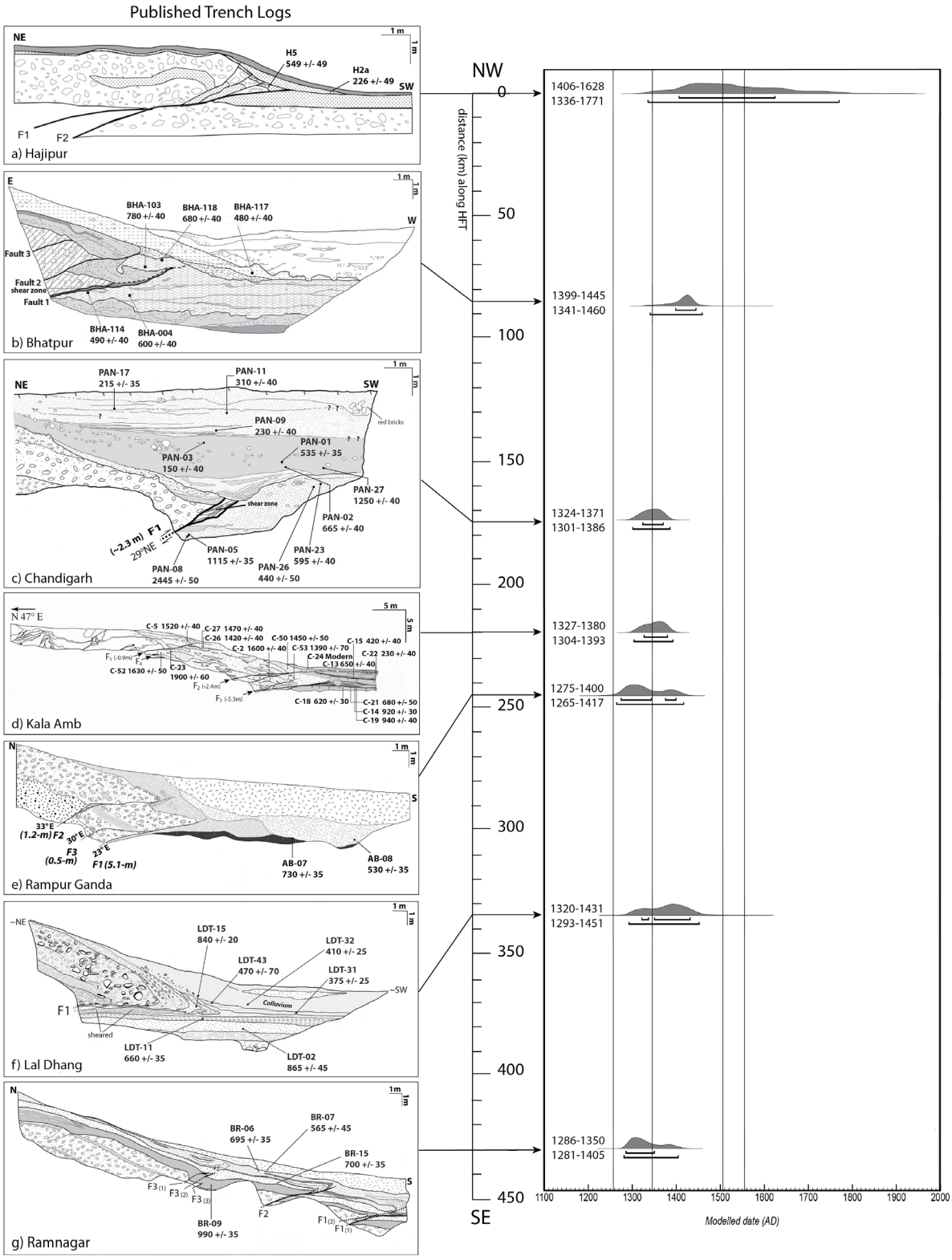
Published Trench Logs
NE
H5
549 +/- 49
H2a
226 +/- 49
SW
F1
F2
a) Hajipur
E
BHA-103
780 +/- 40
BHA-118
680 +/- 40
BHA-117
480 +/- 40
W
Fault 3
Fault 2
shear zone
Fault 1
BHA-114
490 +/- 40
BHA-004
600 +/- 40
b) Bhatpur
NE
PAN-17
215 +/- 35
PAN-11
310 +/- 40
SW
red bricks
PAN-09
230 +/- 40
PAN-01
535 +/- 35
PAN-03
150 +/- 40
PAN-27
1250 +/- 40
shear zone
PAN-02
665 +/- 40
(~2.3 m) F1
29°NE
PAN-05
1115 +/- 35
PAN-23
595 +/- 40
PAN-26
440 +/- 50
PAN-08
2445 +/- 50
c) Chandigarh
N 47° E
C-5 1520 +/- 40
C-27 1470 +/- 40
C-26 1420 +/- 40
C-50 1450 +/- 50
C-2 1600 +/- 40
C-53 1390 +/- 70
C-15 420 +/- 40
C-22 230 +/- 40
C-24 Modern
C-13 650 +/- 40
C-52 1630 +/- 50
C-23
1900 +/- 60
C-18 620 +/- 30
C-21 680 +/- 50
C-14 920 +/- 30
C-19 940 +/- 40
d) Kala Amb
N
S
33°E
(1.2-m)F2
30°E
F3
(0.5-m)
23°E
F1 (5.1-m)
AB-07
730 +/- 35
AB-08
530 +/- 35
e) Rampur Ganda
~NE
LDT-15
840 +/- 20
LDT-32
410 +/- 25
LDT-43
470 +/- 70
LDT-31
375 +/- 25
~SW
Colluvium
F1
sheared
LDT-11
660 +/- 35
LDT-02
865 +/- 45
f) Lal Dhang
N
BR-07
565 +/- 45
BR-06
695 +/- 35
BR-15
700 +/- 35
S
F3 (1)
F3 (2)
F3 (3)
F2
F1 (2)
F1 (1)
BR-09
990 +/- 35
g) Ramnagar
NW
SE
distance (km) along HFT
0
50
100
150
200
250
300
350
400
450
1406-1628
1336-1771
1399-1445
1341-1460
1324-1371
1301-1386
1327-1380
1304-1393
1275-1400
1265-1417
1320-1431
1293-1451
1286-1350
1281-1405
1100
1200
1300
1400
1500
1600
1700
1800
1900
2000
Modelled date (AD)

The Bhatpur trench (Kumahara & Jayangondaperumal, 2013), located approximately 85 km southeast of Hajipur and also to the northwest of the CSG, measured 22 m long and 5 m deep, and revealed six major stratigraphic units. The oldest of these, Unit 1, is a sandy, pebble-gravel. Unit 2 is also a sandy, pebble-gravel that is faulted in the hanging wall, and repeated as a sub-horizontal layer with some folding in the footwall. The base of Unit 2 is a fine-grained sand. Unit 3 is a sand and silt layer with gravel lenses, with interbedded, organic-rich layers that are interpreted to be buried paleosols. Units 1-3 are faulted and displaced over Unit 3 in the footwall. Units 4 and 5 are capping colluvium layers of a silty pebble-gravel, and a clayey silt with interspersed pebble-sized clasts, respectively. Unit 6 is interpreted as an active fan deposit. Four charcoal samples were collected from the faulted Unit 3 (BHA-004, BHA-103, BHA-114, and BHA-118) and one from the Unit 5 colluvium layer (BHA-117) that caps the event. The age model gives a two-sigma confidence interval for event occurrence in the range of 1341 CE – 1460 CE, and a one-sigma confidence interval for occurrence in the range of 1399 CE – 1445 CE.

The 40-m-long trench at Chandigarh (Kumar et al., 2006), located approximately 90 km southeast of the Bhatpur site, was excavated to a depth of 4-5 m. Seven major stratigraphic units were exposed in the excavation. Units 1-3 are gravel layers and Unit 4 is described as a sandy, silty clay. Units 1-4 are faulted and overlie Unit 4 in the footwall. Unit 5 is interpreted as a cut-and-fill channel that caps the fault strand, and Unit 6 is colluvium composed of silty sand deposits with interspersed, pebble- to cobble-sized clasts. Unit 7 is a young, overbank deposit of silty sand. Charcoal samples were collected from Unit 4 in the footwall (PAN-05, PAN-08, PAN-23, and PAN-26), from the Unit 6 colluvium layer (PAN-

01, PAN-02, PAN-03, and PAN-27), and from Unit 7 (PAN-09, PAN-11, and PAN-17). Samples PAN-11, PAN-26 and PAN-27 were removed from the model due to low AIs. The age model gives a two-sigma confidence interval for this rupture occurring in the range of 1301 CE – 1386 CE and a one-sigma confidence interval for occurrence in the range of 1324 CE – 1371 CE.

The trench at Kala Amb (also known as Black Mango) (Kumar et al., 2001), located about 45 km to the southeast of Chandigarh, measured 55 m in length and 5-10 m in depth. Four fault strands were identified in this trench. For the purpose of this model, we focus on the strand labeled F3, as it is suggested that the strand labeled F2 occurred in a later event with much less co-seismic slip. The F3 fault strand marks the displacement of a gravel layer, Unit 2, and a silty sand layer, Unit 3, in the hanging wall over Unit 3 in the footwall. The soil layer Qb1 is cross-cut by F3. The Qb2 soil layer is not involved, and serves as a capping horizon for the rupture of F3. Unit 1 is identified as Siwalik bedrock, but this layer is not exposed adjacent to F3. Although it is apparent that colluvium layers have developed above Unit 3, these are not differentiated from Unit 3. Radiocarbon ages for charcoal samples collected from Unit 3 in the footwall of F3 (C-14, C-18, C-19, and C-21) and from colluvium layers in Unit 3 that cap the faulted sequence (C-13, C-15, and C-22 and C-24) are the constraining radiocarbon ages for this event. Sample C-24 was not included in the model as the published radiocarbon age was given only as “modern”. Several older samples from Unit 2 are also included (C-2, C-5, C-23, C-26, C-27, C-50, C-52 and C-53). The age model gives a two-sigma confidence interval for rupture occurrence in the range of 1304 CE – 1393 CE and a one-sigma confidence interval for occurrence in the range of 1327 CE – 1380 CE.

Rampur Ganda is located approximately 25 km southeast of Kala Amb. The trench excavated at this location (Kumar et al., 2006) measured 58 m long and 12 m deep, and exposed 3 major stratigraphic units. The oldest of these, Unit 1, is sheared, Middle Siwalik sandstone. Unit 1 together with Unit 2, a fluvial sand and gravel layer capped by a succession of soils, are displaced over Unit 2 in the footwall. The fault is capped by Unit 3, consisting of medium to coarse sand with occasional pebbles and interpreted as aeolian fill abutting the newly formed scarp, underlying a layer of colluvium composed of blocky clay. Charcoal samples were collected from Unit 2 in the hanging wall some distance from the fault (AB-18) and at the interface between Unit 2 and Unit 3 in the footwall (AB-07). Unit 3 was also dated above Unit 2 in the footwall (AB-08). Sample AB-18 was omitted due to a low AI and potential error associated with the distance of the sampling location from the fault strand. A two-sigma confidence interval is given for the event occurring within the range of 1265 CE – 1417 CE and a one-sigma confidence interval for the range of 1275 CE – 1400 CE.

The trench at Lal Dhang (Kumar et al., 2006) measured 25 m in length and 4-6 m deep and exposed seven major stratigraphic units. From oldest to youngest: Units 1 and 2 are boulder- to cobble-sized gravel layers, Unit 3 is a poorly compacted sand layer, Unit 4 is a compact, silty clay, and Unit 5 is a sandy loam. Units 1-5 are thrust over and plowed into Unit 5 in the footwall. Both Unit 6, a basal colluvium layer composed of silty clay, and Unit 7, a scarp-derived colluvium layer composed of sandy silt with occasional pebble- to cobble-sized gravel clasts, are unfaulted. Charcoal samples were collected from Unit 3 in the footwall (LDT-02) and in the hanging wall (LDT-15), and from Unit 4 in the footwall (LDT-

11). Additional samples were collected just above the contact between Unit 5 in the footwall and the colluvium layer, Unit 6 (LDT-31), near the hanging wall in Unit 6 (LDT-43) and from the Unit 7 colluvium layer (LDT-32). The age model gives a two-sigma confidence interval at this site for event occurrence in the range of 1293 CE – 1451 CE and a one-sigma confidence interval for occurrence in the range of 1320 CE – 1431 CE.

The southernmost trench site was excavated near Ramnagar (Kumar et al., 2006), approximately 95 km southeast of the Lal Dhang site, and measured 32 m in length. Five stratigraphic units and three fault strands were identified, with all displacement attributed to a single event. Faulted units include: Unit 1, a gravel layer; Unit 2, a silty, sandy clay; Unit 3, a clayey, medium to coarse sand with gravel stringers and Unit 4, a clayey silt to coarse sand layer. Unit 5 is unfaulted, scarp-derived colluvium of dark, clayey sand with weak soil development. Charcoal samples were collected from Unit 3 between the F2 and F3 fault strands (BR-09), Units 3 and 4 in the hanging wall of F2 (BR-06 and BR-15) and the colluvium layer, Unit 5 (BR-07). A two-sigma confidence interval is given for an earthquake occurrence date range between 1281 CE – 1405 CE, and a one-sigma confidence interval for 1286 CE – 1350 CE.

A subsequent trenching study at Ramnagar (Rajendran et al., 2015), directly adjacent to the trench described above, supports the conclusion that the most recent, large-scale rupture at this location occurred in the 14th century. We followed the same procedure for modeling of the radiocarbon age data from this trench using OxCal, and the results are shown in Figure 2.3 alongside the published trench log. Sample BR-P1 NZA 53311, from the

colluvium layer capping the fault strand, was removed due to low AI. A two–sigma confidence interval is given for a rupture date range between 1280 CE – 1360 CE, and a one-sigma confidence interval for 1282 CE – 1326 CE. Rajendran et al. (2015) interpret the trench stratigraphy to suggest a multiple-event scenario with an earlier rupture, but this interpretation is inconclusive according to the authors due to drag folding that was not accounted for in the retrodeformation. The data for the earlier event is not modeled here for the reasons stated in the Methods section above.

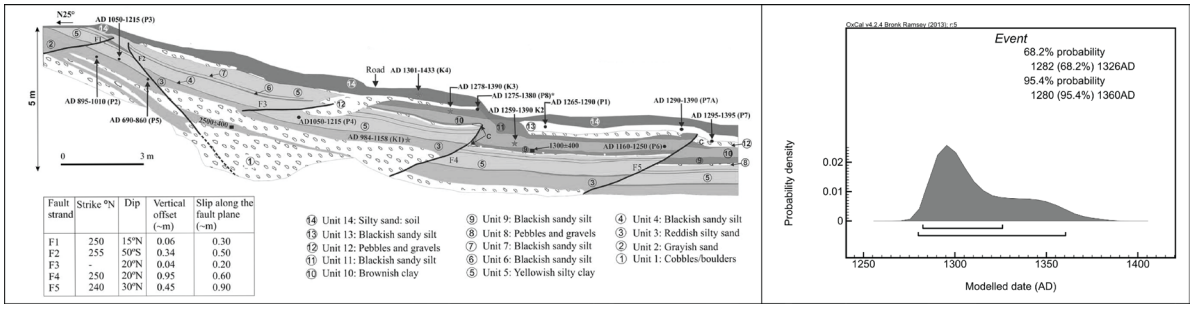

Figure 2.3: (Left) Published paleoseismic trench log for the Ramnagar site by Rajendran et al. (2015), including radiocarbon sample collection locations. (Right) Probability distribution function developed from radiocarbon age results using the OxCal software program (Bronk Ramsey, 2009a).

Discussion and Conclusions

The historical earthquake record for the medieval period (Ambraseys & Jackson, 2003; Iyengar et al., 1999; Jackson, 2002; Pant, 2002; Rana, 1935), which is the period of interest in this study, is held primarily in Nepalese accounts and includes three major earthquakes for the central Himalayan front in 1255 CE, 1344 CE, 1505 CE, and another to the west in 1555 CE. There are also minor references to earthquakes that occurred in 1223

CE and 1408 CE although the evidence for these events is scarce and incomplete. Determining the history of the 1223 CE rupture, which is the earliest earthquake known from authentic historical sources, has proven especially challenging due to complicated linguistic translations and the defacement of historical documents (Pant, 2002). Therefore, the nature of this rupture is not well understood other than the date of its occurrence on December 24, 1223 CE, which falls outside of the two-sigma date range for all of the sites included in this study.

A second 13th century rupture that occurred on June 7, 1255 CE was still recounted by the Nepalese almost 600 years later when they were interviewed in 1833 CE (Rana, 1935). Pant (2002) translates a late 14th-century Newari chronicle: "Very many temples and houses collapsed during the victorious reign of the venerable Abhaya Malladeva. One-third of the subjects…died." This earthquake is also related in a Sanskrit text from the same period, and although minor chronological discrepancies exist between the two accounts, historians have shown the dates given above to be correct (Pant, 2002). There is little doubt that this was a large-scale event, due to multiple documented narratives that describe catastrophic damage in central Nepal. Evidence of this event has been uncovered in several paleoseismic trenches in central and eastern Nepal (Bollinger et al., 2014; Bollinger, et al., 2016; Mishra et al., 2016; Mugnier et al., 2013; Nakata, Kumura & Rockwell, 1998; Sapkota et al., 2013), extending from the area affected by the 1934 CE rupture to the easternmost section of the CSG.

Pant (2002) refers to the same Newari chronicle when describing another great earthquake having occurred in the early afternoon on September 14, 1344. There is little

detail given regarding this rupture, except that it was "big" and that the reigning king, Ari Malla, died the day after the event in Deopatan, near Kathmandu. References to an earthquake in 1408 CE have been questioned due to a lack of historical evidence for this event. It has been suggested that these accounts, in fact, describe the earthquake in 1344 CE, and that they were incorrectly attributed to the 15th century due to a revision of the calendar (Mugnier et al., 2013). Bollinger et al. (2016) argues that "whether the sources reported a true earthquake at a wrong date due to calendric problems must still be clarified by historians". If it is shown that these events are one and the same, then the historical evidence for the two events can be combined to describe a single, great earthquake in the mid-14th century.

The 16th century was marked by two great ruptures of the central Himalayan front. The first of these was the catastrophic Lo Mustang earthquake on June 6th or 7th of 1505 CE, which is well-documented in Tibetan historical accounts (Iyengar et al., 1999; Jackson, 2002). Many sources indicate that this earthquake was felt in Tibet and also in the northern part of India, as far away as Agra. However, the historical record of this event has been distorted due to a second earthquake that occurred on the 6th of July in the same year in Kabul, Afghanistan (Ambraseys & Bilham, 2003; Jackson, 2002). Many of the historical narratives seem to confuse the timing and locations of these ruptures, leading to what Ambraseys and Bilham (2003) describe as an amalgamation of the two events. Therefore, it is difficult to determine with certainty the meizoseismal area for each of these earthquakes. However, because the majority of the historical accounts for this event are from southern Tibet, and because there has been little evidence of the earthquake discovered through

paleoseismic investigation across the HFT, Rajendran et al. (2015) has suggested that the event affecting Lo Mustang may have occurred in the hinterland without rupturing the frontal fault.

Bollinger et al. (2016) proposes that inherited radiocarbon age of charcoal samples may cause overestimation of depositional age, making the 1505 CE earthquake a candidate where evidence is found for 1255 CE or 1344 CE. While all charcoal samples have some inherited age; outliers due to inherited age should be identifiable where there are many samples analyzed and where results are modeled. Additionally, the ratio of old wood to young wood should be very small in an area with major anthropogenic influences, dominant annual monsoon patterns, and short distance fluvial transport mechanisms. Sapkota et al. (2013) and Bollinger et al. (2014) found average inherited ages of only a few decades at the Sir Khola site in Nepal (Bollinger et al., 2016), which may indicate that a small correction factor is justified for individual samples with consideration given to the percentage error of the original radiocarbon age of the sample. For this study, in the absence of a systematic process for adjusting radiocarbon age to reflect inherited age, we have modeled each of the sites based solely on the published radiocarbon data and associated error margins with the understanding that a small adjustment may be warranted.

The second 16th century event occurred farther to the west, in the area of Kashmir, in September of 1555 CE according to both Sanskrit and Persian sources. This event, which is extensively documented in historical texts (Ambraseys & Jackson, 2003), has been assigned a preliminary magnitude of 7.56 by Ambraseys and Douglas (2004). The rupture caused widespread destruction in the Kashmir valley, including landslides and rockfalls, with tens of

thousands of casualties. This event may correspond to the fault rupture exposed at the Hajipur site, which is the northernmost site included in this study (Figure 2.1). While the date of the event at this site is not well-constrained due to a lack of radiocarbon data, the location of this trench lies just to the southeast of the likely epicenter of this event.

The age model presented here indicates a likelihood of one event, coeval on the HFT across five paleoseismic sites in northern, west-central India, corresponding to a historically documented earthquake in 1344 A.D (Pant, 2002), with an estimated magnitude of ≥ 8.6 M_w (Feldl & Bilham, 2006; Jayangondaperumal, Mugnier, & Dubey, 2013). The two-sigma confidence intervals for the Chandigarh, Kala Amb and Ramnagar sites are narrowly constrained to the 14th century and include probability density for only this event. The probability distributions for the sites of Rampur Ganda and Lal Dhang are bimodal with median dates of 1322 CE and 1382 CE, respectively, and both include probability around the event in 1344 CE. Note that the antinode for each of these distributions falls near 1344 CE with the greatest probability densities for each of these sites falling around dates before or after, but not including 1344 CE. Perhaps future studies at these sites will improve the age constraint for this event horizon, which may result in narrower, unimodal probability distributions. When considering the two-sigma confidence intervals in the context of the historical earthquake record, however, the 14th century earthquake is the one event within the range of the probability distributions at both of these sites (Figure 2.2).

Taken together, the results (Figure 2.4) suggest that the most recent large-scale rupture along the western half of the CSG likely occurred in the historically documented earthquake of 1344 CE. However, due to the small number of charcoal samples collected

from these sites, including those from capping colluvium units where reworked charcoal samples may lead to the overestimation of depositional age, it is possible that these probability distributions are overly constrained. For this reason, the earthquake of 1505 CE remains a possible, though perhaps less probable, candidate for the event that ruptured this segment of the CSG.

To the northwest of the CSG, results are less conclusive. The two-sigma confidence interval for Bhatpur includes probability for rupture having occurred in 1344 CE, however the greatest probability density for this site falls around the early 15th century. It is worth noting, however, that historical evidence for earthquakes along this section of the HFT in the 15th century is scarce, if not nonexistent, as discussed above. The timing of the rupture at the northernmost site of Hajipur is poorly constrained due to a dearth of radiocarbon data at this site, and therefore some probability exists for ruptures corresponding to any of several historical earthquakes. However, the earthquake of 1555 CE is a probable candidate at this location, due to the site's close proximity to the affected area for that event.

Preliminary estimates of recurrence intervals for the eastern section of the CSG in Nepal can be calculated as 1934 CE – 1255 CE or 679 years (Sapkota et al., 2013), or 1934 CE – 1100 CE or 834 years (Mugnier et al., 2013). For the western section of the CSG in India, our model suggests rupture in the earthquake of 1344 CE, with no subsequent large-scale rupture in the last 672 years, reinforcing the concern for an impending large-magnitude event which would be catastrophic for nearby populations.

Future studies in this area should include the continued geomorphic and paleoseismic investigation of this segment of the CSG, with a focus on producing an ample number of

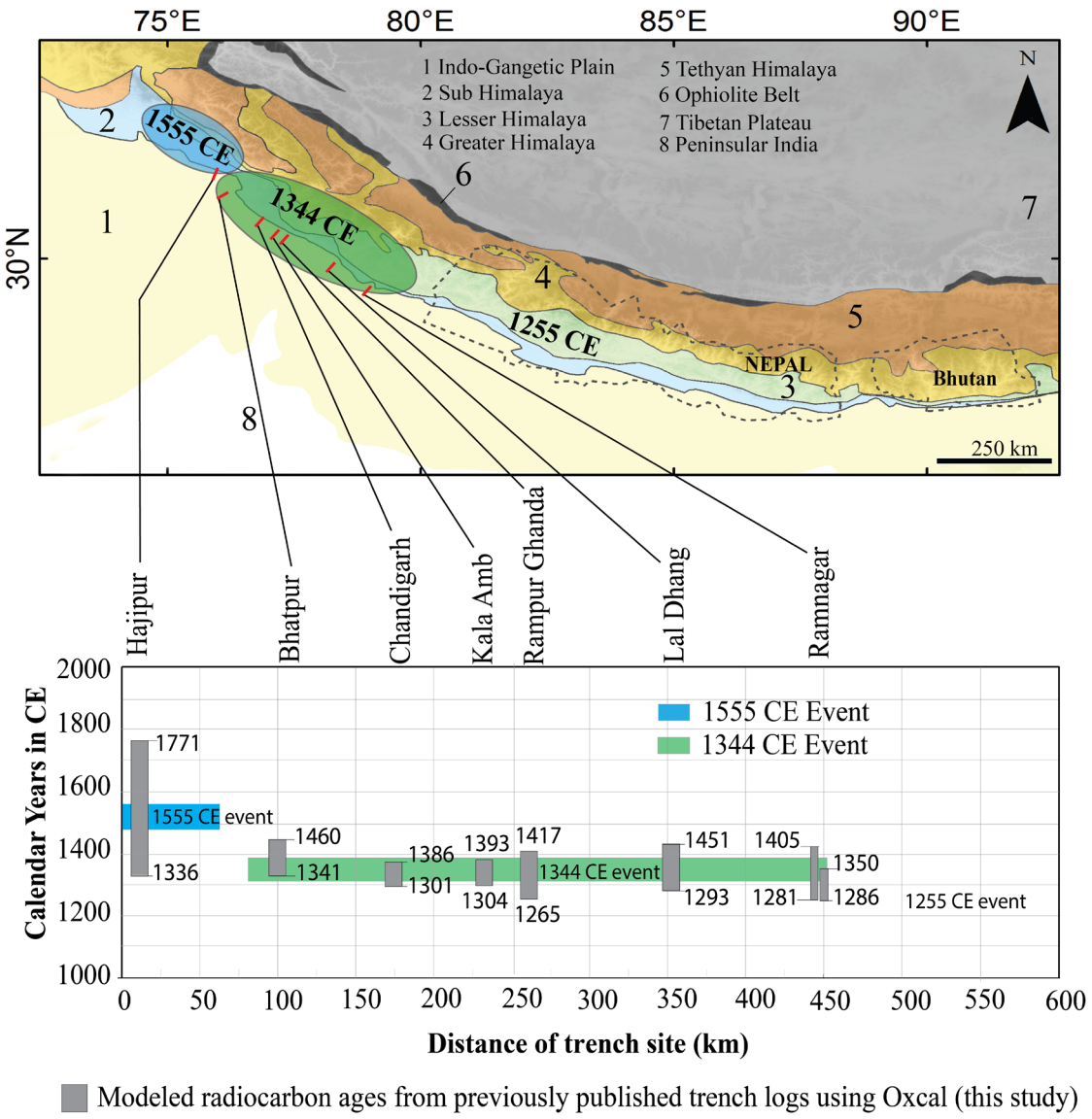

Figure 2.4: Map showing areas of the Central Seismic Gap affected by penultimate large-scale (~8 M_w) earthquakes, as inferred from paleoseismological evidence. Colored ellipses show estimated rupture areas of large-scale earthquakes. Modeled two-sigma confidence intervals for seismic events at each of the modeled sites are shown as grey bars on graph below map. Results indicate that the western section of the CSG likely ruptured in an event corresponding to historical accounts of an earthquake in 1344 CE.

geological samples from fault-capping units for better constraint of minimum limiting ages of events. Incorporating other types of age constraints into these models, such as luminescence or cosmogenic nuclide dating, will require that these types of samples be collected routinely in the future. Further, a systematic investigation on the influence of inherited radiocarbon age in the Himalayan region would allow for greater accuracy in estimating ages of radiocarbon samples and resultant age models. Regional seismic hazard analysis depends on the future of this work, and our ability to better understand the nature and timing of the large magnitude earthquakes that have ruptured the Himalayan Frontal Thrust.

CHAPTER 3

LATE MEDIEVAL SEISMICITY ON THE HIMALAYAN FRONTAL THRUST FAULT AT LAL DHANG, UTTARAKHAND, INDIA

Daniels, R.L., Niemi, T.M., Jayangondaperumal, R., Aravind, A., Rautela, P., Pandey, A., and Murphy, L.D. (2023), Late Medieval seismicity on the Himalayan Frontal Thrust Fault at Lal Dhang, Uttarakhand, India. *Tectonophysics*, 864, 2023, 229934, 1-14. https://doi.org/10.1016/j.tecto.2023.229934.

Abstract

The Himalayan Frontal Thrust Fault (HFT) lies at the active tectonic boundary between Eurasia and the Indian subcontinent. Past earthquakes on the HFT have resulted in significant ground displacement that is evidenced by sizable scarps along the fault. Here we present findings from an ~28-m-long x 5-m-wide x 8-m-deep paleoseismic trench excavated across an ~10-m-high fault scarp at the site of Lal Dhang in the Central Seismic Gap. Excavation exposed three recumbent fault-propagation folds that support occurrence of at least two earthquakes with >25 m of cumulative coseismic slip. Findings suggest that two great ($M_w \geq 8.0$) earthquakes may have occurred in rapid succession at the site during the Late Medieval period. Radiocarbon dating of stratigraphic units that are modeled using the OxCal software program constrain timing of the events to 1317-1391 CE and 1447-1572 CE, which is coincident with historical earthquakes in 1344 CE and 1505 CE. With over 500 years of quiescence since the last great earthquake in the Central Seismic Gap, it is possible that another devastating rupture could be imminent.

Introduction

Continent-continent collision at the tectonic boundary between the Eurasian and Indian plates, which began ~50 Ma, initiated the orogenesis of the Himalayas and produced an associated system of thrust faults that partially accommodate the strain generated through convergence. The faults are oriented parallel to the arcuate plate boundary and span ~2,500 km with an overall strike of northwest to southeast, roughly orthogonal to the average direction of convergence (Figure 3.1a). The convergence rate between the plates is 40-55 mm/yr, with approximately half of this accommodated in the Himalayan arc (Ader et al., 2012; Banerjee & Bürgmann, 2002; Bettinelli et al., 2006; Bilham et al., 1997; Jayangondaperumal, Thakur, Joevivek, Rao, & Gupta, 2018; Lavé & Avouac, 2000; Stevens & Avouac, 2015; Thakur et al., 2014). The active boundary has migrated progressively southward with younger thrust faults forming toward the foreland and connecting with older fault strands along a décollement that separates the over-riding Eurasian plate from the Indian plate at depth. These fault strands mark approximate boundaries for the three major physiographic zones of the Himalayas: the Greater (or High), Lesser, and Sub Himalayas (Figure 3.1a). The current active boundary lies at the youngest of these faults, the Himalayan Frontal Thrust Fault (HFT), which has produced instrumentally documented major (M_w 7.0-7.9) and great ($M_w \geq 8.0$) earthquakes throughout the last century (e.g., Ambraseys & Douglas, 2004). The HFT dips northward at an estimated 20°-45° (e.g., Kumar et al., 2006; Lavé et al., 2005) and verges southward, displacing Neogene and Quaternary sedimentary units (Siwalik Group) over the sediments of the Indo-Gangetic Plain.

Figure 3.1 shows a map of the Himalayan Thrust Fault System and two schematic

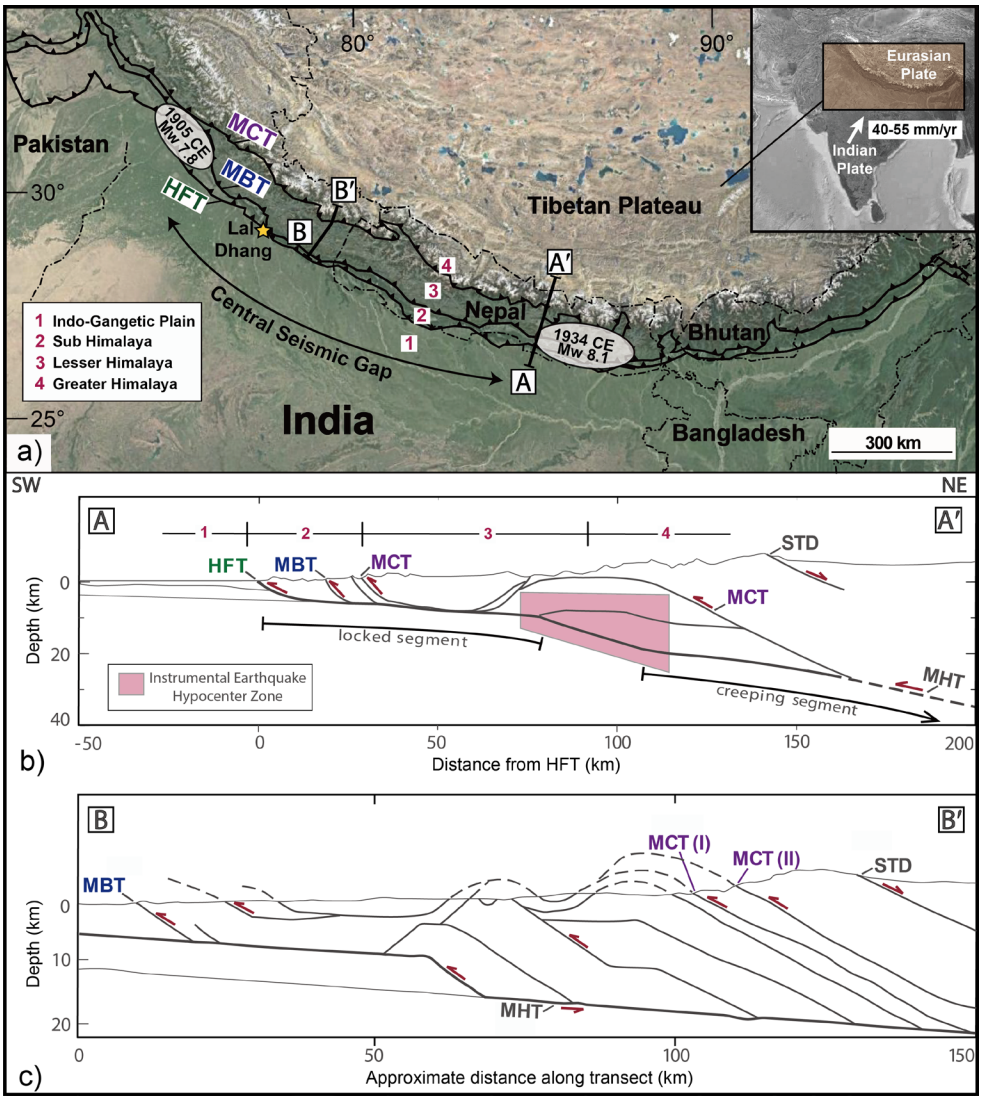

Figure 3.1: Map and cross-sections of The Himalayan Thrust Fault System at the tectonic boundary between the Eurasian and Indian plates. a) Satellite image from Google Earth. Main thrust faults are: MCT - Main Central Thrust; MBT - Main Boundary Thrust; and HFT - Himalayan Frontal Thrust. Major physiographic regions delimited by these faults are labeled according to the legend. Central Seismic Gap (CSG) lies between the areas affected by the 1905 CE and 1934 CE earthquakes. Location of Lal Dhang along the CSG is shown. Cross section transects are delineated along A-A′ and B-B′. Inset map of the Himalayan arc shows the average velocity of convergence. b) Schematic cross section through Kathmandu in central Nepal shows major structures and instrumental earthquake hypocenter zone, adapted from Lavé and Avouac (2001). Transect shown in Figure 3.1a. c) Schematic cross section through the Kumaun region of the Indian Himalaya shows major structures, adapted from Célérier, Harrison, Webb, and Yin (2009). Transect shown in Figure 3.1a. Other structural features shown in cross sections are: STD - Southern Tibet Detachment; MHT - Main Himalayan Thrust.

cross sections that illustrate the subsurface structure of the system, with one transect through Nepal (Figure 3.1b) (Lavé & Avouac, 2001) and another through the Kumaun region of northern India (Figure 3.1c) (Célérier et al., 2009). Also shown is the location of the current study, Lal Dhang, and the approximate bounds of the Central Seismic Gap (CSG), which is defined as the section of the HFT between the areas affected by the 1905 Kangra earthquake to the west and the 1934 Nepal-Bihar earthquake to the east (Figure 3.1a) (Khattri, 1987). The CSG was identified by Khattri (1987) as a section of the HFT that has experienced a quiescence of great earthquakes for more than a century, suggesting that a large magnitude rupture may be more likely to occur in the CSG than on adjacent sections of the fault. Powerful earthquakes occurred within the bounds of the CSG in 1803 CE (M_w 7.46) and 1916 CE (M_w 7.22) (Ambraseys & Douglas, 2004). However, slip deficit studies based on Global Navigation Satellite System (GNSS) data indicate that the magnitude of these events was insufficient to release the total accumulated strain on these segments of the fault (Ader et al., 2012; Banerjee & Bürgmann, 2002; Bilham & Ambraseys, 2005; Bilham et al., 1997; Bollinger et al., 2016; Lavé & Avouac, 2000; Pandey & Tandukar, 1995; Xiong et al., 2017; Yadav et al., 2019).

Paleoseismological investigations have revealed evidence of previous great earthquakes in the western section of the CSG, allowing for preliminary estimation of seismic parameters associated with these events, such as rupture timing, magnitude, coseismic slip measurements, and expected recurrence intervals (Jayangondaperumal et al., 2017a; Kumahara & Jayangondaperumal, 2013; Kumar et al., 2001, 2006; Malik et al., 2010, 2017; Philip, Bhakuni, & Suresh, 2012; Rajendran et al., 2015, 2018). A study by Kumar et

al. (2006) laid the groundwork for characterization of this segment of the fault by outlining findings of paleoseismological investigations at six locations (including Lal Dhang) in the western section of the CSG. The results of that study allow for a single earthquake on this segment of the HFT between 1404 and 1422 CE, based on overlap of radiocarbon-constrained date ranges for earthquake occurrence at five of the six sites. The authors suggest that their observations may correlate to the great, Lo Mustang earthquake of 1505 CE. A subsequent analysis of data from the Kumar et al. (2006) study and others (Kumahara & Jayangondaperumal, 2013; Kumar et al., 2001; Malik et al., 2010; Rajendran et al., 2015) demonstrated that modeling the published radiocarbon data and stratigraphic information together using OxCal (Bronk Ramsey, 2009a; Lienkaemper & Bronk Ramsey, 2009), a Bayesian statistical software program, could narrow the probability distributions for the individually calibrated radiocarbon samples and event horizons at the included sites (Jayangondaperumal, Daniels, & Niemi, 2017b). That study concludes a rupture of this segment of the HFT may correlate to the historically documented earthquake of 1344 CE (Jayangondaperumal et al., 2017b).

Together, these studies were the impetus for the current investigation at the site of Lal Dhang. The goals of this project were four-fold, with the first aimed at reproducing the findings of the Kumar et al. (2006) study, the second at narrowing the relatively wide range of possible rupture dates (1282-1632 CE) presented for Lal Dhang, and the third at investigating a discrepancy between scarp height and estimated coseismic slip at several paleoseismic sites along the CSG. The fourth aspect of this study was motivated by the observation that the previously published paleoseismic trench log for Lal Dhang exhibits

deformational features unlike those presented for the sites of Rampur Ganda, which lies to the west of Lal Dhang, and Ramnagar, which lies to the east (Figure 3.2a). Trench logs for both Rampur Ganda and Ramnagar depict two stacked faults near the base of the scarp with ductile folding and shearing across both fault strands (Kumar et al., 2006; Malik, Naik, Sahoo, Okumura, & Mohanty, 2017; Rajendran et al., 2015). Kumar et al. (2006) observed only one fault strand and associated fold at Lal Dhang. Although myriad factors can affect the type of deformation that occurs at any specific location, many paleoseismic sites within the CSG exhibit remarkably similar deformational features raising a question as to why Lal Dhang would be an outlier in this regard. This study aimed to excavate a larger, deeper trench adjacent to the site of the previous study, in an attempt to resolve these discrepancies by exposing additional stratigraphic evidence for past earthquakes at Lal Dhang.

Methods

The Lal Dhang paleoseismic trench site is located in the state of Uttarakhand ~175 km northeast of Delhi and 55 km southeast of Dehradun (Figure 3.2a). To the north of Lal Dhang, the Rawasan River runs from east to west as it debouches from the Sub Himalaya onto the Gangetic Plain, then turns southwest and empties into the Ganga River ~20 km south of Haridwar (Figure 3.2b). Fluvial terraces adjacent to the Rawasan River that have been uplifted and incised demonstrate the interaction of tectonic and fluvial processes at Lal Dhang. South of the river, the town is abutted to the east-northeast by an ~10-m-high fault scarp striking north-northeast (Figure 3.2c). The scarp extends to the north of the Rawasan river, where it turns back to the northwest, in line with the general strike of the HFT. The focus of this study is the southern section of the scarp bordering the town of Lal Dhang.

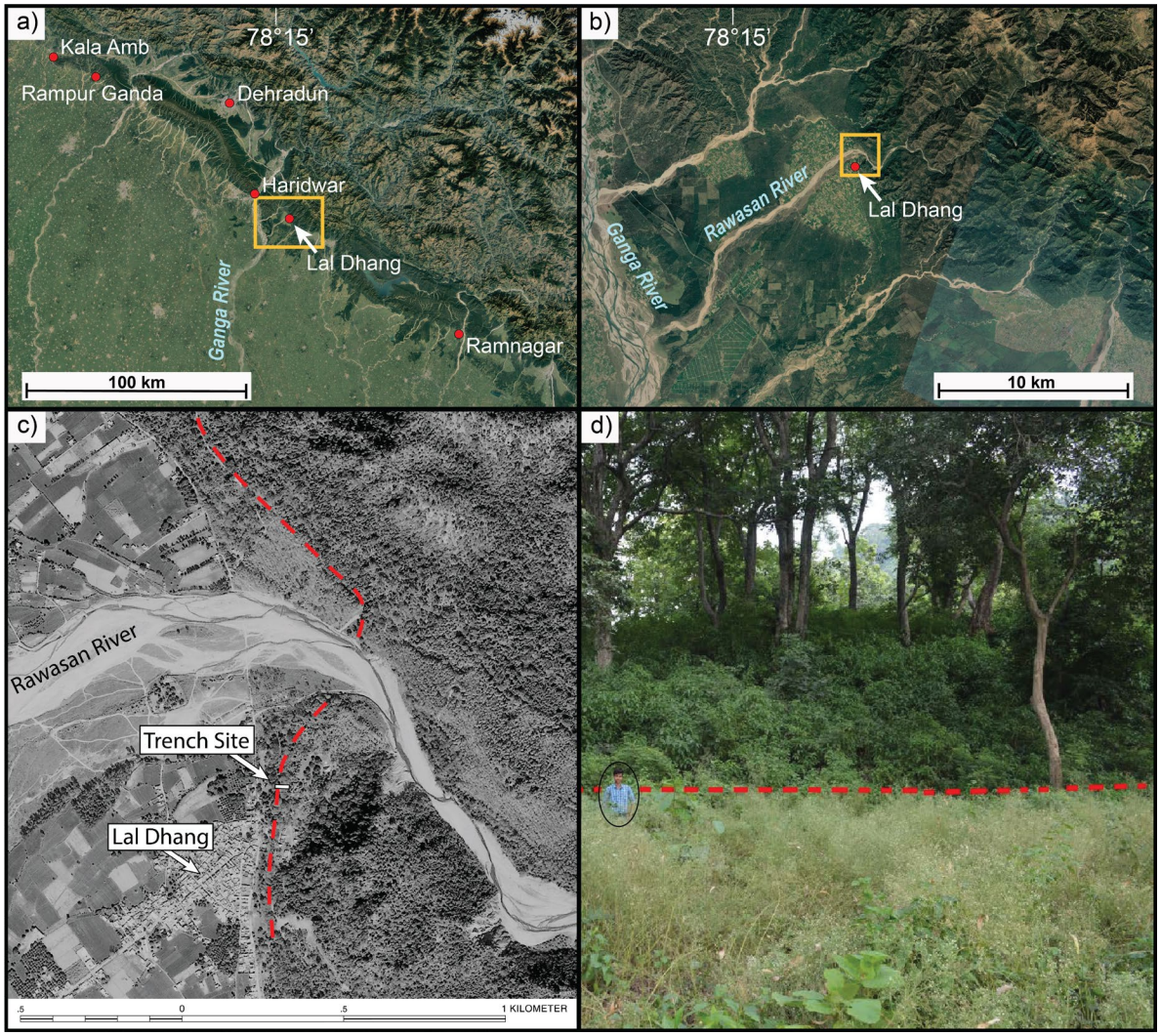

Figure 3.2: The Himalayan Frontal Thrust Fault (HFT) at the site of Lal Dhang. a) Satellite image of the HFT in the region surrounding the study site of Lal Dhang. Locations of previous paleoseismological studies cited in this paper are shown. Yellow box shows the area in Figure 3.2b. b) Lal Dhang is located south of the Rawasan River, which joins the Ganga River to the southwest. Yellow box shows area in Figure 3.2c. c) Map showing location of the trench site (N 29°51'14.13", E 78°19'6.79") (dimensions not to scale), the town of Lal Dhang, and the trace of the HFT fault scarp (red dashed line). d) Photograph of the ~10-m-high fault scarp viewed toward the east. Red, dashed line shows approximate base of scarp. Person for scale (1.5 m) is positioned several meters in front of scarp base.

Figure 3.2d shows a photograph of this section of the fault scarp, and a topographic profile across the scarp is shown in Figure 3.3.

An ~28-m-long x 5-m-wide x 8-m-deep trench with an east-west orientation was excavated across the base of the scarp, approximately 10 m south of the excavation documented in the Kumar et al. (2006) study. The location and orientation of the trench are shown in Figure 3.2c. Excavation was completed with a tracked excavator and occurred in two stages; the first of which defined the margins of the trench and achieved ~75% of the final depth. Benches were constructed along three sides of the trench during the initial stage of excavation to stabilize the walls and provide access to the upper reaches of the exposures. In the second stage of excavation, the benches were removed and the trench was deepened to expose the conformable, depositional sequence of alluvial sediments in the footwall at the west end of the trench. The north and south trench walls were gridded and logged, and the stratigraphic units were described along with the observed structural deformation of the units. Detrital charcoal samples were identified, photographed *in situ*, and collected during both stages of excavation for radiocarbon analysis to determine the timing of deformation. A second ~21-m-long x 2.5-m-wide x 7-m-deep trench was excavated ~15 m to the south of the first trench and was also oriented east-west across the base of the scarp. The bottom of the second trench was sloped approximately parallel to the ground surface so that only ~3-4 vertical meters of trench wall were exposed at any point along the length of the trench. Findings supported the results of the primary excavation but provided no additional insight, as the complete deformational sequence could not be observed due to significant erosion of

Figure 3.3: Photomosaic and trench log of the south wall exposure in the paleoseismic trench at Lal Dhang. Two-sigma probability distribution calendar date ranges for deposition of the stratigraphic units (modeled with OxCal) are shown alongside collection locations of associated detrital charcoal samples. Descriptions of the stratigraphic units in the legend are labeled in accordance with the corresponding units on the trench log. A topographic profile of the scarp is shown above (2x V.E.) with vertical, red lines delimiting the extent of the trench log and a red box marking the approximate location of a test pit excavated higher on the scarp.

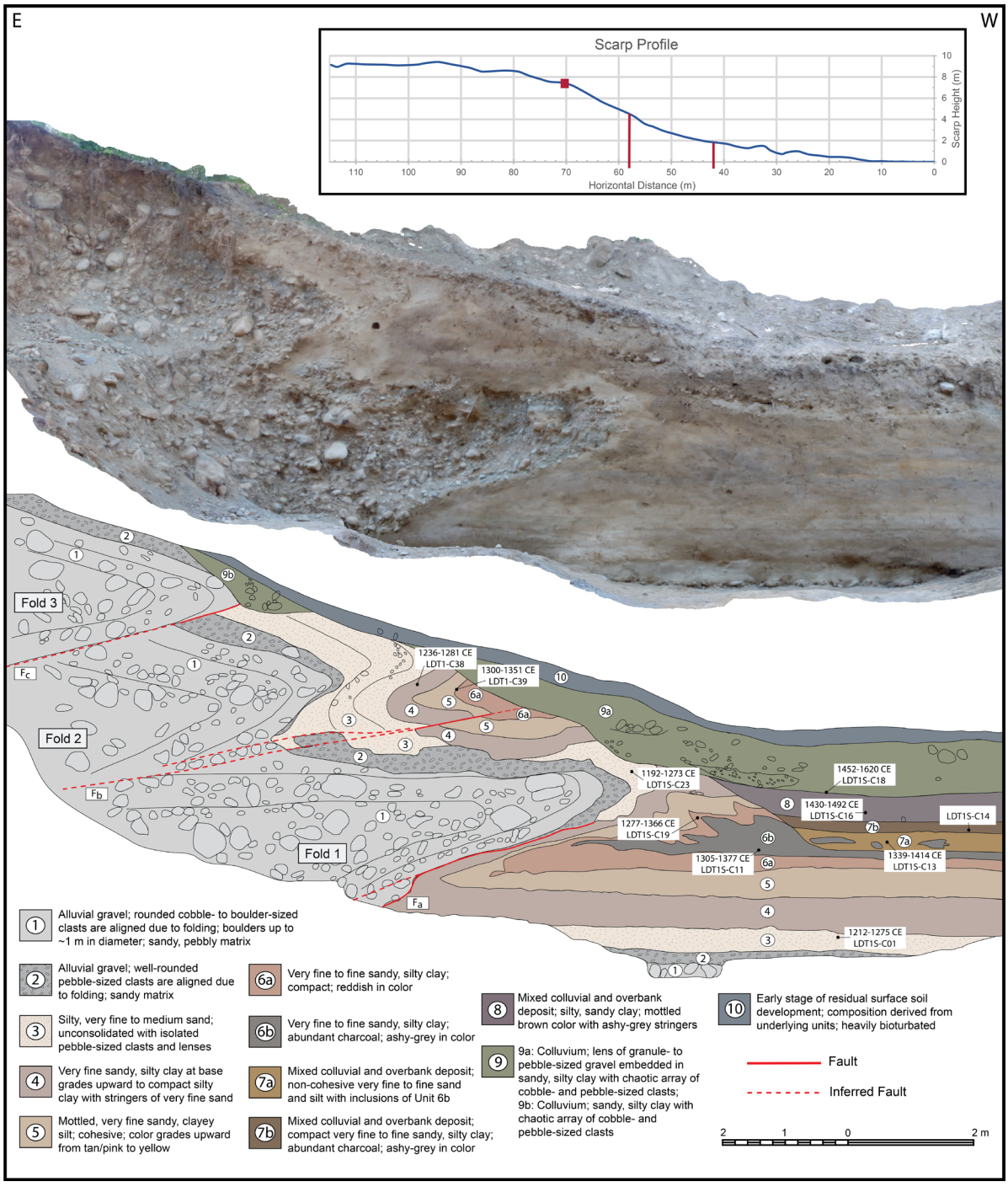
E
W
Scarp Profile
Scarp Height (m)
Horizontal Distance (m)
Fold 3
Fold 2
Fold 1
Fc
Fb
Fa
1236-1281 CE
LDT1-C38
1300-1351 CE
LDT1-C39
1192-1273 CE
LDT1S-C23
1277-1366 CE
LDT1S-C19
1305-1377 CE
LDT1S-C11
1452-1620 CE
LDT1S-C18
1430-1492 CE
LDT1S-C16
LDT1S-C14
1339-1414 CE
LDT1S-C13
1212-1275 CE
LDT1S-C01
1 Alluvial gravel; rounded cobble- to boulder-sized clasts are aligned due to folding; boulders up to ~1 m in diameter; sandy, pebbly matrix
2 Alluvial gravel; well-rounded pebble-sized clasts are aligned due to folding; sandy matrix
3 Silty, very fine to medium sand; unconsolidated with isolated pebble-sized clasts and lenses
4 Very fine sandy, silty clay at base grades upward to compact silty clay with stringers of very fine sand
5 Mottled, very fine sandy, clayey silt; cohesive; color grades upward from tan/pink to yellow
6a Very fine to fine sandy, silty clay; compact; reddish in color
6b Very fine to fine sandy, silty clay; abundant charcoal; ashy-grey in color
7a Mixed colluvial and overbank deposit; non-cohesive very fine to fine sand and silt with inclusions of Unit 6b
7b Mixed colluvial and overbank deposit; compact very fine to fine sandy, silty clay; abundant charcoal; ashy-grey in color
8 Mixed colluvial and overbank deposit; silty, sandy clay; mottled brown color with ashy-grey stringers
9 9a: Colluvium; lens of granule- to pebble-sized gravel embedded in sandy, silty clay with chaotic array of cobble- and pebble-sized clasts; 9b: Colluvium; sandy, silty clay with chaotic array of cobble- and pebble-sized clasts
10 Early stage of residual surface soil development; composition derived from underlying units; heavily bioturbated
Fault
Inferred Fault
2 1 0 2 m

this section of the scarp and extensive anthropogenic disturbance of the stratigraphy. A trench log for the north wall of this trench can be viewed in the supplementary data section.

Results

Stratigraphy and Deformation

The paleoseismic trench presented here (Figure 3.3) exposed evidence of deformation in unlithified, alluvial sediments that were folded and thrust onto the ground surface of the footwall, consistent with the findings of the Kumar et al. (2006) study. However, the exposure in the current trench revealed three recumbent fault-propagation folds, two more than were uncovered in the previous study (Figure 3.3). Each of the upper two folds is positioned above and slightly toward the hinterland of an underlying fold, resulting in a stacked arrangement of three recumbent anticlines (hereafter referred to as Folds 1, 2 and 3, for the lowermost, intermediate, and uppermost, respectively). The stratigraphic units within Folds 1 and 2 include, from oldest to youngest, an alluvial gravel consisting of cobbles and boulders with a maximum observed size of ~1 m in diameter (Unit 1), a stratified, alluvial, predominately pebble-sized gravel with a small fraction of cobble-sized clasts (Unit 2), a loose, fine- to medium-grained overbank floodplain sand (Unit 3), and several layers of compact, fine-grained, floodplain deposits that include some sand but are primarily composed of clay and silt (Units 4-6b). The uppermost of these units is a compact, dark grey, sandy silty clay with abundant charcoal (Unit 6b). The layers composed of gravel (Units 1-2) exhibit alignment of clasts due to folding. Fold 3 consists of only these gravel layers within the excavated area of the trench. Detailed descriptions of the stratigraphic units can be found in the legend for Figure 3.3.

Folds 1 and 2 formed during thrust fault motion on two splays of fault strand F_a. The splay that generated Fold 1 is visible in a drag-fold syncline that is sheared along the fault plane in the footwall below Fold 1. Fold 2 piggybacks Fold 1, and presumably developed above a splay that propagated at depth below the excavated area of the trench. Folds 1 and 2 share an intermediate syncline, and the same stratigraphic sequence that was observed in this syncline was also observed in the lower, drag-fold syncline, as well as in the anticlines of Folds 1 and 2. Small-scale disharmonic and chaotic folds developed as saturated floodplain units (Units 4-6b) were deformed and pushed toward the foreland during the rupture of fault strand F_a, creating a mound on top of Unit 6b in the footwall adjacent to the nose of Fold 1 (Figure 3.4a-b). Units 4-6b are thinned along the limbs of Folds 1 and 2 and thicken into the hinge zones. Alignment of gravel clasts at the contact between Folds 2 and 3, and the truncation of Units 2 and 3 in the backlimb of Fold 2, show that the Fold 3 anticline crosscut the Fold 2 anticline (Figure 3.4d) along fault strand F_c, requiring that Fold 3 formed subsequent to Fold 2. An additional 0.5 m stratigraphic offset along fault strand F_b was observed below the axial plane of the syncline between Folds 1 and 2. The overlying Unit 9a is not apparently offset, indicating that the rupture of this strand probably occurred prior to or during the deposition of Unit 9a but after the formation of Fold 2.

The footwall deposits at the west end of the exposure consist of a conformable, layered sequence of alluvial sediments (Units 1-6), identified as the same units involved in the fold-and-thrust deformation described above (Figure 3.4b). Excavation of a test pit 25 m to the east of the trench, at the crest of the fault scarp above Fold 3 (Figure 3.3), exposed ~1.4 m of floodplain deposits (Units 3-6) overlying the gravel of Units 1 and 2. The thickness

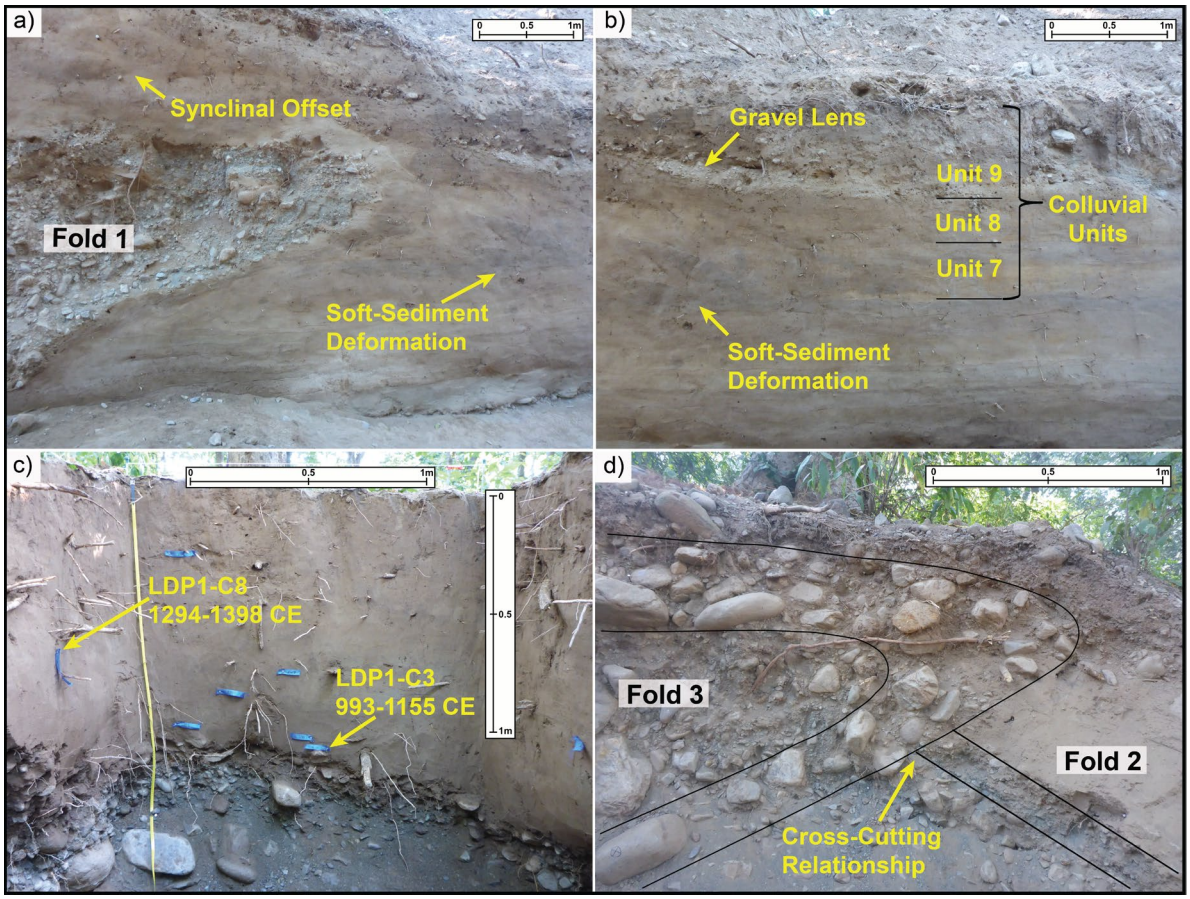

Figure 3.4: High-resolution images of selected features within the paleoseismic trench (a, b, d) and pit (c) at Lal Dhang. Trench images were captured from north to south, with east to the left and west to the right. Pit image is from west to east with north to the left and south to the right. a) Fold 1 anticline with drag-fold syncline below. Soft-sediment deformation features are shown at right center. Offset in the syncline intermediate to Folds 1 and 2 is at top left. b) Conformable alluvial deposits are shown at the west end of the trench covered by approximately 2 m of colluvial deposits in 3 distinct layers. Soft-sediment deformation at the anticlinal hinge of Fold 1 is also shown at left center. c) Pit excavation on scarp above and slightly east of paleoseismic trench. Calibrated age ranges for two processed samples are shown. d) Fold 3 anticlinal forelimb cuts across anticlinal backlimb of Fold 2.

of the floodplain deposits at the top of the scarp is approximately equivalent to the 1.5 m of floodplain deposits that overlie the same gravel in the footwall (Figure 3.4c). Radiocarbon analyses of charcoal collected from Units 3 and 6 in the trench, and from corresponding horizons in the test pit, assisted with correlation of the strata.

The footwall floodplain units are capped adjacent to the base of the fault scarp by nearly 2 m of undeformed colluvial deposits in three distinct layers (Units 7-9) (Figure 3.4b). Unit 7 is a colluvial layer with a mottled texture that is composed of fine-grained sediment. The lower part of this unit (Unit 7a) includes isolated fragments of silty clay, which are of the same texture and color as Unit 6b, and the upper part of the unit (Unit 7b) is a compact, silty clay layer with abundant charcoal fragments. Unit 7 is overlain by an additional fine-grained deposit that contains some silt and sand, but is predominately clay (Unit 8). Above Unit 8 is a third colluvial layer (Unit 9a) that consists of a lens of fine to medium sand and pebbles that grade upward to a stiff, blocky deposit of sandy, silty clay with scattered pebble- and cobble-sized clasts. Unit 9b does not exist within the layered footwall sequence, but is a small colluvial deposit of pebble- to cobble-sized clasts in front of the anticlinal hinge of Fold 3. Unit 10 is a thin layer just below the ground surface, spanning across most of the exposure, that is undergoing the early stages of soil development. It is predominately an organic-rich humus but varies laterally, as its composition is controlled by the underlying units.

Deformation Sequence

Paleoseismological investigations in unlithified sediments can prove enigmatic due to the ductile nature of seismically generated deformational features in these materials, such as folding, stretching, and thinning of the stratigraphic layers, and rotational alignment of gravel clasts. Such features can be more difficult to analyze than the distinct offsets observed in brittlely-deformed rock units. When no direct offset can be observed in unlithified strata, one must analyze factors such as fold characteristics, cross-cutting relationships of deformational structures, and deposition of capping colluvial layers to determine the most likely sequence

of events that produced the observed features. Several possible deformational sequences, including one-, two-, and three-earthquake scenarios, were considered during interpretation of the stratigraphic relationships exposed in the paleoseismic trench during this investigation.

Previous study of the fold-and-thrust deformation at the Lal Dhang site by Kumar et al. (2006) resulted in a single earthquake interpretation, although because of the shallower depth and shorter trench length, that study exposed only one recumbent fold. In this study, a stack of three recumbent folds was exposed, which requires additional interpretation of the deformational sequence. If all of the observed folding across the three stacked folds exposed in this study occurred in a single earthquake, the most likely chronological sequence would be Fold 3, then Fold 2, then Fold 1, as younger thrust faults and associated fault-propagation folds generally form toward the foreland of older fault strands (i.e., in-sequence fold-and-thrust) (e.g., Storti, Salvini, & McClay, 1997). Small-scale sandbox modeling demonstrates that closely spaced, thrust-related folds form in the hanging wall of a subsequent fold that runs out toward the foreland on a thrust fault that accommodates most of the shortening (Storti et al., 1997). However, it is unclear whether this type of deformation across three fault strands is mechanically possible in one earthquake, and the cumulative slip on the combined three folds is very large for one event. Furthermore, cross-cutting relationships of the structures and variation in colluviation require the interpretation of a second earthquake at Lal Dhang.

The continuity of the folded stratigraphic units across Folds 1 and 2, and the shared intermediate syncline, suggest that these folds formed in sequence (Fold 2 then Fold 1) in a single earthquake. The same stratigraphic units (Units 1-6) are observed across both folds,

and the depositional age of the youngest deformed stratigraphic unit in the footwall (Unit 6b) matches the age of the youngest unit within the intermediate syncline, indicating that Folds 1 and 2 formed rapidly in succession in one deformation event. Additionally, no crosscutting relationship was observed between Folds 1 and 2 except for a small (0.5 m) offset on fault strand F_b that can only have occurred after the folding that produced the intermediate syncline. Therefore, these two folds are interpreted to have formed in sequence in a single earthquake event (EQ1).

Mapping of the stratigraphy in the trench shows that thrust fault F_c at the base of Fold 3 truncates Fold 2, indicating that Fold 3 formed after Fold 2 (Figure 3.4d) by a thrust-related fold cutting through the EQ1 hanging wall (i.e., out-of-sequence fold-and-thrust). With energy already propagating toward the foreland during the in-sequence thrusting associated with Folds 1 and 2, it would be unlikely for Fold 3 to form higher on the hanging wall in a break-back progression and crosscut the backlimb of Fold 2 in the same event. Fold 1 and Fold 2 had already formed in EQ1 prior to the thrust-related formation of Fold 3 along fault F_c in a second earthquake (EQ2).

Further evidence that two earthquakes ruptured the HFT at Lal Dhang includes the observation that colluvial deposits in the footwall (Units 7-9) appear to reflect two distinct phases of colluvium development (Figure 3.4b). Unit 7 is interpreted as a colluvial layer that accumulated following the earthquake that generated Folds 1 and 2 (EQ1) because it does not exist in the folded sequence or in the test pit higher on the scarp, it shows no evidence of deformation adjacent to the anticlinal hinge of Fold 1, and it includes only fine-grained colluvium sourced from Units 3-6 along with isolated fragments of silty clay from Unit 6b.

Almost no gravel was observed in Unit 7 or in the overlying Unit 8, which is texturally similar to Unit 7 and is interpreted to demonstrate continued accumulation of fine-grained, scarp-derived colluvium. Because the elevation of the footwall was unchanged during EQ1, colluvial Units 7 and 8 were likely deposited in an environment of continued episodic accumulation of floodplain sediment following that event. The blocky and chaotic texture of Unit 9a is noticeably different from the underlying layers, suggesting a second phase of colluvium development following a second earthquake (EQ2). Additionally, the large amount of pebble- and cobble-sized gravel at the base of Unit 9a could not have been sourced from Folds 1 or 2, as gravel Units 1 and 2 are only exposed at the surface in Fold 3. For these collective reasons, deformation across Folds 1 and 2 is interpreted to have occurred in sequence during a single earthquake (EQ1), with Fold 3 forming later in a second, out-of-sequence event (EQ2).

The observed stratigraphic offset in the intermediate syncline (Figure 3.4a) along fault strand F_b could be a break thrust that formed immediately following the formation of Fold 2 in EQ1 as energy propagated forward on fault strand F_a and Fold 1 began to form, although in this case the syncline would likely be offset above rather than below the axial plane. This strand could also be evidence of an out-of-sequence rupture in a later, third event, although colluvial Unit 9a does not appear to be offset along the fault. Given the problems with these two scenarios, fault strand F_b is interpreted to be a bifurcation of fault strand F_c that ruptured during EQ2. Depositional dates of the strata in the pit at the top of the scarp and in the non-colluvial footwall deposits adjacent to the base of the scarp are the same, which would make it improbable that an older fault strand initially formed the scarp in a rupture

toward the hinterland of Fold 3. It is possible, however, that a younger out-of-sequence fault strand ruptured in the hanging wall of Fold 3, but no evidence was observed to support this possibility. A schematic depiction of the interpreted earthquake chronology evidenced at Lal Dhang is shown in Figure 3.5.

Coseismic Slip and Displacement

Estimation of coseismic slip for ruptures that cause ductile deformation in a fluvial setting is complicated by factors that include lateral facies changes, variations in depositional thicknesses, stretching and thinning of beds during deformation, and extensive erosion of deformed units. However, a reasonable estimate can be made by measuring the folded contact, with the assumption that stretching and thinning of the limbs is approximately equal to shortening and thickening in the hinge zones, and with the caveat that a margin of error exists if the contact is not measured parallel to the slip vector.

Measurement of the contact between Units 1 and 2 across Folds 1 and 2, from the hinge of the syncline below Fold 1 to the point where Fold 3 truncates Fold 2, gives a total length of ~15.7 m, which is the approximate, original horizontal distance between two ground points. Subtracting the current horizontal distance between the same two points (0.886 m), gives a total horizontal displacement (heave) of ~14.8 m for EQ1. However, to measure the actual horizontal displacement in EQ1, the measurement would need to continue toward the hinterland along the backlimb of Fold 2 to the point where the fold ends and the beds are no longer dipping. The actual current horizontal distance between the base of the Fold 1 forelimb and the base of the Fold 2 backlimb would then need to be subtracted. This procedure would add some amount of horizontal shortening for most, if not all, additional

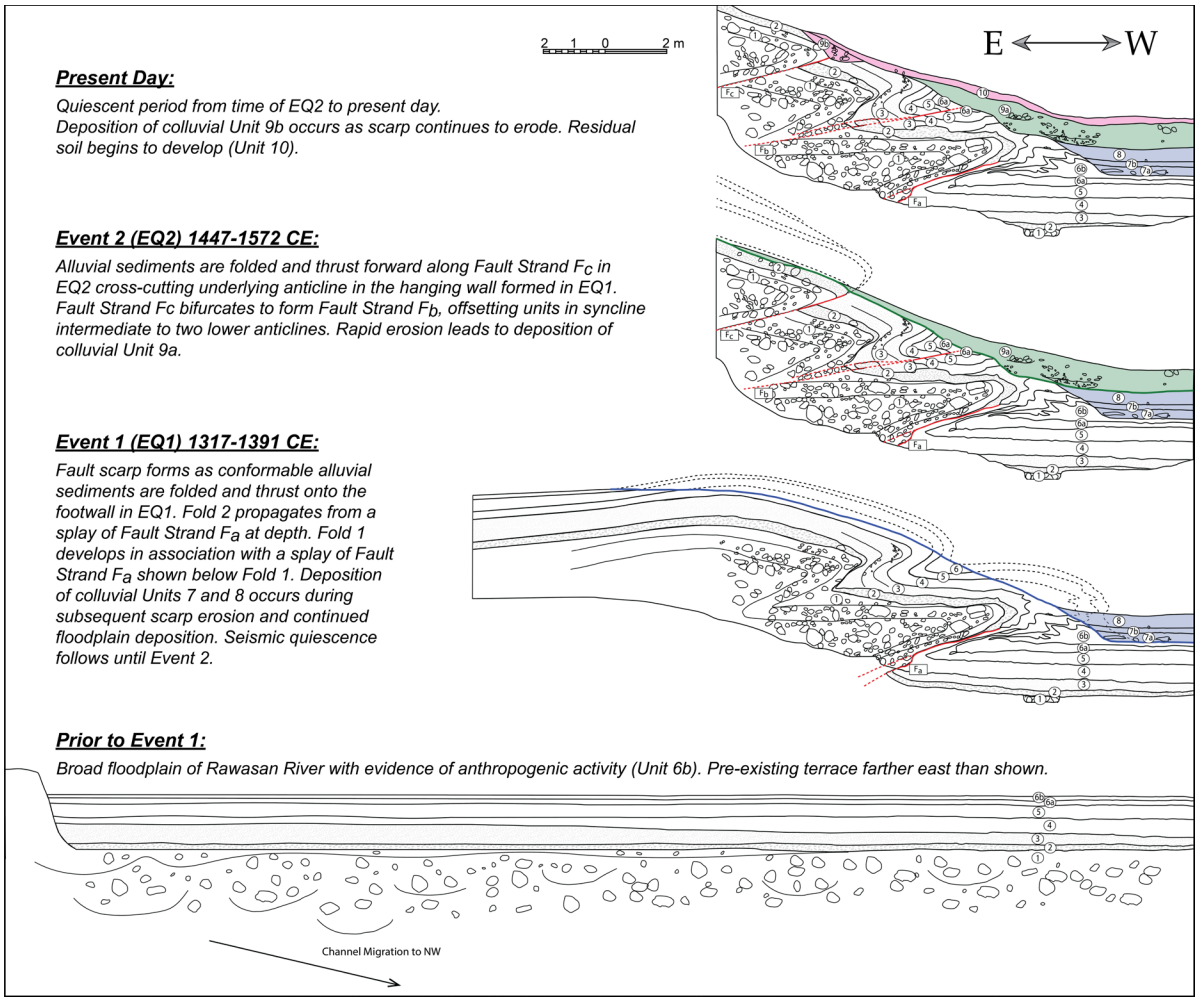

Figure 3.5: Schematic diagram of earthquake chronology on the Himalayan Frontal Thrust Fault at the site of Lal Dhang, in the western section of the Central Seismic Gap. Depiction is based on evidence revealed in a paleoseismic trench excavation across an ~10-meter-high fault scarp at this location. Two earthquakes evidenced at the site are constrained to time periods coincident with great, historically documented earthquakes in 1344 CE and 1505 CE. Dashed black lines illustrate folded sediments in the hanging wall prior to erosion. Colored bold lines indicate the erosional surface following each earthquake and are color matched to associated colluvial layers. Post EQ1 erosion is shown in blue and post EQ2 erosion is shown in green. Continued erosion and soil development are shown in pink. Deformation sequence proceeds from the last panel to the first panel and is pinned at the west end. Unit 6 in the third panel includes both Units 6a and 6b.

meters of length because the amount added would most often be measured along an angle to the horizontal and the amount subtracted would be measured along the horizontal. Therefore,

this is a minimum heave for EQ1 that only includes the parts of Folds 1 and 2 that can be measured within the trench. The average fault strand dip angle within the trench is 18-20° and the faults are assumed to steepen to 20-45° at depth. Using a conservative estimate of 20° for the overall, local dip angle, and dividing the heave by the cosine of 20°, gives a calculated minimum coseismic slip of ~15.7 m for EQ1.

The contact between Units 1 and 2 can be measured on the backlimb of Fold 3, however this contact does not exist on its forelimb because it is an out-of-sequence rupture that cut through the hanging wall of a pre-existing fold. Therefore, the forelimb was measured by following the aligned gravel clasts where Fold 3 cuts Fold 2. The measured length of the fold is ~7.79 m with no current horizontal distance between the two endpoints. However, this is likely an underestimate of the actual horizontal displacement in EQ2 because neither the base of the Fold 3 forelimb nor the base of the Fold 3 backlimb is visible within the trench. The test pit that was excavated 25 m to the east of the trench exposed backtilted gravel, which indicates that the base of the backlimb is likely at least 30 meters to the east of the east end of the trench. The actual current horizontal distance between the base of the forelimb and the base of the backlimb would then need to be subtracted, but as discussed above, there would likely be a net gain in horizontal shortening for each additional meter measured. Using the same procedure as above, the measured heave of ~7.79 m was used to calculate a minimum coseismic slip of ~8.29 m for EQ2. Within the trench, there are two observable direct offsets associated with EQ2 that can be measured. The first is a direct offset adjacent to the hinge line of Fold 3 that measures 0.964 m, and an additional 0.500 m of offset can be measured in the syncline intermediate to the Fold 1 and 2 anticlines. Adding

these slip amounts together, gives a minimum coseismic slip of ~9.75 m for EQ2. Minimum cumulative slip for the two events is ~25.5 m when rounding is completed in the final step of the calculation, which is 18.5 m greater than the slip observed by Kumar et al. (2006).

Multiplying the minimum cumulative slip of ~25.5 m by the sine of 20°, gives a vertical slip component (throw) of ~8.72 m, which is a minimum cumulative vertical displacement following the two earthquakes. This estimate is based solely on the amount of slip that can be measured within the excavated area, prior to erosion. It should be noted that these ruptures are out-of-sequence and therefore the base of the Fold 3 forelimb is well below the top of the scarp that was formed in EQ1. Therefore, there is an overlap of the vertical displacements in the two events, which cannot be quantified for the same reasons that the total coseismic slip cannot be calculated, as discussed above. There is a 1.28 m difference between the estimated minimum cumulative throw of ~8.72 m and the scarp height of ~10 m but the ground surface at the time of scarp formation now lies at a depth of ~2.0 m, making the total difference closer to 3.3 m. This could be the result of a combination of factors that include those described above, pre-existing fluvial terrace topography, and/or the existence of an additional out-of-sequence fault strand toward the hinterland that was not observable within the excavated area (e.g., Jayangondaperumal et al., 2013).

Radiocarbon Analyses and Event Chronology

Determination of calendar date ranges for deposition of the stratigraphic units was achieved through radiometric dating of 15 detrital charcoal samples (see supplementary data), which were calibrated and modeled using the OxCal software program (Bronk Ramsey, 2009a; Reimer et al., 2013). These date ranges are shown in Figure 3.3 alongside

sample collection locations for the south trench wall. Three charcoal samples in our initial OxCal age model produced results with low agreement to the model. Low agreement index (AI) values may occur for reworked, scarp-derived charcoal samples, "old wood" samples with inherited age, or may be the result of myriad additional sources of error. Bronk Ramsey (2009b) recommends removing samples with AI < 60, as this indicates that the sample is an outlier with poor statistical fit to the model. Sample LDT1S-C14 had a very low AI of 17.4 and was particularly suspect due to its age, which is older than a sample from the underlying unit. The irregular age sequence suggests that this sample is scarp-derived, reworked charcoal that reflects an erroneously old age for deposition of the unit. Therefore, LDT1S-C14 was removed from the model, and its removal brought all remaining sample ages into agreement. The collection location for the sample is shown in Figure 3.3 but a depositional date range is not provided because it is not included in the final model. Uncalibrated radiocarbon data for sample LDT1S-C14, and the OxCal model that was generated prior to its removal, can be viewed in the supplementary data section, along with auxiliary data for each of the other samples collected from the trench and the pit. Radiocarbon results for three of the samples included in the final model are derived from charcoal samples collected from Units 7 and 8 in the north trench wall (Samples LDT1N-C07, LDT1N-C08, and LDT1N-C10). The collection location for these samples is indicated on the north wall trench log, which can also be found in the supplementary data section.

When modeled depositional date ranges for units in the undeformed section of the footwall shown in Figure 3.3 are averaged, Unit 3 has a depositional date of ~1240 CE, while Unit 6 that lies ~1.5 m above Unit 3, has a depositional date of ~1340 CE. This indicates that

sediment deposition was occurring at ~15 mm/yr in the ~100-year period immediately preceding EQ1. This rate is considerably faster than published estimates for the whole of the Ganga Plain, which generally fall in the range of ~0.1-1.5 mm/yr (Dingle, Sinclair, Attal, Milodowski, & Singh, 2016; Singh, 1996; Sinha, Friend, & Switsur, 1996); however, this might be expected on a 100-yr timescale at a site proximal to both a river channel and the orogenic front, where sediment can accumulate faster (Dingle et al., 2016; Singh, 1996; Sinha et al., 1996). Such areas are prone to episodic depositional events in response to localized short-term climatic perturbations, as well as precipitation fluctuations associated with seasonal monsoon patterns, and/or frequent geomorphic changes associated with orogenic processes such as mass wasting and seismic events.

Unit 6b is the youngest of the deformed, non-colluvial stratigraphic units and the modeled 2σ probability distribution function (PDF) calendar date range for deposition of this unit (Sample LDT1S-C11) is given as 1305-1377 CE, requiring the earthquake that deformed this unit (EQ1) to have occurred after a date included in this range. The youngest sample collected from the pit above the trench has a calibrated 2σ depositional date range of 1294-1398 CE and was collected at a depth of ~0.5 m. The calculated sedimentation rate prior to deformation is ~15 mm/yr suggesting that the sediments at the top of the pit should be ~30-35 years younger. This indicates that EQ1 also occurred after a date within the approximate range of 1324-1433 CE. Samples collected from Unit 7a, the colluvial layer that developed directly following this event, have modeled 2σ PDF depositional date ranges of 1339-1414 CE (Sample LDT1S-C13), 1346-1407 CE (Sample LDT1N-C08), and 1412-1453 CE (Sample LDT1N-C07), indicating that EQ1 occurred before a date that falls between 1339

and 1453 CE. Samples from the overlying colluvial unit (Unit 8) have modeled 2σ PDF depositional date ranges of 1430-1492 CE (Sample LDT1S-C16), and 1442-1518 CE (Sample LDT1N-C10), indicating that a second rupture associated with the development of Fold 3 (EQ 2) would have occurred after a date that falls between 1430 and 1518 CE. A sample from Unit 9a, which is interpreted to have accumulated following EQ2, has a modeled 2σ PDF depositional date range of 1452-1620 CE (Sample LDT1S-C18), requiring EQ2 to have occurred prior to a date included in that range. When stratigraphic horizons for the two events, delineated by the colluvial contacts described above, are included in the OxCal model (Figure 3.6), the resulting 2σ PDF date range for EQ1 is 1317-1391 CE, and 1447-1572 CE for EQ2.

Discussion

Modeled results for depositional ages of the stratigraphic units and the relative timing of the event horizons (Figure 3.6) suggest that a great earthquake (EQ1) occurred at Lal Dhang between the dates of 1317 CE and 1391 CE, which is coincident with a great historical earthquake in 1344 CE (Bollinger et al., 2016; Jayangondaperumal et al. 2017b; Mugnier et al., 2013; Pant, 2002; Rajendran et al., 2018); and a second event (EQ2) may have occurred between the dates of 1447 CE and 1572 CE, which is coincident with the great Lo Mustang earthquake of 1505 CE (Ambraseys & Jackson, 2003; Iyengar et al., 1999; Jackson, 2002; Rajendran, Rajendran, Sanwal, & Sandiford, 2013). Documented felt areas for the 1344 CE and 1505 CE earthquakes are a considerable distance from Lal Dhang (~500-700 km). However, these reports are indicative of intensity rather than coseismic slip or magnitude, and absence of reports from other areas may not be meaningful due to a lack of

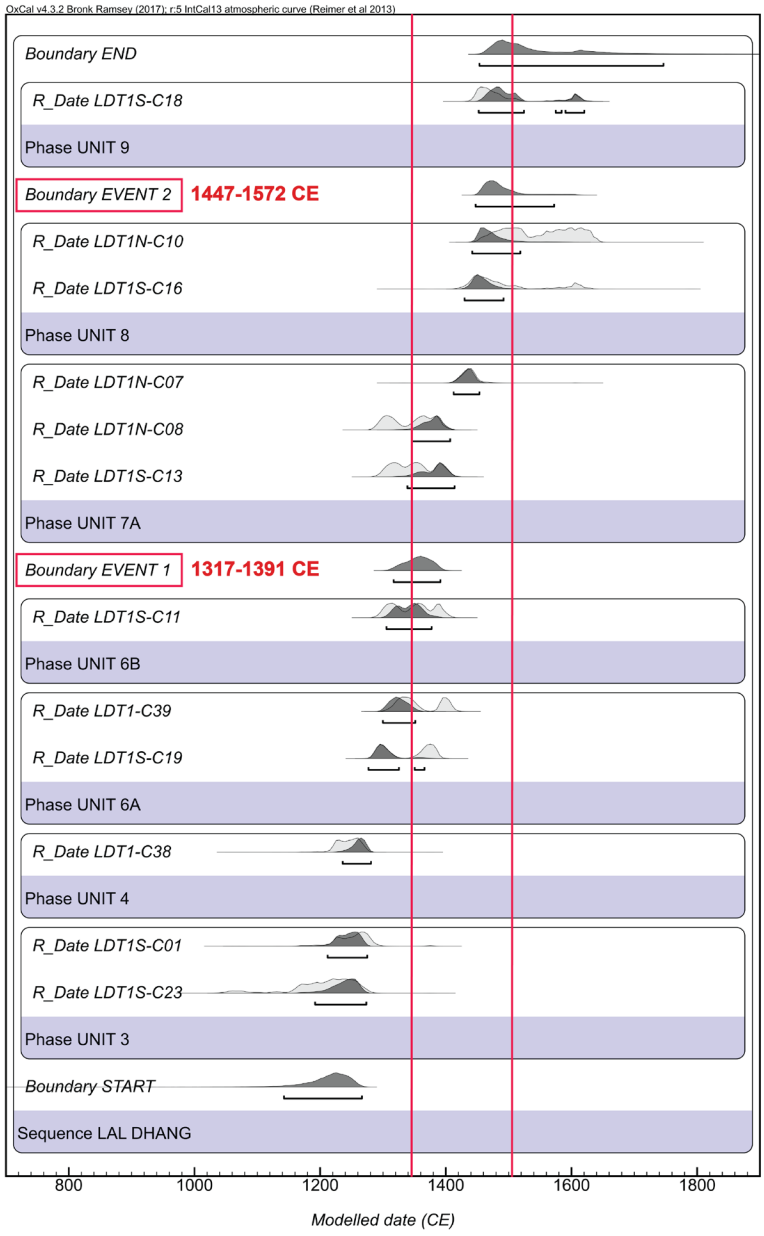

Figure 3.6: OxCal age model for earthquake occurrence at Lal Dhang. Plotted two-sigma (2σ) probability distribution function (PDF) calendar date ranges are shown for each included radiocarbon sample. Also shown are 2σ PDF calendar date ranges for event horizons delineated by colluvial contacts, with the first event constrained to 1317-1391 CE and the second to 1447-1572 CE. Vertical, red lines show timing of great, historically documented earthquakes in 1344 CE and 1505 CE. Boundaries included in the model delimit three distinct sedimentation regimes, which include: 1) original rate of continuous deposition bounded by Event 1, 2) colluviation between Events 1 and 2, and 3) colluviation following Event 2.

historical record keeping in those areas and/or loss of records due to natural disaster or deterioration (Bilham, 2004). It should be noted that the inferred estimates of magnitude and rupture extent discussed below are still quite uncertain and are subject to revision as new historical, archaeological, and paleoseismological findings are published.

The historical record for the 1344 CE event is held in a single document that reports the death of King Ari Malla the following day in Deopatan, near Kathmandu (Pant, 2002). However, there are also accounts of architectural damage that required restoration during the same time period, including repair of the Qutb Minar monument in Delhi that was built between 1198 CE and 1230 CE, and was restored and expanded in 1368 CE (Rajendran et al., 2018). Raw radiocarbon data from previous paleoseismological investigations in the Central Seismic Gap were modeled in a study by Jayangondaperumal et al. (2017b), which concludes that the 1344 CE rupture may have affected the Himalayan Frontal Thrust Fault from at least Bhatpur in the west to Ramnagar in the east, including the site of Lal Dhang. The following year, Rajendran et al. (2018) published results from paleoseismic trench sites at Chorgalia in India, and Mohana Khola in Nepal, which suggest the 1344 CE rupture may extend eastward into western Nepal; however, the trench in Nepal did not produce a well-constrained minimum radiocarbon age for the observed deformational event, so it is possible that the rupture actually occurred in a later earthquake. An earlier comprehensive study that included both historical and paleoseismological evidence for the 1344 CE earthquake by Mugnier et al. (2013) also suggests that the rupture may have extended from Mohana Khola in western Nepal to the Kumaun region of India, and estimates the magnitude of this event as $M_w \geq 8.4$-9.2 with a narrower hypothesis of $M_w \geq 8.6$. However, a more recent review by

Bilham (2019) presents a lower estimate of M_w 7.5-8.2. The latter estimate does not appear to include evidence of the 14th century rupture from the Kumaun region of India. The sources listed include only the historical record and a study by Bollinger et al. (2016) that suggests the 1344 CE earthquake is likely to have caused part of the documented surface rupture in central Nepal at the site of Koilabas that was originally reported by Mugnier, Huyghe, Gajurel, & Becel (2005) to correlate with a historical earthquake in 1255 CE. It is unclear whether these two areas ruptured in the same 14th century earthquake, but if a single earthquake was responsible for surface rupture from the Central Seismic Gap in India to central Nepal, the magnitude would fall closer to the estimate presented by Mugnier et al. (2013). Although only one measurement from a single site, the results presented here support a great 14th century earthquake, with a minimum coseismic slip of 15.7 m in an earthquake between 1317 and 1391 CE (EQ1). The 1344 CE earthquake is the only known earthquake to fall within the estimated date ranges for a 14th century event presented in both the Jayangondaperumal et al. (2017b) study and in the current investigation. However, historical records during this period are scarce, so it is possible that another undocumented earthquake during the same time period is responsible for the deformation observed, as suggested by Kumar et al. (2006) and a recent summary by Wesnousky (2020).

The catastrophic Lo Mustang earthquake of 1505 CE is well-documented in Tibetan historical accounts (Iyengar et al., 1999; Jackson, 2002) and was first reported in association with paleoseismic field data on the HFT at the site of Mohana Khola in western Nepal (Yule, Dawson, Lave, Sapkota, & Tiwari, 2006). Since that time, evidence of this event has been reported at additional sites as far west as Ramnagar in India (Malik et al., 2017) and possibly

as far west as Kala Amb (Kumar et al., 2001; Kumar et al., 2006). Ambraseys and Jackson (2003) suggest that the 1505 CE earthquake was a M_w 8.2 event that produced a surface rupture of ~250 km and damaged buildings along a 700 km stretch of the Himalayas. However, Bilham and Ambraseys (2005) propose that M_w 8.2 may be an underestimate for this event and that the rupture could have spanned the entire length of the CSG (~600 km), requiring M_w 8.6-8.8 and coseismic slip of 7-15 m. A later review by Bilham (2019) suggests a rupture area extending from Ramnagar in India to central Nepal that is 450-550 km in length and ~100 km wide with 10-15 m of slip, and with a projected magnitude between M_w 8.7 and 8.9. A 1505 CE rupture at the Lal Dhang site would expand the western extent to ~100 km west of Ramnagar, likely increasing the projected magnitude to the higher end of that range. The minimum coseismic slip at Lal Dhang for an event between 1447 and 1572 CE (EQ2) is ~9.75 m. However, as outlined in the section on coseismic slip and displacement above, a portion of the slip in EQ2 was not measurable within the bounds of the trench and therefore this is only a minimum estimate. It is possible that EQ2 was actually much larger at Lal Dhang than this slip estimate suggests.

If fault strand F_b is not associated with EQ2 as interpreted here, but instead ruptured in a later, third event, the small amount of coseismic slip would indicate that it was generated during a lesser-magnitude rupture. A possible candidate is the 1803 CE earthquake that affected the Garhwal-Kumaun Region (Ambraseys & Douglas, 2004; Ambraseys & Jackson, 2003; Dasgupta & Mukhopadhyay, 2014; Malik et al., 2017; Martin & Szeliga, 2010). The inferred rupture area for the 1803 event presented by Mugnier et al. (2013) and Bilham (2019) overlaps with the 14th century rupture and includes the site of Lal Dhang. However, a

recent study brings into question whether this rupture reached the Himalayan Frontal Thrust Fault or terminated in the lesser Himalaya (Mohan, Sharma, & Mishra, 2023).

Additional evidence for the possibility of two great Medieval earthquakes in the Central Seismic Gap (CSG) can be found in previous publications. The results of paleoseismological studies at or near the site of Ramnagar, which is located ~100 km southeast of Lal Dhang and is one of the six sites included in the Kumar et al. (2006) study, report evidence of both the 1344 CE earthquake (Rajendran et al., 2015) and the 1505 CE earthquake (Malik et al., 2017). Calendar date ranges for probable rupture published by Kumar et al. (2006) and Rajendran et al. (2015) are 1278-1433 CE and 1259-1433 CE, respectively, coincident with the earthquake in 1344 CE; while Malik et al. (2017) reports 1294-1587 CE and concludes that the rupture evidenced at the site corresponds to the 1505 CE earthquake. An additional study at Ramnagar that employed structural balancing of fault scarp geometry to corroborate paleoseismological findings (Jayangondaperumal et al., 2013) also supports a multiple-earthquake scenario at the site. Further analysis of the trench logs from Kumar et al. (2001; 2006) revealed that the fault orientations and sequences for the included sites share striking geometric similarities and that many of the trenches exhibit two phases of colluvium development, indicating that the same earthquakes may have occurred across the entire study area. Additionally, Kumar et al. (2001) reports evidence for a break-back sequence of two earthquakes that are constrained to 1349 +/-55 CE and 1523 +/-99 CE at the site of Kala Amb (Black Mango), which lies ~20 km to the west of Rampur Ganda, and ~125 km northwest of the Lal Dhang site.

The cumulative evidence suggests that two great magnitude earthquakes, which correlate in age with the documented 1344 CE and 1505 CE events, may have ruptured extensive stretches of the HFT in the western section of the CSG from Bhatpur in the west to at least Ramnagar in the east, and possibly as far east as central Nepal, although paleoseismological evidence in Nepal is equivocal. Figure 3.7 provides inferred rupture areas of the earthquakes that likely occurred at the site of Lal Dhang, based on the current body of paleoseismological research.

If a rapid succession of two large magnitude earthquakes ruptured the HFT at the site of Lal Dhang in the Late Medieval period, it could indicate that the site is located proximate to a segment boundary where rupture overlaps during earthquakes on either of the adjoining segments of the fault. Alternate explanations for clustering of great earthquakes may include a faulting mechanism that requires pulses of great earthquakes within a short period of time to facilitate the complete release of accumulated strain (Feldl & Bilham, 2006; Mugnier et al., 2013) and/or the potential for multiple segments of the fault to rupture in a single event (Kumar et al., 2010; Lavé et al., 2005; Mugnier et al., 2013; Shaw & Dieterich, 2007). While no surface-rupturing earthquakes with a magnitude approaching M_w 9 have occurred at a continent-continent convergence zone in the modern era to provide an analog of what we see in the paleoseismic data, there may be analogous ruptures along subduction zones. A recent review of the Tohoku event by Uchida and Bürgmann (2021) points to evidence for multi-segment and partial ruptures within the slip zones of previous earthquakes in the Aleutian subduction zone (Shennan, Bruhn, & Plafker, 2009), Kuril subduction zone (Nanayama et al., 2003), Sumatra subduction zone (Konca et al., 2008), and Nankai subduction zone (Ando,

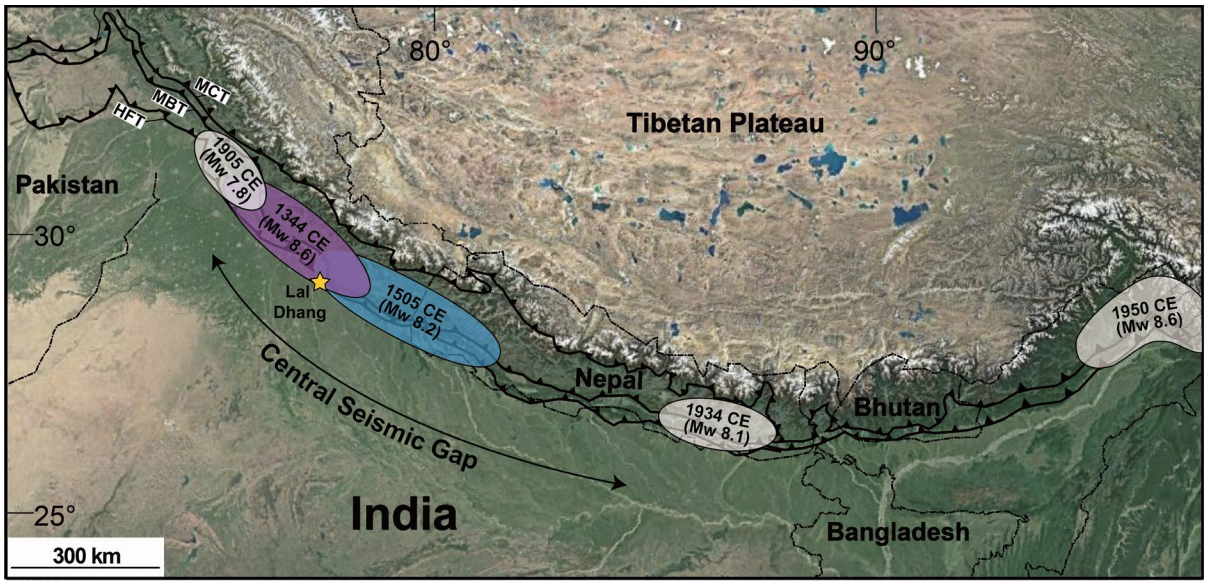

Figure 3.7: Estimated minimum rupture boundaries of Late Medieval earthquakes on the HFT at Lal Dhang. Colored ellipses indicate minimum areal extents of Late Medieval earthquakes at the site of Lal Dhang, inferred from the current body of regional paleoseismological field work including the findings presented here. Major and great magnitude rupture zones for 20th century earthquakes with $M_w \geq 7.8$ (1905 CE, 1934 CE, and 1950 CE) are also shown. Rupture zones for 20th century earthquakes and all magnitude estimates are taken from previously published studies (Mugnier et al., 2013; Bilham, 2019). Note: significant uncertainty remains surrounding the 1344 CE and 1505 CE events and the associated magnitudes and minimum rupture areas are subject to future revision as new field data is collected.

1975). The authors also note that lesser-magnitude events can rupture within these larger slip zones (Uchida et al., 2007). Therefore, they contend that "…if we define likely rupture segments based only on the so far observed, smaller-sized events, even if they had occurred repeatedly, we neglect the real possibility of much larger earthquakes." (Uchida & Bürgmann, 2021). If the stored energy along multiple segments of the HFT is released concurrently in certain earthquakes but not in others, this would introduce an additional element of complexity for the estimation of expected recurrence intervals along the Himalayan front.

Whether the earthquakes would have occurred on multiple smaller segments of the HFT simultaneously, or on a single, expansive segment of the fault is unclear. Lal Dhang lies along a structural feature in the under-riding Indian plate that Khattri (1987) identifies as the Delhi-Hardwar Ridge, which strikes northeast-southwest and separates the Punjab shelf from a deep basin covered by 8-10 km of sediments, known as the Sarda Depression. According to the asperity model, increased strain at the intersection between the fault and the under-riding ridge may increase the likelihood for great earthquakes in areas proximate to the ridge (Bilek, 2007; Khattri & Tiyagi, 1983; Rundle, Kanamori, & McNally, 1984), and locations experiencing this type of stress differential may also be preferential locations for development of fault segment boundaries. This would add an additional risk factor for great earthquakes with very short recurrence intervals in the area spanning from Bhatpur to Ramnagar along the ridge, making additional paleoseismological studies adjacent to these sites critical for validation of these findings and determination of the lateral extent of this phenomenon.

Conclusions

The purpose of this investigation was to determine the nature and chronology of earthquakes at the site of Lal Dhang, while building upon the findings of a previous study in the western section of the Central Seismic Gap by Kumar et al. (2006). Each of the objectives was accomplished, as the findings of the previous study were reproduced; the calendar date range for possible rupture at the site of Lal Dhang was narrowed; and additional structural features were discovered that closely resemble features at paleoseismic trench sites to the

east and west, allowing for an increased estimate of coseismic slip and at least partially addressing a disparity between coseismic slip and scarp height. Specifically, the findings are as follows:

1) Thrust fault deformation reported by Kumar et al. (2006) for the Lal Dhang site was also observed in the current study, along with additional structural features that were likely generated during multiple earthquakes. In this study we document three stacked, recumbent fault-propagation folds that define thrust fault slip events in two earthquakes.

2) The calendar date range for probable rupture at the site of Lal Dhang was narrowed from 1282-1632 CE as reported by Kumar et al. (2006), to 1317-1391 CE for the corresponding event horizon. The calendar date range for rupture corresponding to a possible second event horizon was constrained to 1447-1572 CE.

3) The estimated minimum amount of coseismic slip observed within the bounds of the trench was increased from ≥7 m as observed by Kumar et al. (2006) to ~25.5 m, which accommodates for a total of ~8.72 m of vertical displacement and helps to address a disparity between coseismic slip and scarp height introduced in the former study.

4) Deformational features exposed in the excavation exhibit similarities to the features depicted in trench logs by Kumar et al. (2006) for the sites of Rampur Ganda and Ramnagar, and by Kumar et al. (2001) for the site of Kala Amb (Black Mango). Both the 1344 CE and 1505 CE earthquakes have been

reported in published studies at Ramnagar and are consistent with rupture timing reported for Kala Amb.

Analysis of the trench exposure indicates that two large magnitude earthquakes likely occurred in rapid succession at the site of Lal Dhang in the Late Medieval period, at times coincident with the great earthquakes of 1344 CE and 1505 CE. Such a short recurrence interval between two great events would suggest that the site of Lal Dhang could be located proximate to a fault segment boundary and may therefore experience earthquakes that rupture either of the adjoining segments, or perhaps both adjoining segments in certain large magnitude events. Alternately, the strain release mechanism may be such that pulses of great earthquakes are required to completely release the accumulated strain on a single, expansive segment of the fault. These factors, taken together, indicate that a heightened risk may exist for the clustering of multiple, major to great earthquakes in the area surrounding this site; and a quiescence of >515 years since the time of the last great earthquake may indicate that one or more great magnitude ruptures could be imminent on this segment of the HFT (Bilham & Ambraseys, 2005; Feldl & Bilham, 2006; Stevens & Avouac, 2016).

Much work is left to be done and additional studies are needed to further delineate the seismic history of the Himalayan Frontal Thrust Fault within the Central Seismic Gap, so that the assessment of risk for great magnitude earthquakes on this part of the fault can be achieved with greater accuracy. The Indo-Gangetic plain provides fertile ground for food production and is, therefore, highly developed with densely populated urban areas, increasing the potential risk posed by large-scale, seismic events (Gupta & Gahalaut, 2015; Wyss, Gupta, & Rosset, 2018). Future fault segmentation and boundary studies are critical for

identification of areas that may have a greater seismic hazard due to the likelihood of clustered, great magnitude events. A complete understanding of the characteristics of this thrust fault system is exigent for development of accurate regional seismic hazard assessments that reflect the real potential for imminent, great earthquakes along this segment of the Himalayan Frontal Thrust Fault.

CHAPTER 4

TECTONIC INFLUENCES ON LANDSCAPE DEVELOPMENT ALONG THE HIMALAYAN FRONTAL THRUST FAULT AT LAL DHANG, UTTARAKHAND, INDIA

Daniels, R.L., Niemi, T.M., Jayangondaperumal, R., Aravind, A., Rautela, P., Pandey, A., Murphy, L.D., Thomas, K.A.

Introduction

The development of the Himalayan orogenic wedge at the tectonic boundary between the Eurasian and Indian plates has affected regional drainage patterns by imposing structural control on rivers and streams as they cut across the mountain range and debouche onto the Indo-Gangetic plain. As the range front advances toward the foreland along thrust faults at the active convergent margin, rivers and streams are captured behind new topographic highs, where they run approximately parallel to the range front before downcutting to local base level along structural zones of weakness. Large sediment loads are carried by these waterways due to the continuous erosion of exhumed bedrock in the areas that supply these drainage basins. The entrained sediments are deposited in the foreland basin once local base level is reached, creating extensive accumulations of sediments in front of the range. Molasse units of sandstones, shales and conglomerates develop from the lithification of these deposits and are uplifted during subsequent thrust faulting at the tectonic boundary. Recurrent uplift at the range front, along with subsequent incision, creates complex relationships between fluvial terraces and fault scarps that can be problematic when investigating the seismic

history of these areas. This relationship is further complicated when the orientation of the fault lies at an oblique angle to the direction of convergence, causing an along-strike component of slip that leads to associated horizontal offsets of terraces and the rivers that formed those terraces.

The current, active tectonic margin is the Himalayan Frontal Thrust Fault (HFT), otherwise known as the Main Frontal Thrust Fault (MFT), which lies at the boundary between the Sub-Himalayan Range and the Indo-Gangetic Plain (Figure 4.1). Recent research suggests that a distinct, blind splay of the thrust fault system has developed toward the foreland, and that the active boundary may now be located along this strand; however, the youngest, emergent fault with substantial amounts of observable, vertical separation at the ground surface remains the HFT. While recent large magnitude earthquakes on the HFT have not produced significant vertical offsets, sizeable fault scarps along the front indicate that pre-instrumental ruptures were emergent and generated large amounts of coseismic slip. Because the earthquakes that formed these scarps were likely much larger than recent ruptures, paleoseismological investigations have aimed to determine the timing, magnitude, and expected recurrence intervals of these events, in order to reveal the true seismic potential of the HFT.

The authors of the current study conducted a paleoseismic trenching investigation at the site of Lal Dhang in the Central Seismic Gap (CSG). The CSG is defined as the section of the fault that lies between the areas affected by the 1905 Kangra and 1934 Nepal-Bihar earthquakes (Figure 4.1). Several lines of evidence, including the lack of a recent great ($M_w \geq 8.0$) earthquake, suggest that this segment of the fault may be subject to impending

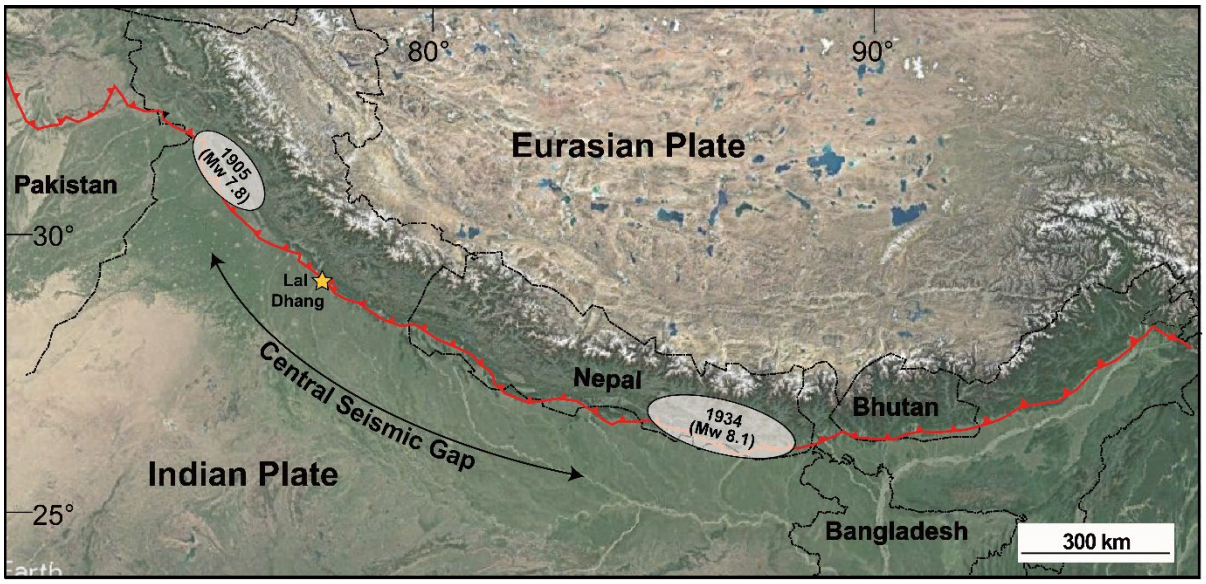

Figure 4.1: Surface trace of the Himalayan Frontal Thrust Fault (HFT) at the boundary between the Indian and Eurasian plates. Surface trace of the HFT is delineated in red with teeth on the upper plate. The segment of the HFT defined by Khattri (1987) as the Central Seismic Gap (CSG) spans between the 1905 Kangra and 1934 Nepal-Bihar earthquakes. The approximate bounds of these events are shown as white ellipses. Yellow star demarcates the site of Lal Dhang, the subject of this study.

large-scale rupture. The results of the study at Lal Dhang suggest that two earthquakes occurred at the site in rapid succession during the Late Medieval period, raising the possibility that Lal Dhang lies along a fault segment boundary or that other complex faulting mechanisms may exist at the site. To determine if geomorphological evidence exists that supports a multiple earthquake scenario at Lal Dhang, and to investigate the influence of the fault on local landscape development, a comprehensive study of the local geomorphic response to tectonic processes was conducted in conjunction with the paleoseismological study. The goal of this study was to determine the geomorphological history of the site as it relates to both tectonic and fluvial processes, specifically the interaction between fluvial terrace development and fault scarp generation.

Methods

Landscape development at the site of Lal Dhang was investigated in conjunction with a paleoseismological trenching study at the site. Detailed analysis of the trench indicated that a very large magnitude earthquake occurred at Lal Dhang in the time period between 1317-1391 CE, which is coincident with a historically documented earthquake in 1344 CE (M_w ~8.6), and that a second great earthquake may have quickly followed in an event during the time period between 1447-1572 CE, which corresponds to a historically documented earthquake in 1505 CE (M_w ~8.2). To determine if additional evidence exists to support a multiple earthquake scenario at the site, and to investigate the influence of tectonics on local landscape development, a comprehensive geomorphological study was conducted concurrent with the opening of the paleoseismic trench. A site map showing the location and orientation of the trench, and two regional maps showing the location of Lal Dhang along the HFT are provided in Figure 4.2.

Lal Dhang is located ~175 km northeast of Delhi and 55 km southeast of Dehradun in the state of Uttarakhand (Figure 4.2a). To the north of town, the Rawasan River flows from east to west as it emerges from the Sub Himalaya onto the Gangetic Plain, before turning southwest and merging with the Ganga River ~20 km south of Haridwar (Figure 4.2b). A stepped series of fluvial terraces associated with the Rawasan river exist alongside a large ~10-m-high fault scarp at this location. A topographic survey was conducted using a Real Time Kinematic (RTK) Global Positioning System (GPS) to determine the absolute elevations of these terrace surfaces and the amount of vertical offset that separates them. The influence of the fault on the development and uplift of the terraces was investigated through

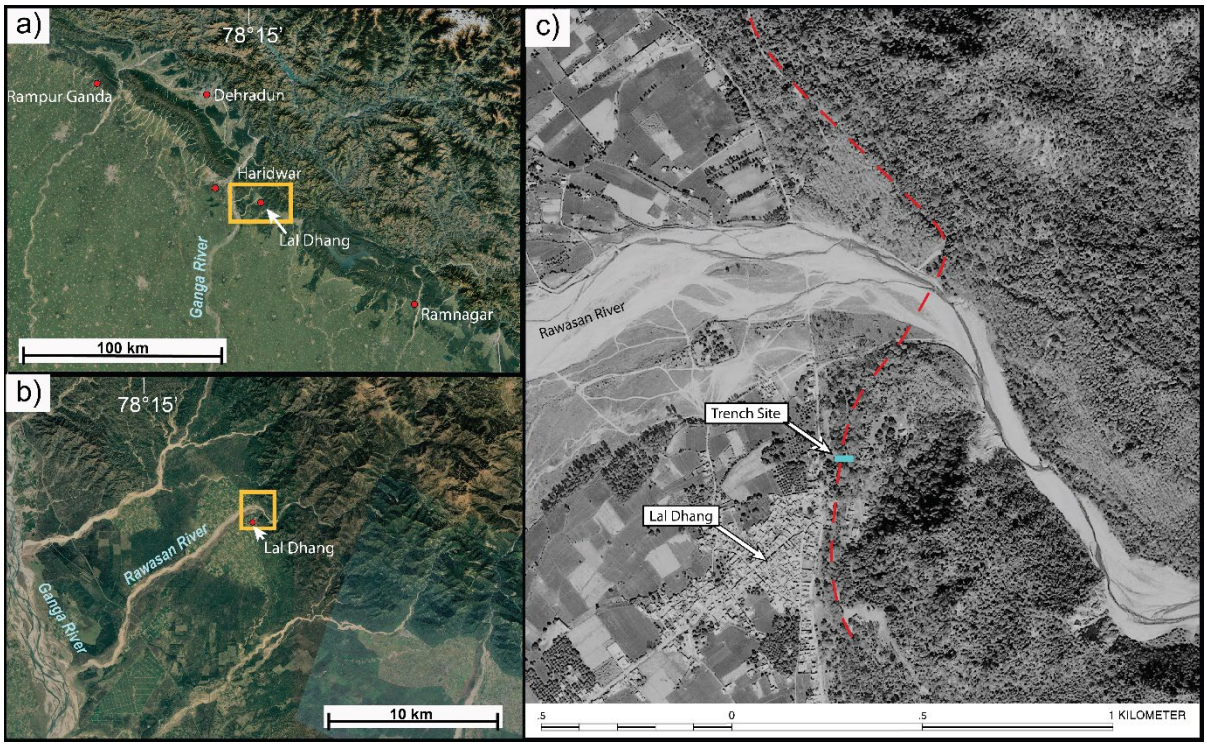

Figure 4.2: Local and regional landscape surrounding the site of Lal Dhang. a) Satellite image of the Himalayan Frontal Thrust fault (HFT) in the region surrounding the study site of Lal Dhang. Reference locations and sites of previous paleoseismological studies cited in this publication are shown. Area within the frame delimits the area depicted in part b. b) Closer view of area framed in part a. Confluence of Rawasan and Ganga River is shown at bottom left. Area within the frame delimits the area depicted in part c. c) Closer view of area framed in part b. Scarp trace is delineated as red, dashed line. Trench location (N 29°51'14.13", E 78°19'6.79") and orientation are shown (not to scale) to the north-northeast of the town of Lal Dhang.

excavation of ~1m^3 pits on each of the surfaces. The stratigraphy exposed in the pits was described, and samples of detrital charcoal were collected from the pits at shallow depths (~20-50 cm) in order to date the most recent deposition of sediment on the respective terrace surfaces. Because deposition should theoretically cease when the land surface is raised to an elevation above the floodplain, these dates should indicate the approximate timing of uplift if

tectonic processes were involved in the generation of these terrace surfaces. Locations and elevations of the various terrace surfaces are shown in Figure 4.3.

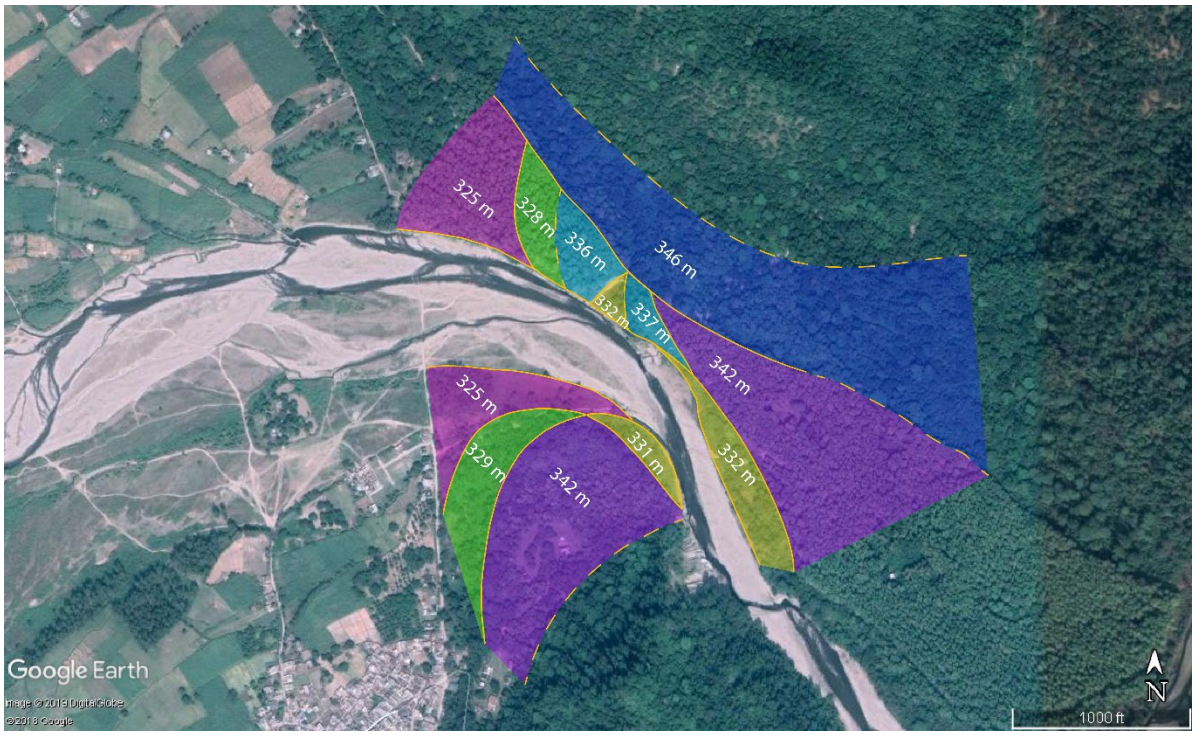

Figure 4.3: Approximate elevations of terraces adjacent to the Rawasan River north of Lal Dhang. Satellite image from Google Earth, 2019. Multiple stages of terrace development show history of uplift and incision due to the interaction of tectonic and fluvial processes. Colors indicate the approximate bounds of corresponding terraces to the north and south of the river. Blue is the highest surface, followed in order of decreasing elevation by purple, turquoise, yellow, green and pink. Solid lines indicate observed vertical offsets. Dashed lines show approximate terrace boundaries based on satellite imagery and elevation data.

Exposed stratigraphy along the Rawasan River was surveyed, with special attention given to large outcrops of sheared, Lower Siwalik sandstone that appear to be in contact with fluvial terrace deposits toward the foreland (Figure 4.4a-b). Additional survey points were collected with an RTK GPS on a subsequent field campaign, and these data were combined with initial survey results to create a detailed contour map of the area that includes the mouth

of the Rawasan River, surrounding fluvial terraces, and the 10-meter-high fault scarp (Figure 4.5). A foot survey was conducted to investigate areas farther to the south that were not easily accessible from the river, where interesting features were discovered that may relate to the changing course of the Rawasan River over time. Once all of the data were compiled, a recent geomorphological history was determined for the site of Lal Dhang that focuses on the dynamics of fault scarp and terrace development, and a model for local fault scarp generation was devised.

Results

Photographs of the strata uncovered during the pit excavations are provided in Figure 4.6, along with collection locations of detrital charcoal samples that were used to date the terrace surfaces. The first of the test pits (LDP1) was excavated east of the paleoseismic trench, higher in the hanging wall of the fault at an elevation of 334 m, to determine if the stratigraphic units in the pit would match the units observed in the footwall of the trench exposure. Approximately 1.5 m of floodplain deposits overlie fluvial gravels in the footwall, and ~1.4 m of floodplain deposits were found to overlie the same fluvial gravels in the pit. Identification of equivalent sequences of non-colluvial floodplain deposits in the footwall and the highest part of the hanging wall supported the interpretation that out-of-sequence thrust fault progression occurred at the site. Out-of-sequence thrusting occurs when fault development progresses away from the foreland, with later events occurring behind the initial rupture and involving the same stratigraphic units that were uplifted in the initial event. A radiocarbon date for a sample collected from a depth of 56 cm in the pit produced a

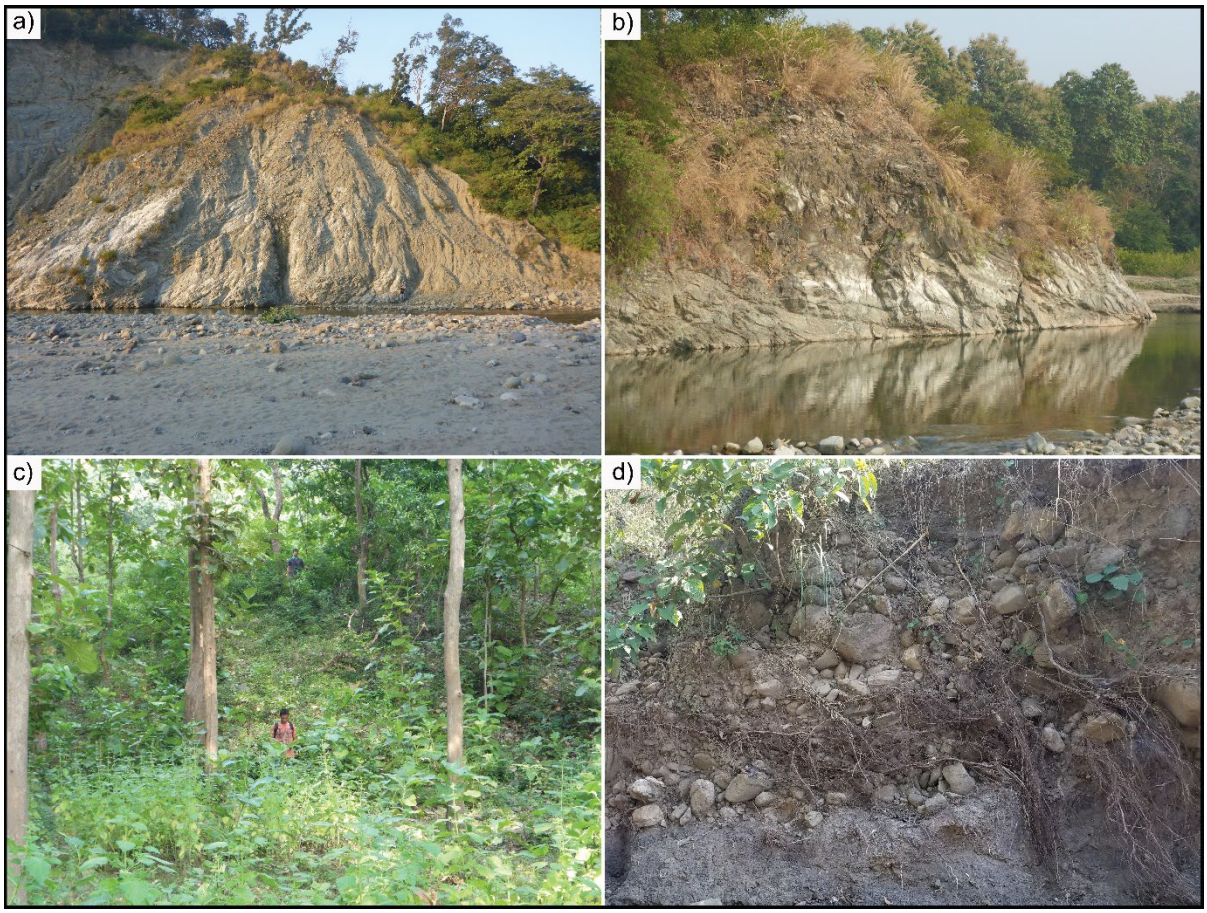

Figure 4.4: Photographs of landscape features at the site of Lal Dhang. a-b) Outcrops of uplifted and sheared Lower Siwalik sandstone along the Rawasan River cut. The image in part a is the outcrop on the south side of the river and part b shows the outcrop on the north side. c) Linear structural feature, known locally as the Muhabharat mound, that is vertically displaced from the surrounding ground surface by ~8 m. d) Abandoned, hanging channel that may be a past segment of the Rawasan River that was truncated and offset during earthquakes at Lal Dhang.

2σ probability distribution function (PDF) date range of 1294-1398 CE, which is similar to the date range determined for deposition of the upper layers of the non-colluvial footwall deposits in the trench exposure. This age constraint provides another line of evidence for the same strata existing in both the footwall of the trench and in the highest reaches of the hanging wall preserved within the scarp.

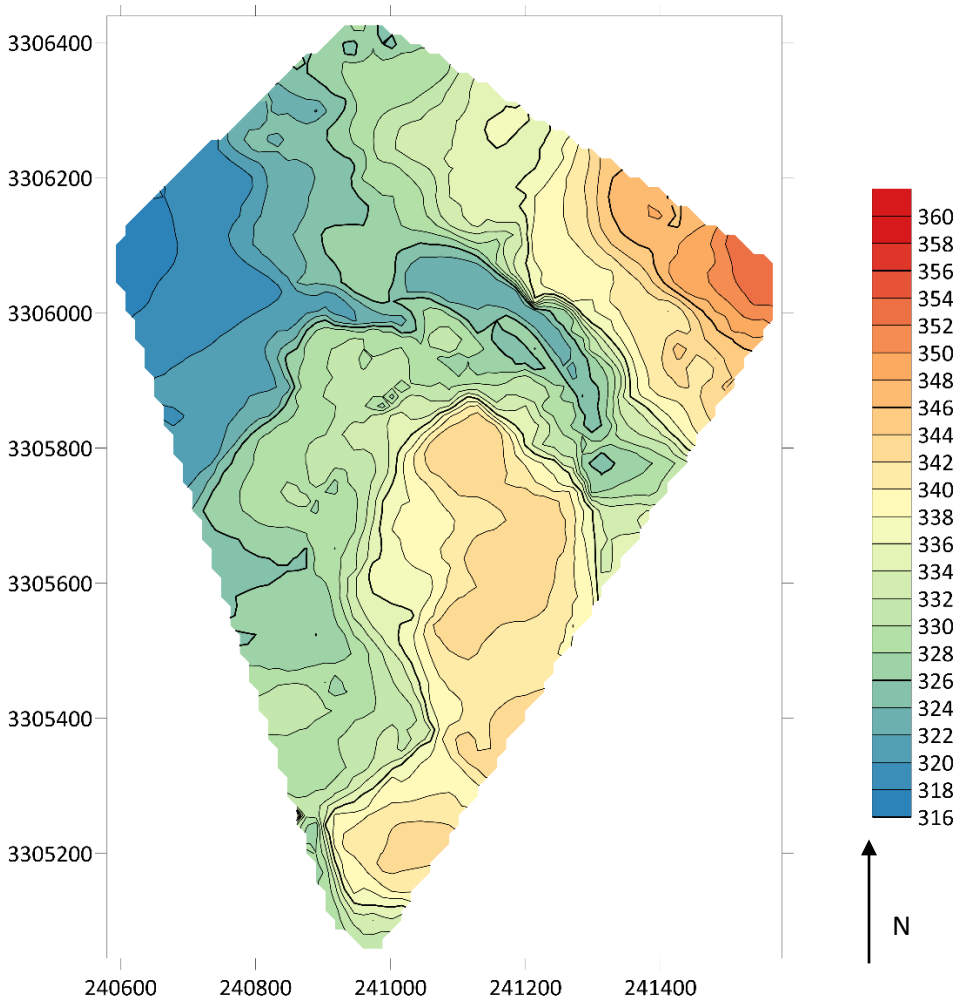

Figure 4.5: Contour map of the area surrounding Lal Dhang. Color-coded legend for elevation data provided at right. Coordinates are in Universal Transverse Mercator (UTM) for zone 44N. Elevation data collected using a Real-Time Kinematic (RTK) Global Positioning System (GPS). Contour map was created using the Surfer software program.

Pits 2-7 were excavated across the river to the north, where a stepped sequence of terraces preserves the history of fluvial processes and tectonic events at the site. Pit 2 (LDP2) was excavated at an elevation of 337 m and produced a charcoal sample from a depth of 30 cm that yielded a 2σ PDF date range of 1441-1618 CE. Pits 3 and 4 (LDP3 and LDP4) were excavated in close proximity to each other on a surface with an elevation of ~346 m. A

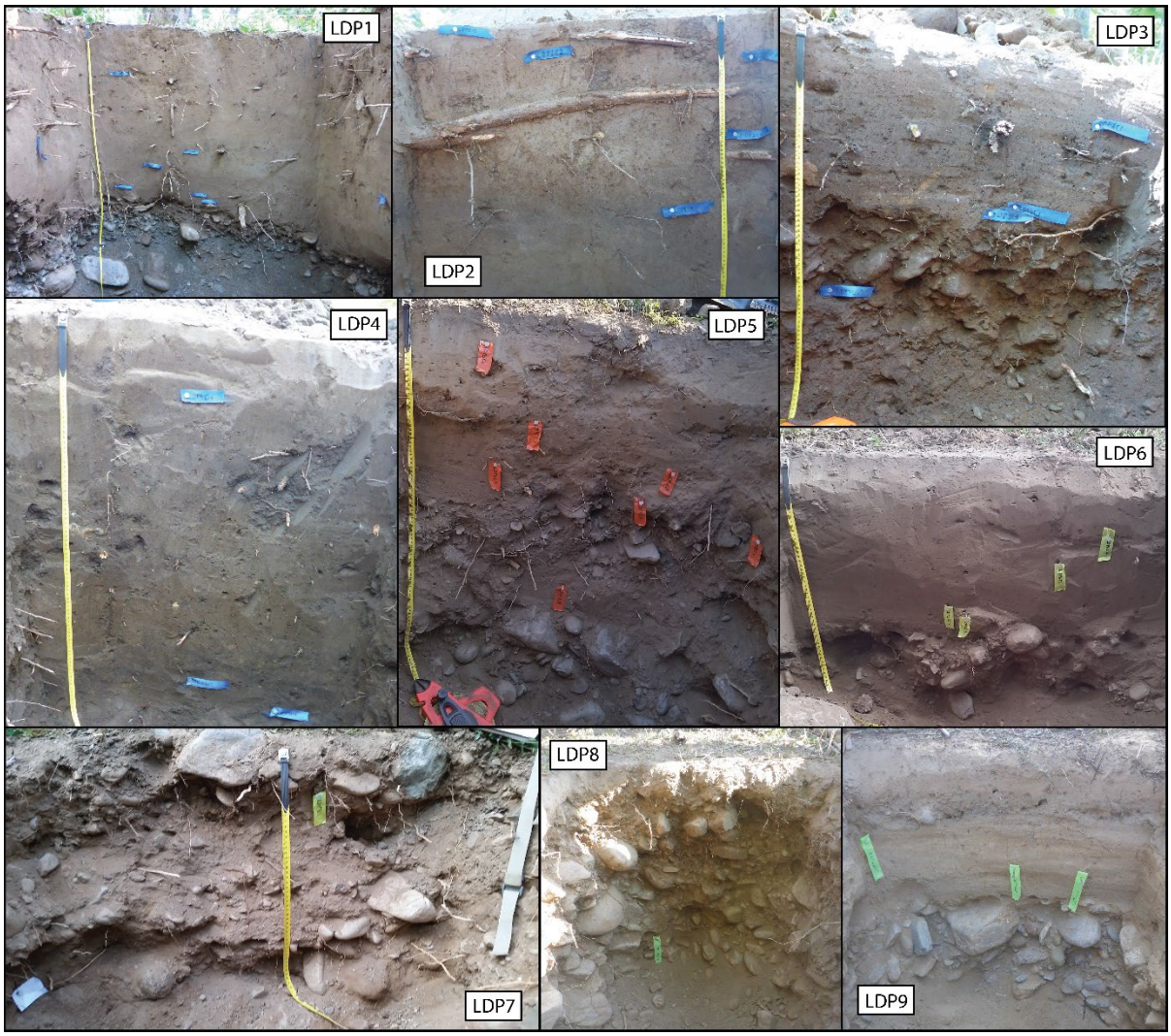

Figure 4.6: Terrace pit stratigraphy at Lal Dhang. Photographs of pits excavated on terraces adjacent to the Rawasan River show the stratigraphy of these surfaces. Detrital charcoal collection locations are tagged. Radiocarbon dates associated with these samples can be found in Figure 4.7.

detrital charcoal sample collected from a depth of 33 cm in LDP3 produced a 2σ PDF date range of 1320-1440 CE, which corresponds with the age of the sample from LDP1. Pit 5 (LDP5), at an elevation of 334 m, yielded a 2σ PDF date range of 1646-1927 CE at a depth of 34 cm, and pit 6 (LDP6), which is approximately equivalent in elevation to LDP2 (336 m), produced a 2σ PDF date range of 1445-1632 CE at a depth of 34 cm, which corresponds to

the age of the sample from LDP2. Pit 7 (LDP7) was excavated at the top of a linear structural feature that is referred to locally as the Muhabharat mound (Figure 4.4c), which is offset from the surrounding terrace surface with a maximum elevation of 338 m. The strata exposed in LDP7 is primarily gravel, which made charcoal collection difficult, but a sample located at a depth of 1.15 m produced a 2σ PDF date range of 129-531 CE, which is the oldest sample produced within any of the pits or trenches. Two additional pits were excavated to the south of the river on terraces that lie adjacent to the terrace above the fault scarp. Pit 8 (LDP8), at an elevation of 331 m, produced a 2σ PDF date range of 1646-1926 CE, which is approximately equivalent to the date range established for LDP5. Pit 9 (LDP9), at an elevation of 325 m, was excavated on the lowest terrace that lies within the current floodplain. A charcoal sample collected from LDP9 gave a 2σ PDF date range of 1958-2000 CE. Locations of the pit excavations, along with the respective pit elevations and radiocarbon results are provided in Figure 4.7.

A foot survey along the river focused on areas where sheared, Lower Siwalik sandstone form natural outcrops. Photos of these outcrops can be viewed in Figure 4.4. Special attention was given to clear an exposure along the river cut to determine if the Tertiary Siwalik units overlie the Quaternary fluvial sediments at this location, but no such relationship could be confirmed. An additional foot survey was conducted to the southeast of the trench site near an outcrop of Siwalik mudstone, which underlies the sandstone in the undeformed Siwalik sequence. During the survey, an abandoned, hanging channel cross-section was observed, which demonstrated that a river previously flowed approximately east-northeast to west-southwest at this location (Figure 4.4d). This abandoned channel is located

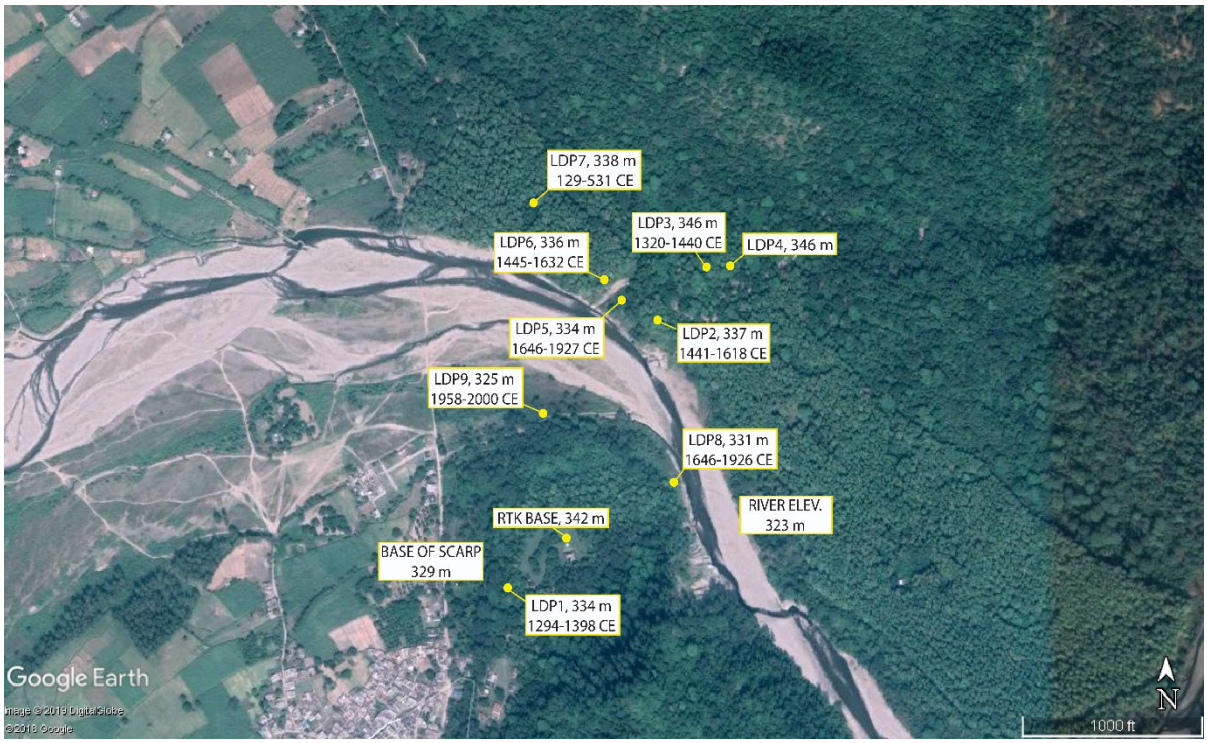

Figure 4.7: Locations, elevations, and radiocarbon age results for terrace pits at Lal Dhang. Radiocarbon results were individually calibrated using the OxCal software program, and 2σ probability distribution function (PDF) results are reported.

to the southeast of the current course of the Rawasan River and may be evidence of an earlier segment of the river that was truncated and offset during cumulative oblique ruptures of the HFT that caused channel migration to the northwest.

Discussion

Based on the findings of the topographic survey and the test pit excavations described above, there are at least two distinct phases of tectonic uplift evidenced at Lal Dhang. The first of these phases uplifted a set of terraces during the time period of ~1294-1440 CE, which is coincident with the 1344 CE historical earthquake, and the second uplifted a younger set of terraces in the time period of ~1441-1632 CE, which corresponds with the

1505 CE earthquake. A third stage of uplift may have occurred for terraces in the time period of ~1646-1927 CE, but this is debatable and could be attributed to local fluvial deposition and incision. The history of terrace uplift described above, which is defined by the radiocarbon ages of the respective surfaces, supports the rupture sequence revealed within the paleoseismic trench, strengthening the argument for a multiple earthquake scenario at the site. With consideration given to ongoing floodplain sedimentation and cut-and-fill terrace development, it appears that the 1344 CE event produced approximately 5-7 meters of vertical separation between adjacent terraces. This event was followed by the capture and subsequent downcutting of the Rawasan River, and a subsequent phase of terrace uplift of approximately 5-7 meters in the earthquake of 1505 CE. Roughly equivalent vertical separation values for the 1344 CE and 1505 CE events indicate that coseismic slip amounts, and perhaps magnitudes, of the two earthquakes may have been similar, as suggested by published magnitude estimates for the two events (Mugnier et al., 2013; Bilham, 2019).

These data provide an important supplement to the paleoseismic trenching study, as coseismic slip during the 1505 CE earthquake could not be firmly established within the trench due to several factors, including: ambiguous contacts between adjacent gravel units where slip could not be precisely measured, an inability to measure contacts that continued beyond the bounds of the trench, and erosion of deformational features following the event. If coseismic slip in the second earthquake was similar to the first, then the total slip would increase from ~25.5 m to ~31.5 m for the combined events. This amount of slip would account for the entire 9-10 m of vertical separation that forms the fault scarp at Lal Dhang.

An interesting dichotomy exists between the topographic expressions of the uplifted

terraces to the north of the river, and the fault scarp to the south of the river at Lal Dhang. On the north side, a stepped sequence of terraces decreases in elevation and youngs toward the foreland, with the higher terrace producing abandonment dates between ~1294-1440 CE and progressively lower terraces producing abandonment dates of ~1441-1632 CE and ~1646-1927 CE, which would appear to support an in-sequence faulting scenario. However, on the south side, the intermediate terrace step that reflects abandonment during the period that correlates to the 1505 CE earthquake does not exist, and the deformation uncovered in the paleoseismic trench suggests an out-of-sequence faulting progression.

To rectify these apparent disparities, erosional forces must be considered alongside coseismic deformation and uplift. The scenario that best fits the paleoseismic and geomorphic evidence at Lal Dhang includes an initial vertical separation of ~5-7 meters occurring during an earthquake between ~1294-1440 CE, followed first by preferential erosion of this newly formed terrace on the north side of the river as it cut down through a new topographic high, and then by a second out-of-sequence episode of ~5-7 meters of coseismic uplift between ~1441-1632 CE. The terraces from this second episode of uplift are only observable on the north side of the river because the pre-existing terrace had been cut back only on the north side. The vertical separation associated with this terrace is concealed on the south side because it is an out-of-sequence progression with uplift occurring in the hanging wall of a pre-existing fault, and therefore the vertical separation for the two events is reflected cumulatively in one terrace surface. Whether this same type of progression occurred between the second episode of uplift and the formation of the terraces abandoned between ~1646-1927 CE is unclear, but possible.

Because the HFT at Lal Dhang is oriented at an acute angle to the average direction of convergence, a significant degree of obliquity in the fault plane slip vector is expected at this location. Strike-slip tear faults that accommodate strain differentials between segments of the fault may also preferentially develop in these areas. A lengthy lineament viewable on satellite imagery at the site of Lal Dhang (Figure 4.8) indicates that there may be a right-lateral strike-slip component to the seismic motion at the site. The linear nature of this feature indicates a high angle of dip, which is inconsistent with thrust faults and suggests that this trace could delineate a tear fault that may or may not be currently active. A satellite view of this feature reveals that the orientation of the scarp front changes at the site of Lal Dhang (Figure 4.8), which may lend support to the hypothesis that a tear fault has developed in this area to at least partially accommodate the strain differential across two segments of the fault. Additionally, Lal Dhang is located in a recess between two areas where anticlinal folding has begun in the foreland. This recess lines up precisely with Delhi and Haridwar, which could be evidence that an under-riding structural feature of the Indian plate called the Delhi-Haridwar ridge may be driving segmentation of the fault and creating a boundary proximate to Lal Dhang. The lineament appears to offset the Rawasan river and crosses the Muhabharat mound which may be a remnant of a pressure ridge from a previous rupture of the fault. The Rawasan River takes a large step at Lal Dhang that is likely due to diversion around the scarp front following uplift and/or an along-strike component of slip on the fault that offsets the river laterally over time. This lateral migration is further evidenced by the abandoned hanging channel identified during the foot survey, which is located to the southeast of the fault scarp (Figure 4.4d). If this lineament does represent a tear fault, the interaction between

Figure 4.8: Orientation of the HFT at the site of Lal Dhang. a) Lal Dhang is located at a point along the HFT where the strike of the fault plane changes. This intersection also lies along a transverse feature in the under-riding Indian plate known as the Delhi-Haridwar Ridge. b) Lineament at the site of Lal Dhang that indicates a significant along-strike component of slip.

this feature and adjoining segments of the HFT warrants further research, as well as its effects on local seismic processes and landscape development.

This preferred geomorphological model suggests that two distinct phases of uplift occurred at Lal Dhang during two, great Late Medieval earthquakes in 1344 CE and 1505 CE. Evidence for both of these events was also revealed in an associated paleoseismic trench excavated across the ~10-m-high fault scarp to the south of the river. An illustration of the deformational features observed in the paleoseismic trench can be viewed in Figure 4.9. The

sequence exposed in the trench includes three stacked, recumbent folds. The lower two folds are continuous and occurred in a single event, however the uppermost anticline cuts the intermediate anticline during rupture in a second event, which demonstrates out-of-sequence thrusting in the earthquake of 1505 CE. The terrace level (~337 m) that corresponds to the 1505 CE event does not appear to exist at the scarp front on the south side due to an out-of-sequence thrust fault progression that is evidenced by the deformational sequence observed in the trench exposure. This terrace is only apparent on the north side because the previously formed terrace (~346 m) that corresponds to the 1344 CE event was preferentially eroded on the north side of the river between the events. The 1505 CE event is not recorded in a terrace surface to the south of the river because in this location it ruptured the scarp behind the fault splay that was generated in the 1344 CE event.

Philip, et al. (1992) outlined several models for fault scarp generation based on deformation observed following the Armenian earthquake of 1988 in the fold-and-thrust belt at the front of the Lesser Caucasus Mountains. Three of these models include the development of pressure ridges that form fault scarps composed of folded, unconsolidated sediments due to motion on a bedrock fault behind the scarp front. Because a sheared Lower Siwalik sandstone outcrop lies behind the scarp front at Lal Dhang, and because only folded sequences of unconsolidated fluvial and floodplain sediments were observed within the trench, it is likely that such a model applies to fault scarp generation at the site. This could explain the out-of-sequence thrust fault progression in the trench between the 1344 CE and 1505 CE events. The trench exposure appears to reveal a pressure ridge that formed when the Siwalik sandstone ruptured and thrust a pre-existing cut-and-fill terrace forward through

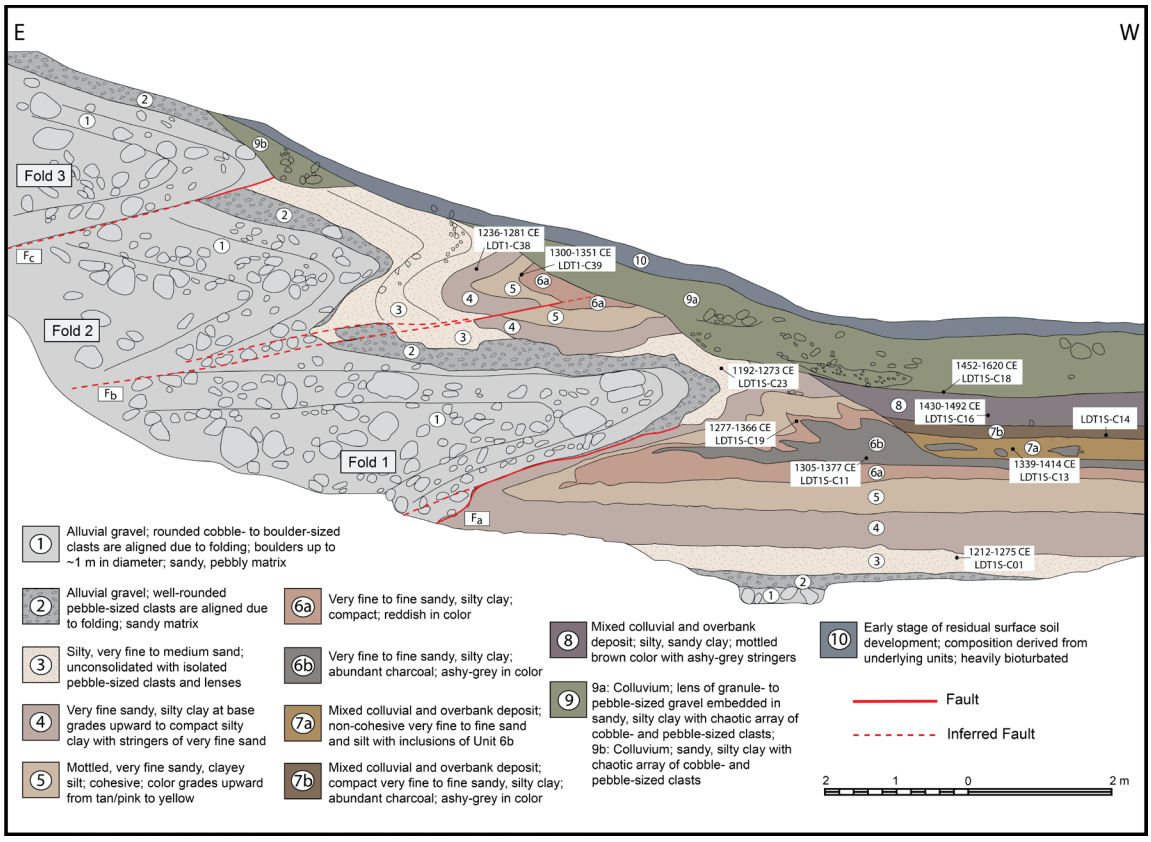

Figure 4.9: Trench log produced in a corresponding paleoseismological study at Lal Dhang.

frictional sliding along a fault plane in the underlying fluvial gravel, folding and uplifting the adjacent floodplain deposits in the hanging wall of the fault. A subsequent reactivation of the fault in the Siwalik sandstone would be at a higher elevation behind the scarp, potentially causing a change in local stress orientation that could cause the folding and shearing of unconsolidated materials in a second earthquake to occur above and behind the initial pressure ridge front, in an out-of-sequence progression. The same study by Philip et al. (1992) suggests that the type of fault scarp generation changes along the front depending on the orientation of the fault to the remote stress field. This likely also applies to scarp generation along the HFT, although oblique convergence is prominent along the central

Indian section of the front and therefore similar scarp generation mechanics may be at work along much of the area contained within the CSG.

Conclusions

Landscape development along the HFT is complex where rivers intersect the fault, and interactions between fluvial and tectonic processes produce unique topographic features. These locations often provide natural outcrops where faulting relationships can be observed without need for excavation, and the resulting data can be used to support findings uncovered during paleoseismic trenching investigations. Lal Dhang is located at such an intersection, where sheared Siwalik outcrops and a stepped sequence of terraces preserve the history of uplift and subsequent incision associated with large-magnitude earthquakes on the HFT. A comprehensive geomorphological investigation into the tectonic influences on landscape development at Lal Dhang has generated data that supports the findings of a corresponding paleoseismological study. The specific findings are as follows:

1) At least two phases of terrace uplift occurred at Lal Dhang and are constrained through radiocarbon dating to ~1294-1440 CE, which is coincident with the historically documented 1344 CE earthquake, and ~1441-1632 CE, which corresponds with the 1505 CE earthquake.
2) This uplift sequence lends support to an associated paleoseismological investigation that uncovered evidence of these events in an excavation across an ~10-meter-high fault scarp at the site.
3) The offset of adjacent terraces indicates that ~6 m of vertical separation was produced in each of the 1344 CE and 1505 CE earthquakes suggesting that the coseismic slip,

and therefore the magnitude, of these events may have been similar. This data strengthens the findings of the trenching study, as slip amounts for the 1505 CE earthquake could not be accurately estimated in the trench due to the nature of the observed deformational features and erosion of the scarp following the event.

4) If the earthquakes were similar in magnitude, a more accurate slip estimate might be achieved by doubling the slip observed for the first earthquake, which would increase the total cumulative slip from ~25.5 m to ~31.5 m and would account for the entire ~10 meters of vertical separation along the scarp front at Lal Dhang.
5) A significant component of strike-slip motion is evident at Lal Dhang along a lineament that appears to have offset the Rawasan River and produced a pressure ridge known as the Muhabharat mound.
6) Lal Dhang is situated in a recess that aligns with a structure in the Indian plate known as the Delhi-Haridwar ridge, and the angle of the range front changes at the location of Lal Dhang. This may signify that the site is located proximate to a segment boundary where a significant along-strike component of slip is required to accommodate strain differentials on adjacent segments of the fault.
7) A fault scarp generation model for the site of Lal Dhang is presented here and involves the formation of a pressure ridge in unconsolidated fluvial and floodplain deposits due to fault motion behind the scarp front in the underlying Siwalik sandstone, which may provide an explanation for subsequent out-of-sequence thrust fault progression observed within the trench.

APPENDIX A

SUPPLEMENTARY MATERIALS – CHAPTER 2

Hajipur Trench Site: Malik, et al., 2010

Table 2
Radiocarbon ages.

Location of the sample[f]	Sample number	Lab sample number[a]	$\delta^{13}C$(‰)[e]	Conventional age[b]	Corrected pMC[d]	Radiocarbon age (BP)	Calibrated age 2σ[c]
Unit D	H2a	KIA30702	−27.84 ± 0.13	225 ± 50 BP	97.22 ± 0.59	226 ± 49	cal A.D. 1623–1696 (probability 30.8%) A.D. 1725–1814 (probability 37.6%)
Unit B	H5	KIA30705	−27.78 ± 0.19	550 ± 50 BP	93.39 ± 0.57	549 ± 49	cal A.D. 1302–1370 (probability 44.8%) A.D. 1381–1440 (probability 50.6%)

[a] Samples were processed and measurements were carried out at Leibniz Labor für Altersbestimmung und Isotopenforschung Christian-Albrechts-Universität Kiel.
[b] Conventional ^{14}C ages were calculated according to Stuiver and Polach (1977) with a $\delta^{13}C$ correction for isotopic fractionation based on the $^{13}C/^{12}C$ ratio measured by our AMS-system simultaneously with the $^{14}C/^{12}C$ ratio.
[c] "Calibrated" or calendar ages were calculated using "CALIB rev 4.3" (Dataset 2, 1998 decadal atmospheric data), Stuiver et al. (1998).
[d] "Corrected pMC" indicates the percent of modern (1950) carbon corrected for fractionation using the ^{13}C measurement.
[e] Please note that the $\delta^{13}C$ includes the fractionation occurring in the sample preparation as well as in the AMS measurement and therefore cannot be compared to a mass spectrometer measurement.
[f] Refer trench section Fig. 7b for sample location.

Table 3
OSL dating.

Location of the sample[a]	Sample number	Th-232 (ppm)	U-238 (ppm)	K (%)	De (Gy)[b]	DR (Gy/ka)	Age (ka)[b]
Unit A′	JMT2	17.3 ± 5.0	5.0 ± 1.4	1.5 ± 0.07	9.5 ± 1.0	3.6 ± 0.5	2.6 ± 0.5
Unit B	JMT4	12.3 ± 6.0	8.0 ± 1.0	1.7 ± 0.08	3.2 ± 0.3	4.1 ± 0.5	0.8 ± 0.1
Unit B	JMT5	11.6 ± 5.0	7.0 ± 1.4	1.8 ± 0.09	1.5 ± 0.5	3.9 ± 0.1	0.4 ± 0.1
Unit C	JMT6	8.9 ± 1.8	2.1 ± 0.5	1.96 ± 0.03	1 ± 0.07	2.9 ± 0.02	0.3 ± 0.04

[a] Refer trench section Fig. 7b for sample location.
[b] Equivalent dose (De) computed using minimum plus two sigma, water content assumed to be 10%, cosmic ray dose 150 micro-gray per year. Dating was carried out at Physical Research Laboratory, Ahmedabad. India.

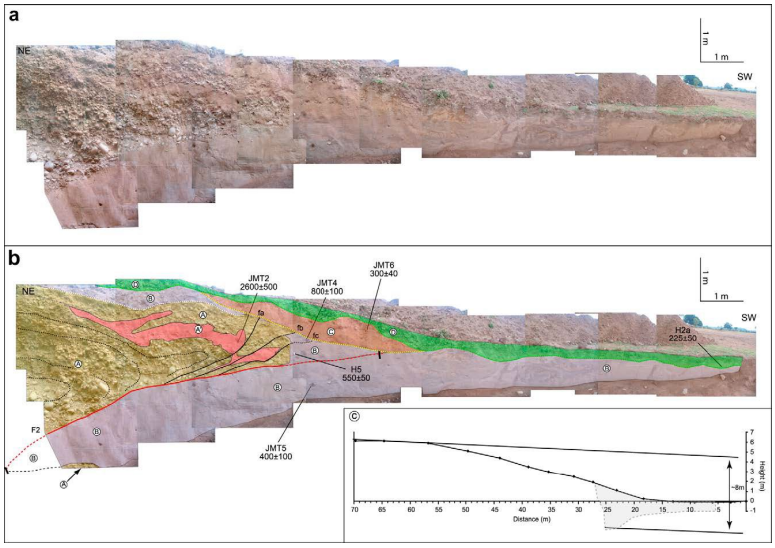

Fig. 7. (a) North facing wall of 18 m long trench section excavated across Hajipur fault (HF2), (b) The trench wall revealed only F2 strand. The exposed successions show four major lithounits. Unit A – gravel deposits and A0 is sandy unit embedded within the grave unit, Unit B – massive sand unit, Unit C comprising medium to coarse sand, and Unit D comprised of medium to fine sand capping the sequence. Both units A–A0 and B have been displaced along the F2 strand. The NE dipping F2 strand is marked with variable dip of w32_ in deeper part of the trench and to w8_ to almost horizontal in the southwest near surface. Total displacement of about 8–9 m (i.e. w7.5 m along the main fault and 1.5 m along the branching faults (f_a, f_b and f_c)) was measured in trench. Location of samples dated by OSL and AMS are marked on the trench, (c) Topographic profile collected with total station shows scarp height of about 6 m. The oldest unit A shows total vertical displacement of about 8 m measured between the top of the exposed gravel in the trench and top on the scarp in the hanging wall. For location refer Figs. 3 and 4.

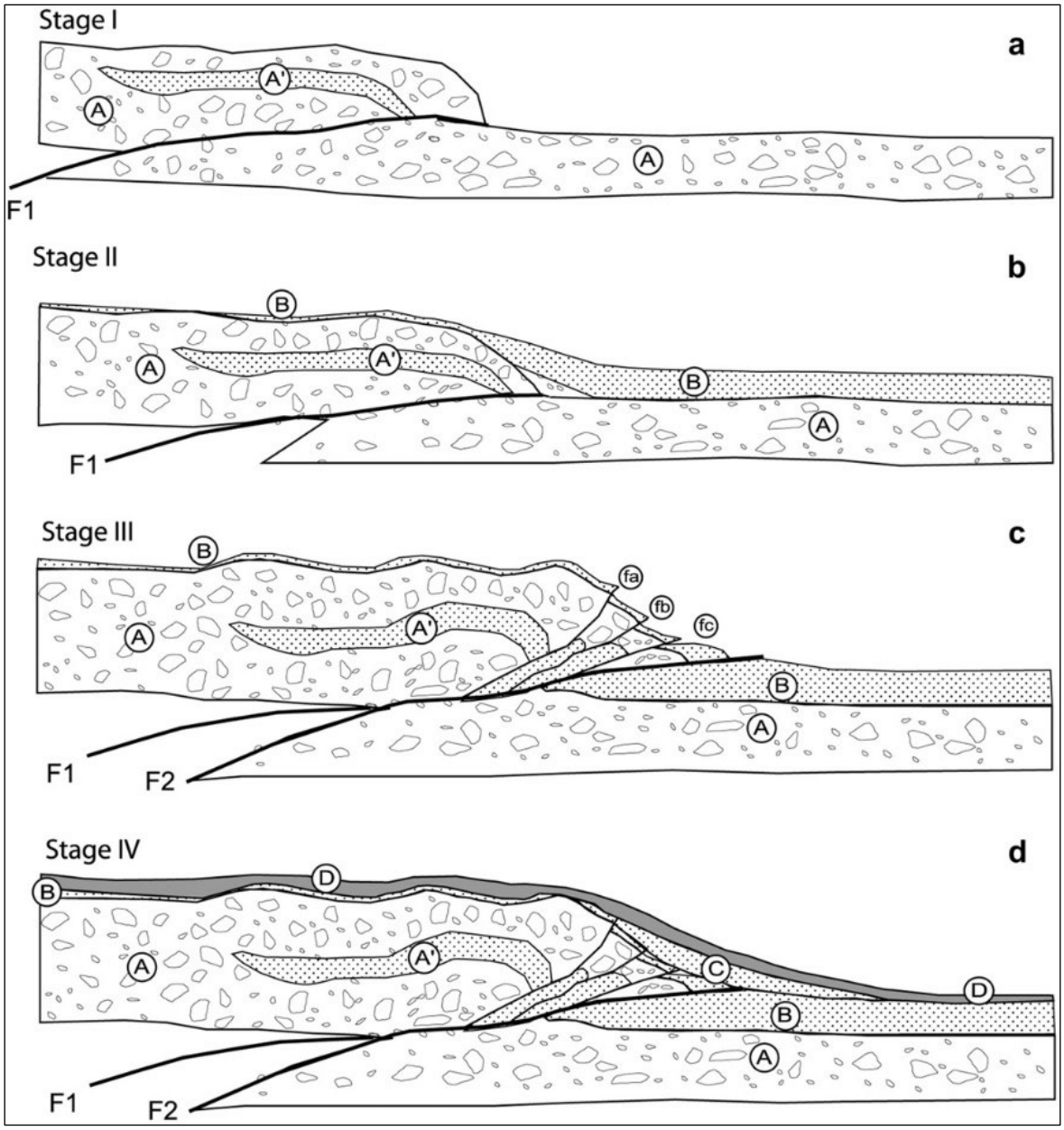

Fig. 8. Schematic view of trench log showing sequence of faulting and depositional phases from Stage I to IV. (a) Stage I: Displacement of unit A–A$_0$ along F1 strand marking Event I, (b) Deposition of unit B, (c) Event II: displacement of unit A–A$_0$ and unit B along new branching out fault strand F2, and (d) deposition of unit C and finally capping by unit D.

Discrepancies between schematic view and trench log (continuity of Unit B). Penultimate trace (F1) is known only through GPR study and merges with most recent trace (F2) at 5m depth. The depth of the trench log is only approx. 4m so Fault 1 should not be shown in the schematic at this scale. In this trenching study, there is only evidence for the most recent event.

Run: /Hajipur_RC_Only.oxcal

```
Sequence("Hajipur")
{
 Boundary();
 Phase("Unit B")
 {
  R_Date("H5", 549, 49);
 };
 Date("Event");
 Phase("Unit D")
 {
  R_Date("H2a", 226, 49);
 };
 Boundary();
};
```

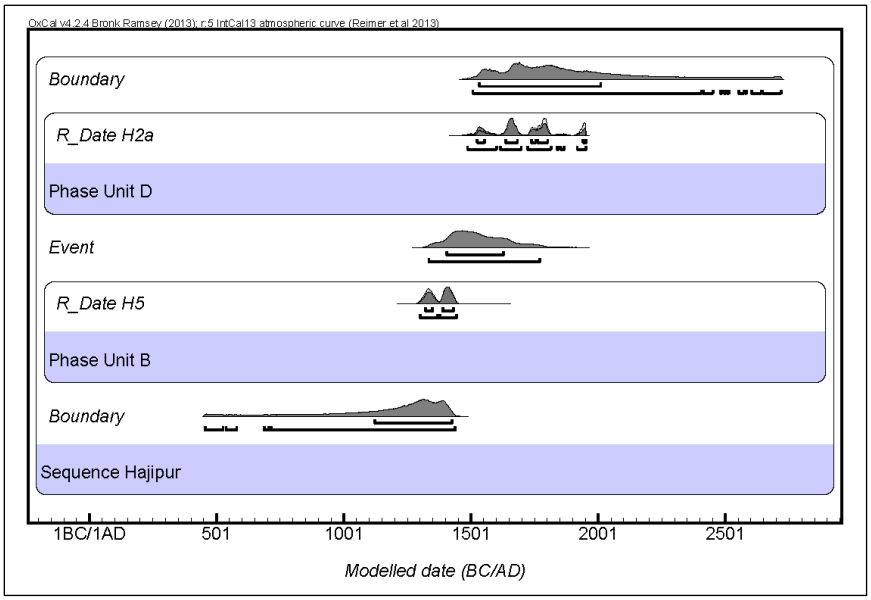

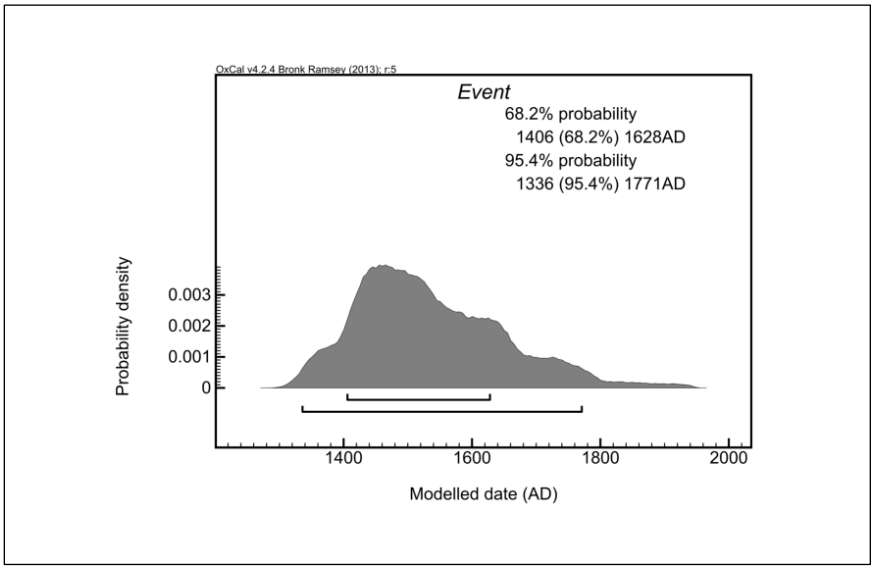

Bhatpur Trench Site: Kumahara and Jayangondaperumal, 2013

Table 1
Radiocarbon data.

Location	Sample	Lab number[a]	$\delta^{13}C$ (‰)	^{14}C age[b] ($\pm 2\sigma$)	Calendar age range[c] ($\pm 2\sigma$)
Unit 3	BHA-103	Beta-277869	−25.7	780 ± 40	A.D. 1200–1280
Unit 5	BHA-117	Beta-277871	−25.0	480 ± 40	A.D. 1400–1460
Unit 3	BHA-118	Beta-277872	−24.8	680 ± 40	A.D. 1270–1320, 1350–1390
Unit 3	BHA-004	Beta-279001	−23.2	600 ± 40	A.D. 1290–1420
Unit 3	BHA-114	Beta-279002	−24.7	490 ± 40	A.D. 1400–1450

[a] Samples are processed and ^{14}C measurements are performed at Beta Analytic Radiocarbon Dating Laboratory.
[b] Reported ^{14}C ages use Libby's half-life of 5568 years, relative to A.D. 1950.
[c] IntCal04 is used for calculation of calendar age.

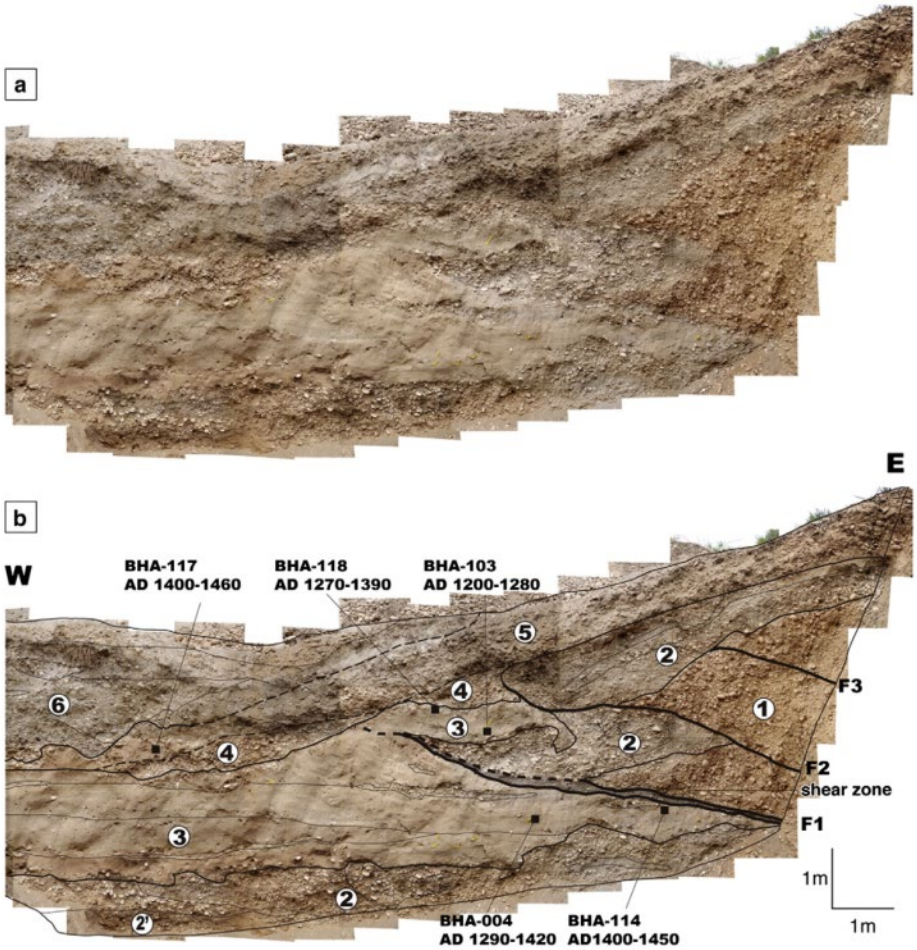

Fig. 6. (a) Photo mosaic of north wall of the Bhatpur Trench. (b) Photo is with interpreted geologic boundaries and faults.

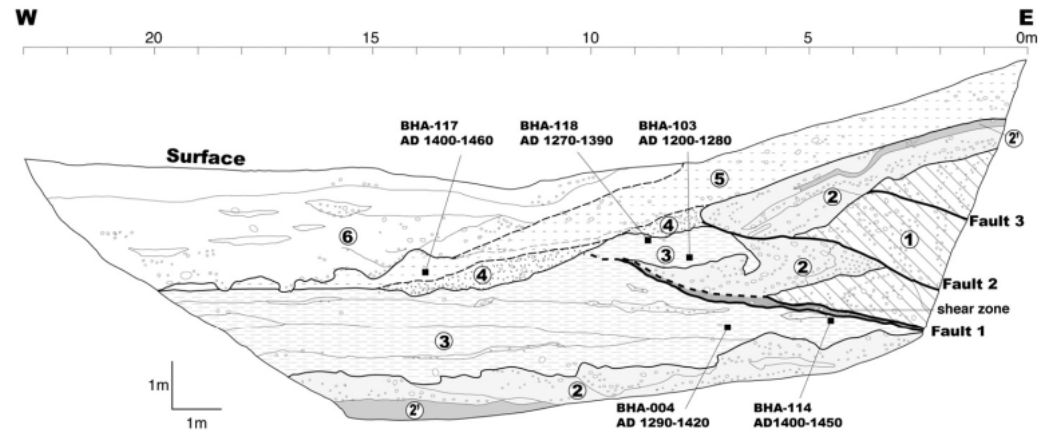

Fig. 5. Log of north wall of the Bhatpur Trench. Circled numbers denote major stratigraphic units discussed in the text. Faults 1 to 3 are three fault strands exposed in the trench. Detrital charcoal samples are denoted by black squares. No vertical exaggeration.

Run: /Bhatpur.oxcal

```
Plot()
{
 Sequence("Bhatpur")
 {
  Boundary();
  Phase("Unit 3")
  {
   R_Date("BHA-103", 780, 40);
   R_Date("BHA-118", 680, 40);
   R_Date("BHA-004", 600, 40);
   R_Date("BHA-114", 490, 40);
  };
  Date("Event");
  Phase("Unit 5")
  {
   R_Date("BHA-117", 480, 40);
  };
  Boundary();
 };
};
```

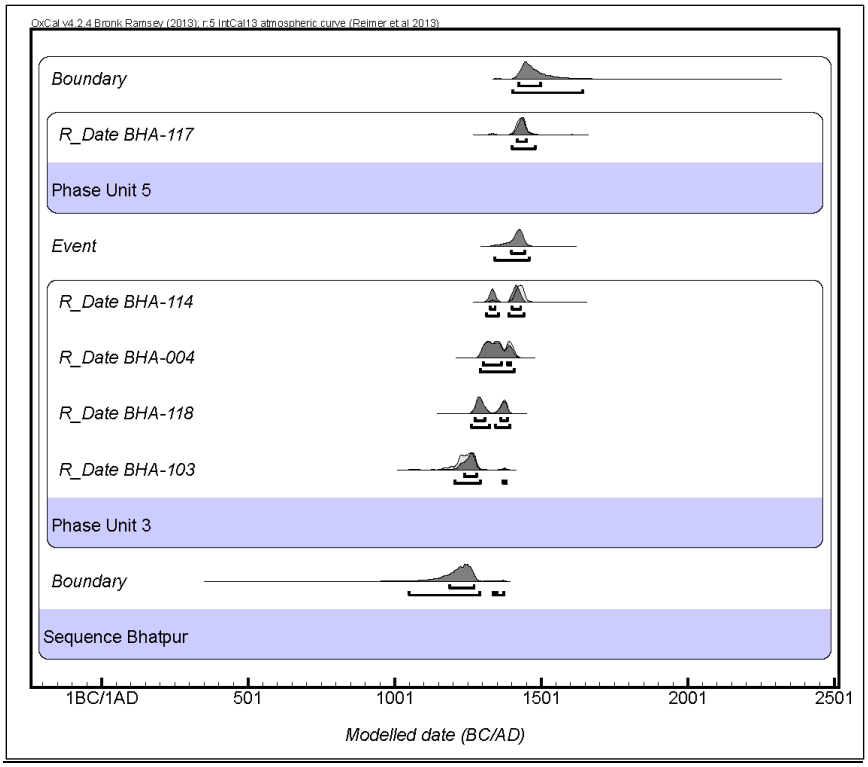
OxCal v4.2.4 Bronk Ramsey (2013); r:5 IntCal13 atmospheric curve (Reimer et al 2013)
Boundary
R_Date BHA-117
Phase Unit 5
Event
R_Date BHA-114
R_Date BHA-004
R_Date BHA-118
R_Date BHA-103
Phase Unit 3
Boundary
Sequence Bhatpur
1BC/1AD
501
1001
1501
2001
2501
Modelled date (BC/AD)

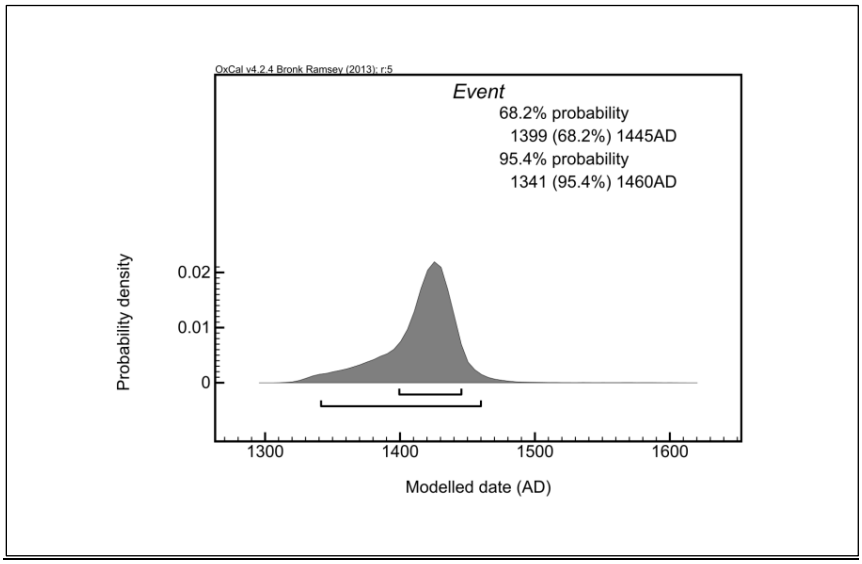
OxCal v4.2.4 Bronk Ramsey (2013); r:5
Event
68.2% probability
1399 (68.2%) 1445AD
95.4% probability
1341 (95.4%) 1460AD
Probability density
0.02
0.01
0
1300
1400
1500
1600
Modelled date (AD)

Chandigarh Trench Site: Kumar, et al., 2006, (RC Data table modified to include Chandigarh only.)

Table 1. Radiocarbon Data

Location	Sample	CAMS Number[a]	$\delta^{13}C$[b]	^{14}C age[c] (±2σ)	Calendar Age Range,[d] Calendar Years B.C. and A.D. (±2σ)
			Trench Samples (Site 1)		
Unit 7	PAN-17	94616	25.0	215 ± 35	A.D. 1637–1688, 1729–1810, 1922–1949
Unit 7	PAN-11	94615	−25.0	310 ± 40	A.D. 1482–1654
Unit 7	PAN-09	94614	−25.0	230 ± 40	A.D. 1522–1576, 1626–1689, 1729–1811, 1922–1949
Unit 6	PAN-03	94612	−25.0	150 ± 40	A.D. 1665–1784, 1790–1890, 1909–1950
Unit 6	PAN-01	97126	25.0	535 ± 35	A.D. 1315–1354, 1387–1441
Unit 6	PAN-02	94611	−25.0	665 ± 40	A.D. 1279–1330, 1341–1397
Unit 6	PAN-27	94619	25.0	1250 ± 40	A.D. 683–884
Unit 4	PAN-23	94617	25.0	595 ± 40	A.D. 1299–1413
Unit 4	PAN-26	94618	−25.0	440 ± 50	A.D. 1404–1523, 1564–1628
Unit 4	PAN-05	97127	25.0	1115 ± 35	A.D. 783–789, 827–840, 863–1002, 1011–1016
Unit 4	PAN-08	94613	25.0	2445 ± 50	762–678, 671–607, 601–404 B.C.

[a]Samples are processed and ^{14}C measurement are performed at Center for Accelerator Mass Spectrometry (CAMS) at Lawrence Livermore National Laboratory.
[b]The $\delta^{13}C$ values are the assumed values according to *Stuvier and Polach* [1977] when given without decimal places. Values measured for the material itself are given with a single decimal place.
[c]Reported ^{14}C ages use Libby's half-life of 5568 years, relative to A.D. 1950.
[d]Dendrochronologically calibrated age ranges were calculated with the University of Washington calibration program Calib 4.4, using the intercepts method [*Stuiver and Reimer*, 1993; *Stuiver et al.*, 1998], and age ranges are often discontinuous.
[e] Reported radiometric dates are obtained from *Kumar et al.* [2001].

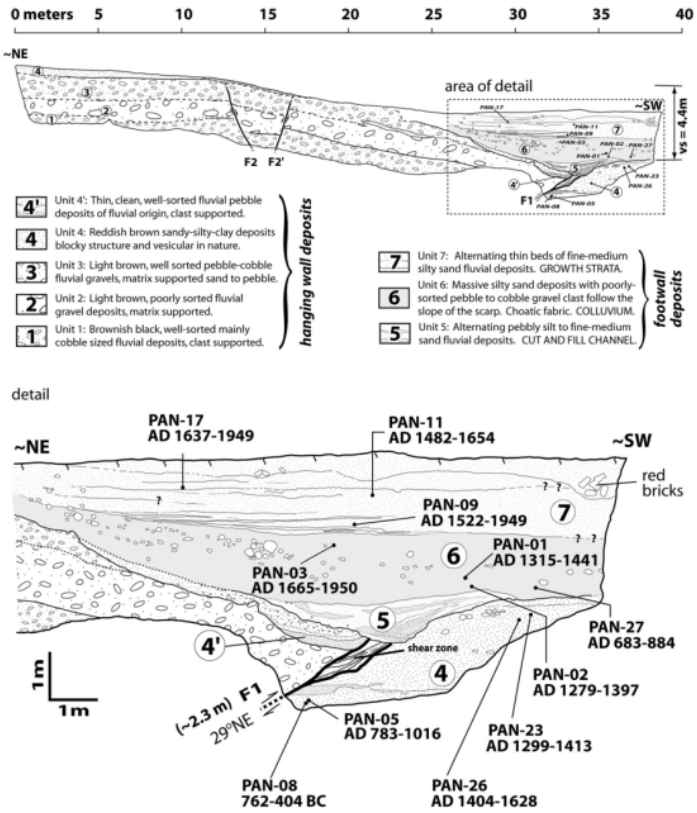

Figure 6. Chandigarh trench log (site 1). Outlined in the box is a portion of the trench enlarged to show details of cross-cutting relationship and radiocarbon sample locations (see Figures 3 and 4 for location).

Run: /Chandigarh_No_Outliers.oxcal

```
Sequence("Chandigarh")
{
 Boundary( );
 Curve("IntCal13","IntCal13.14c");
 Phase("Unit 4")
 {
  R_Date("PAN-08", 2445, 50);
  R_Date("PAN-05", 1115, 35);
  R_Date("PAN-23", 595, 40);
 };
 Date("Event")
 {
 };
 Phase("Unit 6")
 {
  R_Date("PAN-02", 665, 40);
  R_Date("PAN-01", 535, 35);
  R_Date("PAN-03", 150, 40);
 };
 Phase("Unit 7")
 {
  R_Date("PAN-09", 230, 40);
  R_Date("PAN-17", 215, 35);
 };
 Boundary( );
};
```

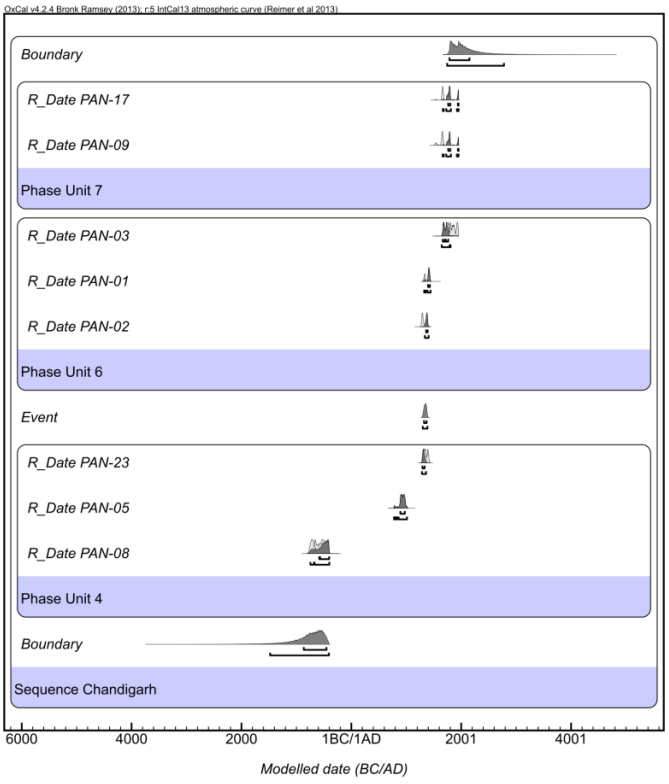

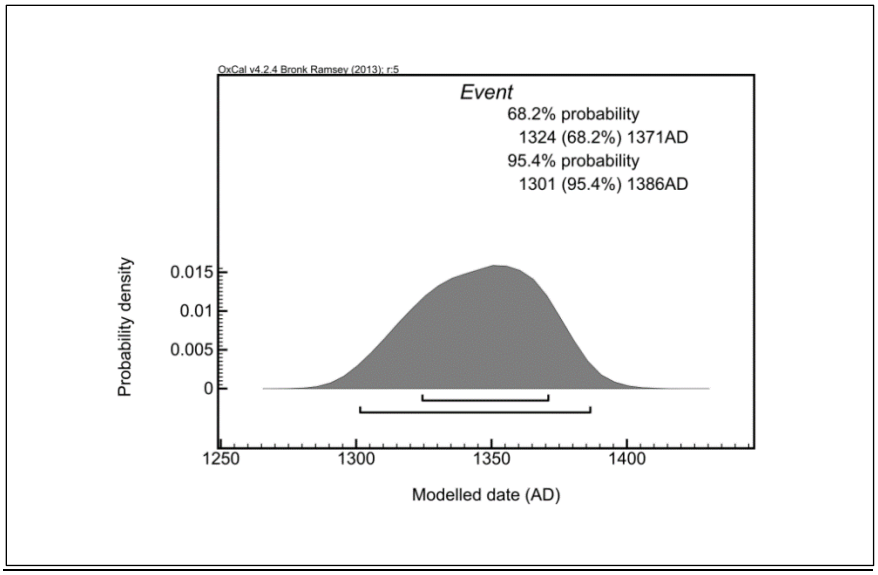

Kala Amb Trench Site: Kumar, et al., 2001

Table 1. Radiocarbon analyses of charcoal samples from trench (see Fig. 4 for sample location).

Location	Sample no. and Laboratory no.*	$\delta^{13}C$	^{14}C age† (1σ)	Calendar age range‡ in calender years A.D./B.C.) (2σ)
		Trench samples		
Unit 3	C-24 (71081)	−28.2	Modern	Modern
Unit 3	C-22 (71079)	−25.3	230 ± 40	1530–1947 A.D.
Unit 3 (Qb2)	C-15 (71076)	−25.1	420 ± 40	1423–1519, 1593–1622 A.D.
Unit 3	C-13 (71075)	−11.4	650 ± 40	1281–1402 A.D.
Unit 3 (Qb1)	C-18 (72127)	−25.8	620 ± 30	1294–1405 A.D.
Unit 3	C-21 (71078)	−25	680 ± 50	1262–1399 A.D.
Unit 3	C-14 (72126)	−25.6	920 ± 30	1021–1217 A.D.
Unit 3	C-19 (72128)	−26.7	940 ± 40	1017–1211 A.D.
Unit 2	C-53 (77315)	−25	1390 ± 70	539–775 A.D.
Unit 2	C-26 (71082)	−24.6	1420 ± 40	559–673 A.D.
Unit 2	C-50 (77313)	−25	1450 ± 50	535–665 A.D.
Unit 2	C-27 (71083)	−24.5	1470 ± 40	534–657 A.D.
Unit 2	C-5 (71074)	−24.1	1520 ± 40	429–639 A.D.
Unit 2	C-2 (71073)	−24	1600 ± 40	385–558 A.D.
Unit 2	C-52 (77314)	−25	1630 ± 50	261–541 A.D.
Unit 2	C-23 (71080)	−25	1900 ± 60	38 B.C. to 243 A.D.
		Terrace samples		
Terrace	MT001-5 (77316)	−25	4300 ± 40	3015–2878 B.C.
Terrace	MT001-3 (73705)	−28.4	4410 ± 40	3325–2915 B.C.

*CAMS; Center for Accelerator Mass Spectrometry, Lawrence Livermore National Laboratory. †Reported ^{14}C ages use Libby's half-life (5568 years). Delta ^{13}C values are assumed when given without decimal places. ‡Dendrochronogically calibrated age ranges were calculated with the University of Washington calibration program Calib 4.2, using the intercepts method (*20*), and age ranges are often discontinuous. Discrete intervals provided only for Qb1 and Qb2.

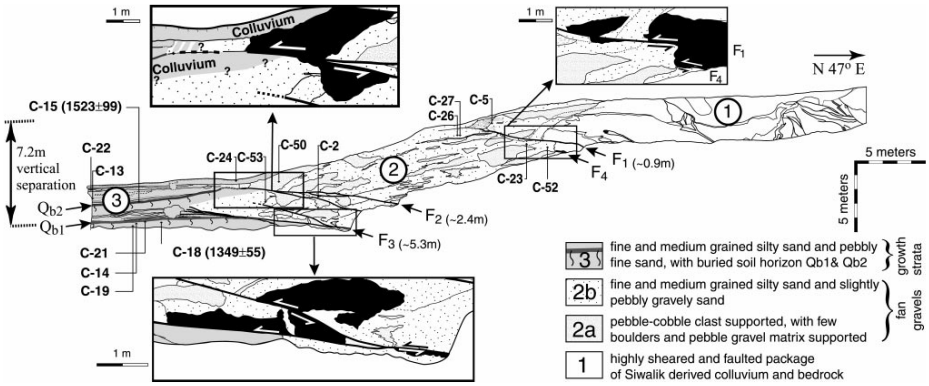

Fig. 4. Map of trench wall showing fault traces (bold), amount of offsets (parentheses, in meters), and radiocarbon sample locations and labels. Dendrochronologically corrected calendar age ranges in years B.C./A.D. are shown for sample C-18 and C-15. Locations of discrete displacements on traces F1, F2, and F3 are enlarged in insets. The units used to measure fault offset are shaded black in the insets.

Run: /Kala_Amb.oxcal

```
Sequence("Kala Amb")
{
 Boundary();
 Phase("Unit 2")
 {
  R_Date("C-23", 1900, 60);
  R_Date("C-52", 1630, 50);
  R_Date("C-2", 1600, 40);
  R_Date("C-5", 1520, 40);
  R_Date("C-27", 1470, 40);
  R_Date("C-50", 1450, 50);
  R_Date("C-26", 1420, 40);
  R_Date("C-53", 1390, 70);
 };
 Phase("Unit 3a")
 {
  R_Date("C-19", 940, 40);
  R_Date("C-14", 920, 30);
  R_Date("C-21", 680, 50);
  R_Date("C-18", 620, 30);
 };
 Date("Event 1");
 Phase("Unit 3b")
 {
  R_Date("C-13", 650, 40);
  R_Date("C-15", 420, 40);
 };
 Date("Event 2");
 Phase("Unit 3c")
 {
  R_Date("C-22", 230, 40);
 };
 Boundary();
};
```

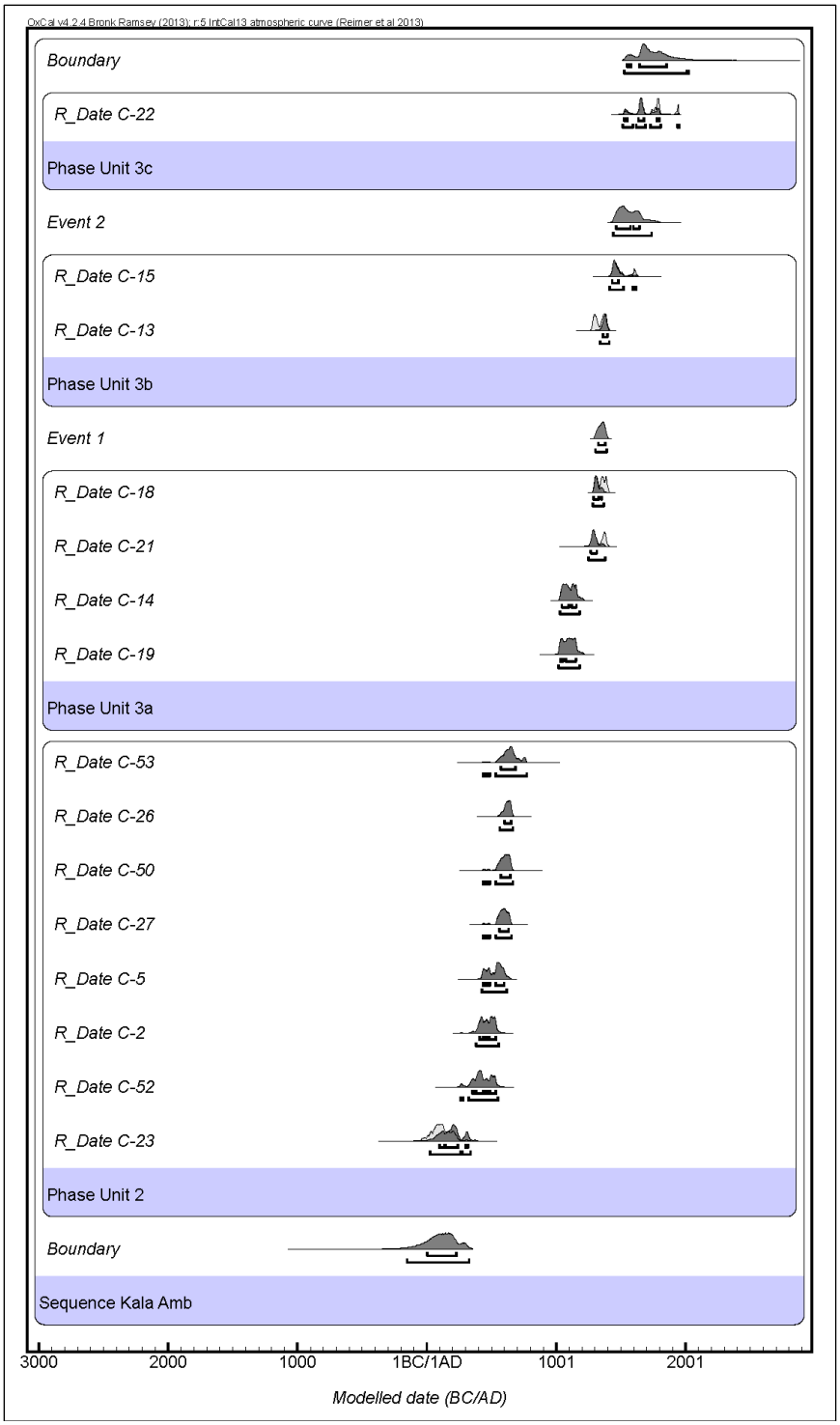
OxCal v4.2.4 Bronk Ramsey (2013); r:5 IntCal13 atmospheric curve (Reimer et al 2013)
Boundary
R_Date C-22
Phase Unit 3c
Event 2
R_Date C-15
R_Date C-13
Phase Unit 3b
Event 1
R_Date C-18
R_Date C-21
R_Date C-14
R_Date C-19
Phase Unit 3a
R_Date C-53
R_Date C-26
R_Date C-50
R_Date C-27
R_Date C-5
R_Date C-2
R_Date C-52
R_Date C-23
Phase Unit 2
Boundary
Sequence Kala Amb
3000
2000
1000
1BC/1AD
1001
2001
Modelled date (BC/AD)

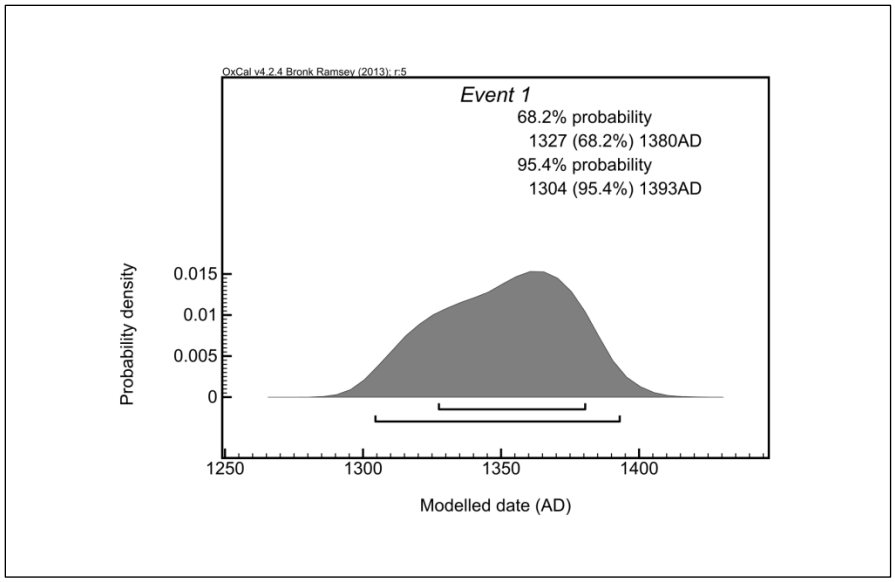

Rampur Ganda Trench Site: Kumar, et al., 2006, (RC Data table modified to include Rampur Ganda dates only.)

Table 1. Radiocarbon Data

Location	Sample	CAMS Number[a]	$\delta^{13}C$[b]	^{14}C age[c] (±2σ)	Calendar Age Range,[d] Calendar Years B.C. and A.D. (±2σ)
			Trench Samples (Site 3)		
Unit 3	AB-08	102806	−25.0	530 ± 35	A.D. 1319 – 1352, 1388 – 1442
Unit 2b'	AB-07	102805	−25.0	730 ± 35	A.D. 1222 – 1301, 1371 – 1380
Unit 2b	AB-18	102807	−25.0	1500 ± 35	A.D. 439 – 452, 463 – 518, 529 – 641

[a]Samples are processed and ^{14}C measurement are performed at Center for Accelerator Mass Spectrometry (CAMS) at Lawrence Livermore National Laboratory.
[b]The $\delta^{13}C$ values are the assumed values according to *Stuvier and Polach* [1977] when given without decimal places. Values measured for the material itself are given with a single decimal place.
[c]Reported ^{14}C ages use Libby's half-life of 5568 years, relative to A.D. 1950.
[d]Dendrochronologically calibrated age ranges were calculated with the University of Washington calibration program Calib 4.4, using the intercepts method [*Stuiver and Reimer*, 1993; *Stuiver et al.*, 1998], and age ranges are often discontinuous.
[e] Reported radiometric dates are obtained from *Kumar et al.* [2001].

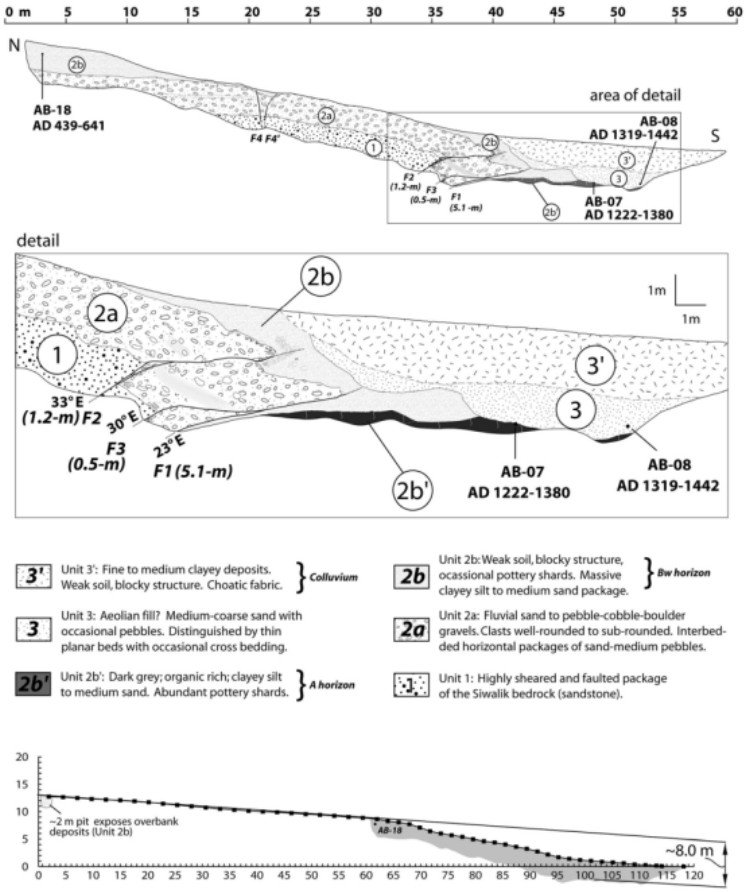

Figure 9. (top) Rampur Ganda trench log (site 3). (center) Detail of southern portion of the trench log. (bottom) Scarp profile across the fault trace. The area of actual trench log (top) with respect to scarp profile is represented as gray shaded polygon (see Figure 7 for location).

Run: /Rampur_Ganda.oxcal

```
Sequence("Rampur Ganda")
{
 Boundary( );
 Curve("IntCal13","IntCal13.14c");
 Phase("Unit 2b'")
 {
  R_Date("AB-07", 730, 35);
 };
 Date("Event")
 {
 };
 Phase("Unit 3")
 {
  R_Date("AB-08", 530, 35);
 };
 Boundary( );
};
```

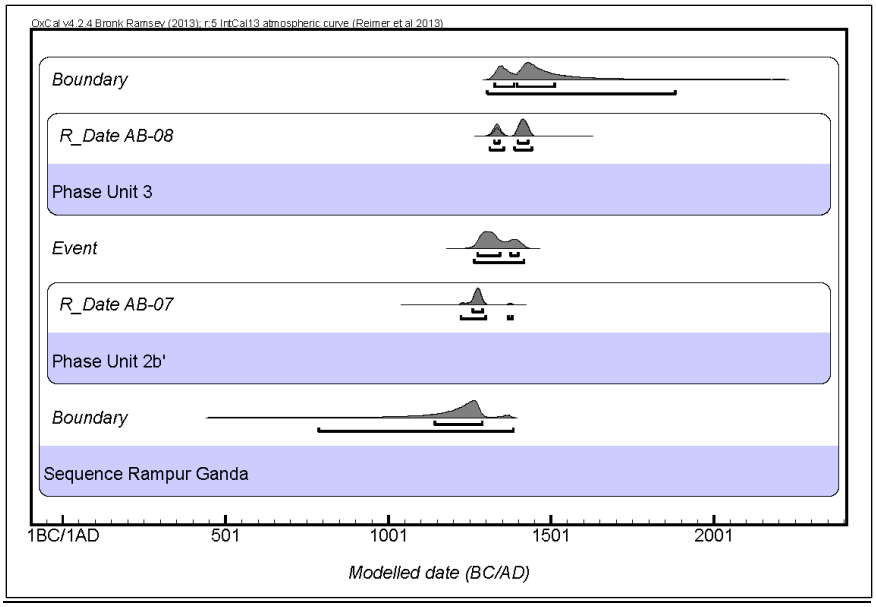
OxCal v4.2.4 Bronk Ramsey (2013); r:5 IntCal13 atmospheric curve (Reimer et al 2013)
Boundary
R_Date AB-08
Phase Unit 3
Event
R_Date AB-07
Phase Unit 2b'
Boundary
Sequence Rampur Ganda
1BC/1AD
501
1001
1501
2001
Modelled date (BC/AD)

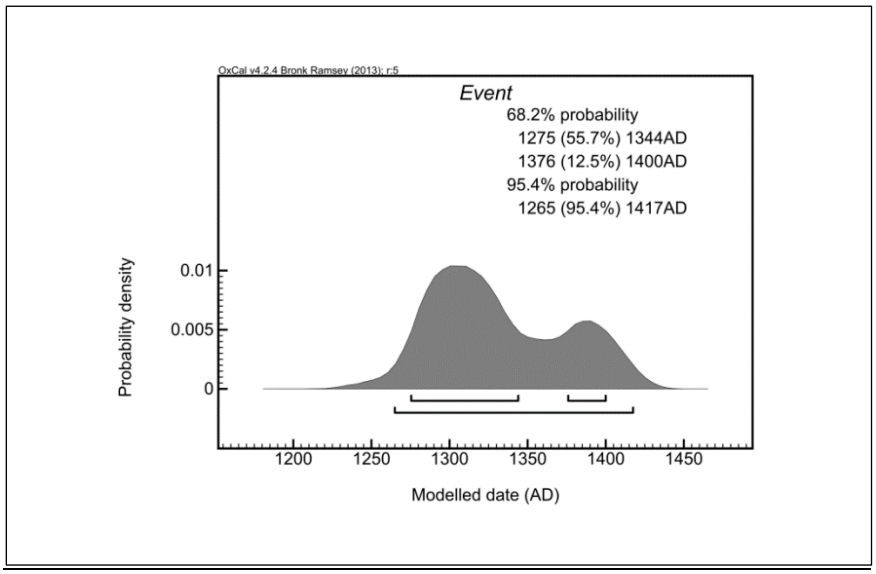
OxCal v4.2.4 Bronk Ramsey (2013); r:5
Event
68.2% probability
1275 (55.7%) 1344AD
1376 (12.5%) 1400AD
95.4% probability
1265 (95.4%) 1417AD
Probability density
0.01
0.005
0
1200
1250
1300
1350
1400
1450
Modelled date (AD)

Lal Dhang Trench Site: Kumar, et al., 2006, (RC Data table modified to include Lal Dhang dates only.)

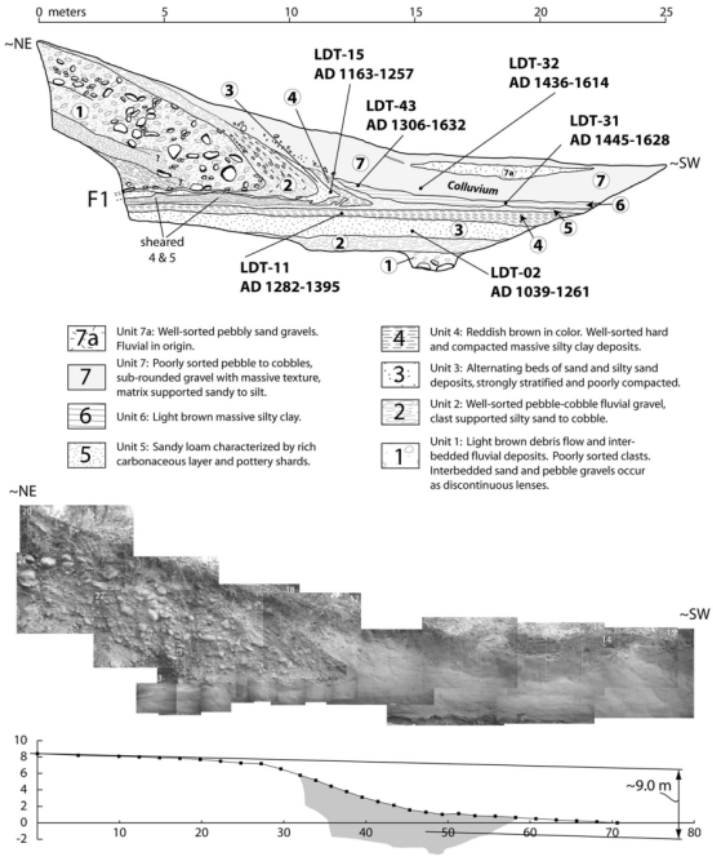

Figure 14. (top) Lal Dhang trench log (site 5). (center) Photo mosaic of the trench log shown at top. (bottom) Scarp profile across the fault trace. The area of Lal Dhang trench log (top) is shown with respect to scarp profile as gray shaded polygon (see Figure 13 for location of trench).

Table 1. Radiocarbon Data

Location	Sample	CAMS Number[a]	$\delta^{13}C$[b]	^{14}C age[c] (±2σ)	Calendar Age Range,[d] Calendar Years B.C. and A.D. (±2σ)
			Trench Samples (Site 5)		
Unit 7	LDT-32	97124	−23.7	410 ± 25	A.D. 1436 – 1512, 1600 – 1614
Unit 6	LDT-43	97125	−25.0	470 ± 70	A.D. 1306 – 1365, 1386 – 1527, 1554 – 1632
Unit 6	LDT-31	97123	−25.2	375 ± 25	A.D. 1445 – 1523, 1564 – 1628
Unit 4	LDT-11	97121	−24.2	660 ± 35	A.D. 1282 – 1329, 1343 – 1395
Unit 3	LDT-15	97122	−24.4	840 ± 20	A.D. 1163 – 1174, 1177 – 1257
Unit 3	LDT-02	97120	−24.6	865 ± 45	A.D. 1039 – 1142, 1150 – 1261

[a]Samples are processed and ^{14}C measurement are performed at Center for Accelerator Mass Spectrometry (CAMS) at Lawrence Livermore National Laboratory.
[b]The $\delta^{13}C$ values are the assumed values according to *Stuvier and Polach* [1977] when given without decimal places. Values measured for the material itself are given with a single decimal place.
[c]Reported ^{14}C ages use Libby's half-life of 5568 years, relative to A.D. 1950.
[d]Dendrochronologically calibrated age ranges were calculated with the University of Washington calibration program Calib 4.4, using the intercepts method [*Stuiver and Reimer*, 1993; *Stuiver et al.*, 1998], and age ranges are often discontinuous.
[e] Reported radiometric dates are obtained from *Kumar et al.* [2001].

```
Sequence("Lal Dhang")
{
 Boundary( );
 Curve("IntCal13","IntCal13.14c");
 Phase("Unit 3")
 {
  R_Date("LDT-02", 865, 45);
  R_Date("LDT-15", 840, 20);
 };
 Phase("Unit 4")
 {
  R_Date("LDT-11", 660, 35);
 };
 Date("Event")
 {
 };
 Phase("Unit 6")
 {
  R_Date("LDT-31", 375, 25);
  R_Date("LDT-43", 470, 70);
 };
 Phase("Unit 7")
 {
  R_Date("LDT-32", 410, 25);
 };
 Boundary( );
};
```

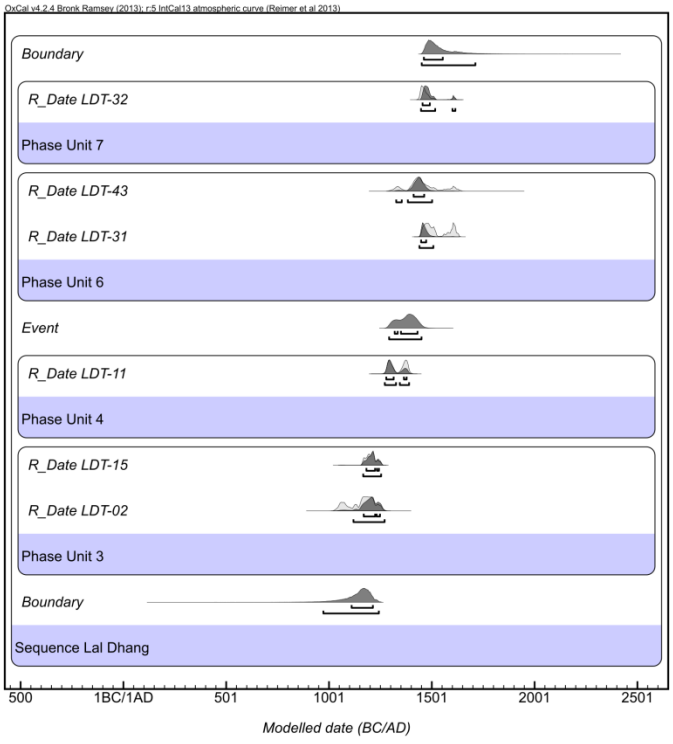

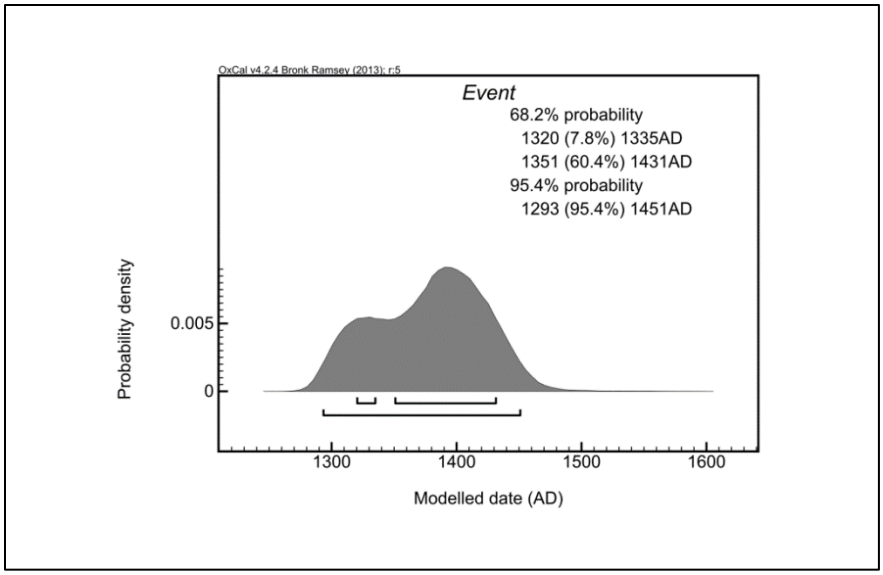

Ramnagar Trench Site: Kumar, et al., 2006, (RC Data table modified to include Ramnagar dates only.)

Table 1. Radiocarbon Data

Location	Sample	CAMS Number[a]	$\delta^{13}C$[b]	^{14}C age[c] (±2σ)	Calendar Age Range,[d] Calendar Years B.C. and A.D. (±2σ)
			Trench Samples (Site 6)		
Unit 5	BR-07	102802	−25.0	565 ± 45	A.D. 1301 – 1371, 1380 – 1433
Unit 4	BR-06	102801	−25.0	695 ± 35	A.D. 1278 – 1323, 1350 – 1390
Unit 3	BR-15	102804	−25.0	700 ± 35	A.D. 1259 – 1322, 1350 – 1390
Unit 2	BR-09	102803	−25.0	990 ± 35	A.D. 984 – 1069, 1080 – 1129, 1136 – 1158

[a]Samples are processed and ^{14}C measurement are performed at Center for Accelerator Mass Spectrometry (CAMS) at Lawrence Livermore National Laboratory.
[b]The $\delta^{13}C$ values are the assumed values according to *Stuvier and Polach* [1977] when given without decimal places. Values measured for the material itself are given with a single decimal place.
[c]Reported ^{14}C ages use Libby's half-life of 5568 years, relative to A.D. 1950.
[d]Dendrochronologically calibrated age ranges were calculated with the University of Washington calibration program Calib 4.4, using the intercepts method [*Stuiver and Reimer*, 1993; *Stuiver et al.*, 1998], and age ranges are often discontinuous.
[e] Reported radiometric dates are obtained from *Kumar et al.* [2001].

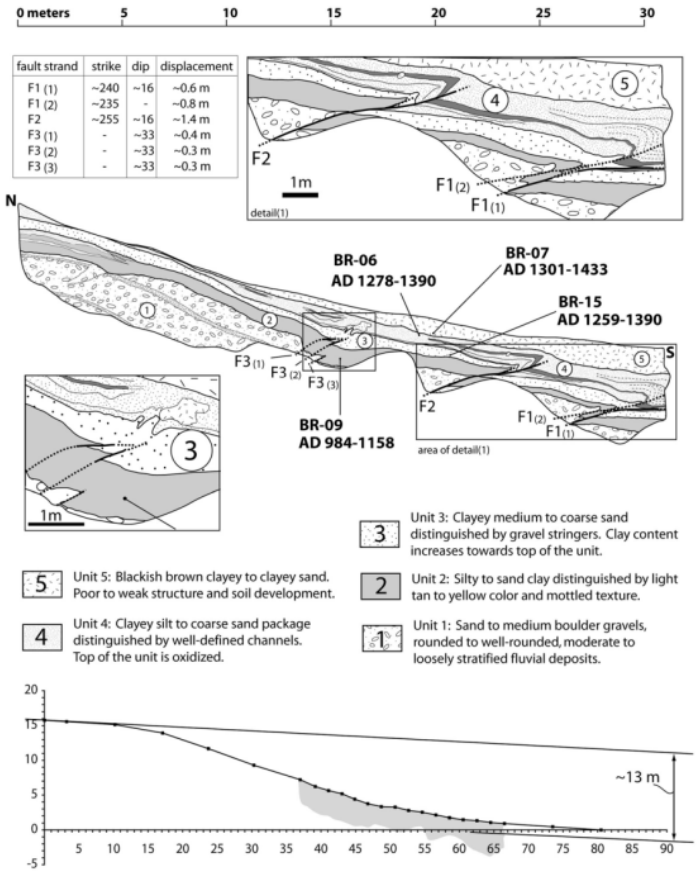

Figure 17. (top) Ramnagar trench log (site 6). Boxes are portion of the trench zoomed in to show discrete offsets of individual fault strands. (bottom) Scarp profile across the fault trace. The area of trench log (top) with respect to scarp profile is represented as gray shaded polygon (see Figures 15 and 16 for location).

Run: /Ramnagar.oxcal

```
Sequence("Ramnagar")
{
 Boundary( );
 Curve("IntCal13","IntCal13.14c");
 Phase("Unit 2")
 {
  R_Date("BR-09", 990, 35);
 };
 Phase("Unit 3")
 {
  R_Date("BR-15", 700, 35);
 };
 Phase("Unit 4")
 {
  R_Date("BR-06", 695, 35);
 };
 Date("Event")
 {
 };
 Phase("Unit 5")
 {
  R_Date("BR-07", 565, 45);
 };
 Boundary( );
};
```

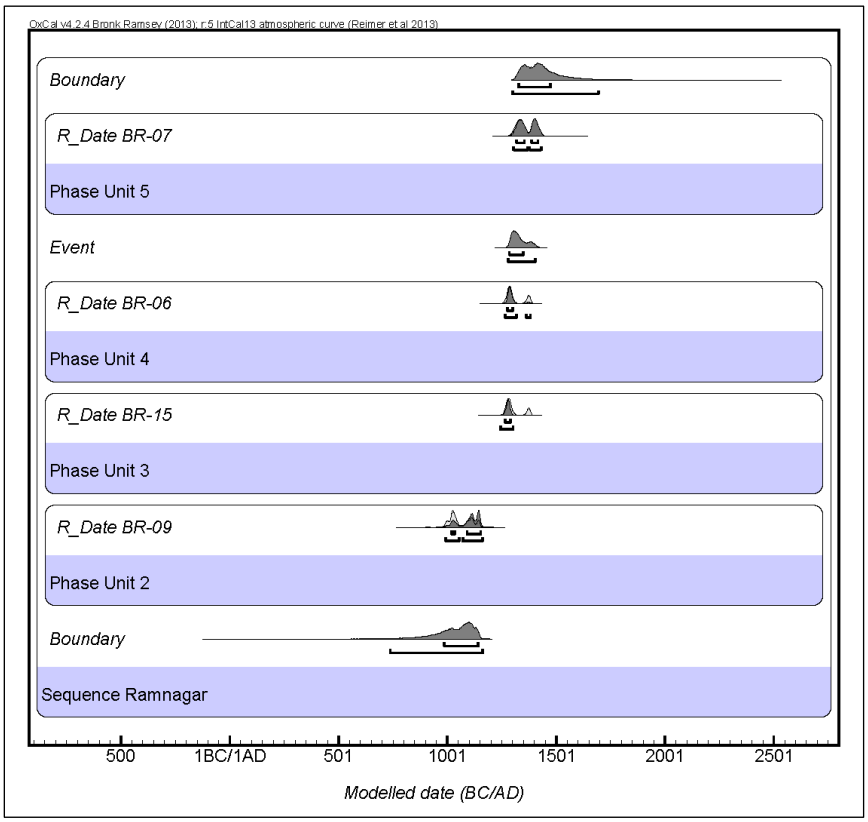
OxCal v4.2.4 Bronk Ramsey (2013); r:5 IntCal13 atmospheric curve (Reimer et al 2013)
Boundary
R_Date BR-07
Phase Unit 5
Event
R_Date BR-06
Phase Unit 4
R_Date BR-15
Phase Unit 3
R_Date BR-09
Phase Unit 2
Boundary
Sequence Ramnagar
500
1BC/1AD
501
1001
1501
2001
2501
Modelled date (BC/AD)

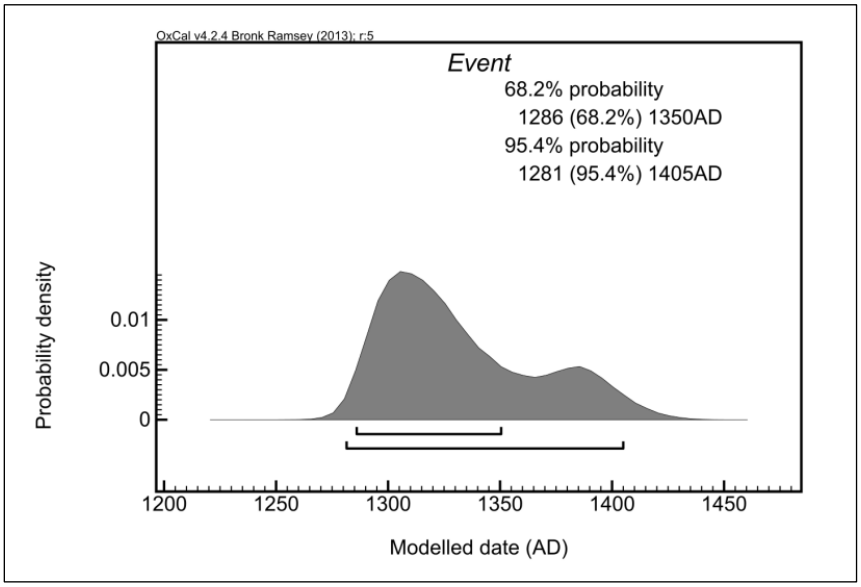
OxCal v4.2.4 Bronk Ramsey (2013); r:5
Event
68.2% probability
1286 (68.2%) 1350AD
95.4% probability
1281 (95.4%) 1405AD
Probability density
0.01
0.005
0
1200
1250
1300
1350
1400
1450
Modelled date (AD)

Ramnagar Trench Site: Rajendran, et al., 2015

Table 2a. Data on Radiocarbon Dates of the Detrital and In Situ Charcoal Fragments From the Trench Site (See Figure 3 for Sample Locations)[a]

Sample ID	^{14}C Age	1 Sigma	2 Sigma
BR-P1 NZA 53311	727 ± 16	[cal A.D. 1271: cal A.D. 1282] 1	[cal A.D. 1264: cal A.D. 1287] 1 Range: A.D. 1265–1290
BR-P2 NZA 53293	1086 ± 17	[cal A.D. 899: cal A.D. 918] 0.386516 [cal A.D. 963: cal A.D. 990] 0.613484	[cal A.D. 895: cal A.D. 925] 0.332924 [cal A.D. 936: cal A.D. 996] 0.645071 [cal A.D. 1004: cal A.D. 1012] 0.022005 Range: A.D. 895–1010
BR-P3 NZA 53291	881 ± 17	[cal A.D. 1157: cal A.D. 1194] 0.794977 [cal A.D. 1195: cal A.D. 1208] 0.205023	[cal A.D. 1051: cal A.D. 1081] 0.165147 [cal A.D. 1126: cal A.D. 1135] 0.02738 [cal A.D. 1152: cal A.D. 1215] 0.807474 Range: A.D. 1050–1215
BR-P4 NZA 53310	884 ± 16	[cal A.D. 1155: cal A.D. 1208] 1	[cal A.D. 1050: cal A.D. 1082] 0.203364 [cal A.D. 1125: cal A.D. 1136] 0.037761 [cal A.D. 1151: cal A.D. 1214] 0.758875 Range: A.D. 1050–1215
BR-P5 NZA 53294	1242 ± 17	[cal A.D. 695: cal A.D. 698] 0.034774 [cal A.D. 708: cal A.D. 747] 0.652714 [cal A.D. 766: cal A.D. 779] 0.23635 [cal A.D. 794: cal A.D. 801] 0.076162	[cal A.D. 687: cal A.D. 755] 0.60006 [cal A.D. 756: cal A.D. 784] 0.207737 [cal A.D. 787: cal A.D. 825] 0.141305 [cal A.D. 840: cal A.D. 862] 0.050898 Range: A.D. 690–860
BR-P6 NZA 53309	849 ± 16	[cal A.D. 1181: cal A.D. 1217] 1	[cal A.D. 1159: cal A.D. 1224] 0.998423 [cal A.D. 1250: cal A.D. 1250] 0.001577 Range: A.D. 1160–1250
BR-P7 NZA 53307	623 ± 16	[cal A.D. 1300: cal A.D. 1319] 0.43464 [cal A.D. 1351: cal A.D. 1368] 0.385174 [cal A.D. 1381: cal A.D. 1390] 0.180186	[cal A.D. 1294: cal A.D. 1326] 0.393414 [cal A.D. 1343: cal A.D. 1394] 0.606586 Range: 1295–1395
BR-P7-A NZA 53303	634 ± 16	[cal A.D. 1297: cal A.D. 1312] 0.372608 [cal A.D. 1358: cal A.D. 1373] 0.36546 [cal A.D. 1377: cal A.D. 1387] 0.261933	[cal A.D. 1291: cal A.D. 1321] 0.396338 [cal A.D. 1348: cal A.D. 1392] 0.603662 Range: 1290–1390
BR-P8 NZA 53302	692 ± 16	[cal A.D. 1280: cal A.D. 1292] 1	[cal A.D. 1274: cal A.D. 1299] 0.916264 [cal A.D. 1370: cal A.D. 1380] 0.083736 Range: 1275–1380

[a]AMS dating of charcoal samples were conducted at Rafter Radiocarbon Laboratory (New Zealand). Radiocarbon ages were calibrated using CALIB (version 6.1.1) [*Stuiver and Reimer*, 1993]. Terrestrial samples were calibrated using the intcal09 data set. [*Reimer et al.*, 2009]. The 2 sigma ranges have maximum area under the probability distribution curve. Ages are rounded off to the nearest decade. Sample P8 is an in situ charcoal, and the rest are detrital. Charcoal dates from a previous adjacent trench [*Kumar et al.*, 2006] identified by suffix "K1 to K4" in Figure 3b are not listed here. Age ranges are rounded off.

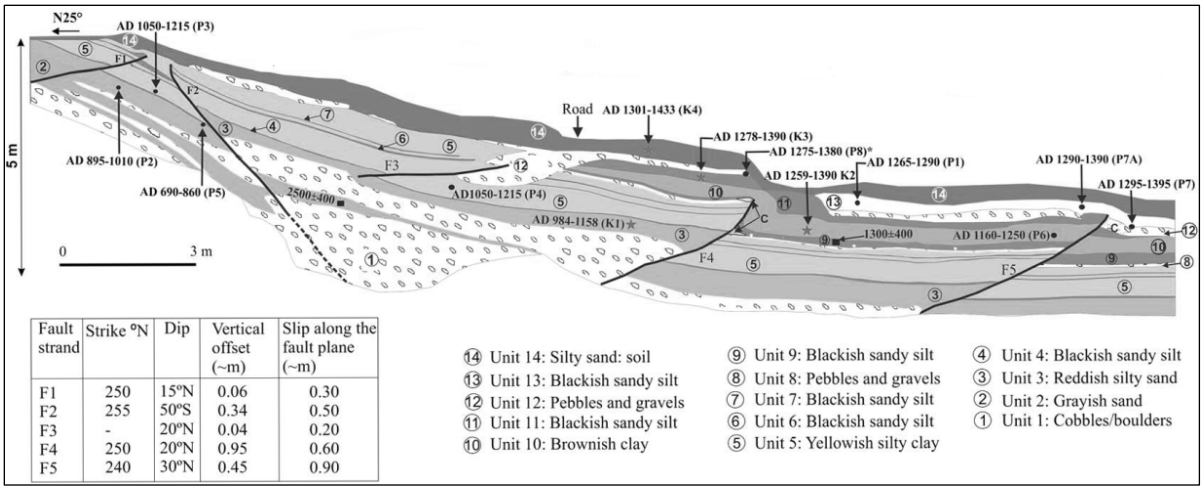

Fault strand	Strike °N	Dip	Vertical offset (~m)	Slip along the fault plane (~m)
F1	250	15°N	0.06	0.30
F2	255	50°S	0.34	0.50
F3	-	20°N	0.04	0.20
F4	250	20°N	0.95	0.60
F5	240	30°N	0.45	0.90

Figure3. (a) Profile of the scarp at Belparao near Ramnagar. (b) Full view of the trench section (eastern wall) showing sedimentary units (numbers within circles; see Table1 for more details),fault strands, colluvial wedges (C) ages and locations of charcoal (filled circles: present study; stars: previous study), and OSL samples (filled rectangles). All charcoal samples are detrital except the starred sample P8(A.D.1275–1390). See Figures 4–6 for closer views of logs and photographs of various segments of the trench section. Offset measurements on the fault strands are shown in a table.

Run: /Ramnagar_Rajendran.oxcal

```
Sequence("Ramnagar - Rajendran / Kumar")
{
 Boundary();
 Phase("Unit 3")
 {
  R_Date("P5", 1242, 17);
  R_Date("P2", 1086, 17);
 };
 Phase("Unit 5")
 {
  R_Date("P4", 884, 16);
  R_Date("P3", 881, 17);
 };
 Phase("Unit 10")
 {
  R_Date("P6", 849, 16);
 };
 Phase("Unit 11")
 {
  R_Date("P8", 692, 16);
 };
 Date("Event");
 Phase("Unit 13")
 {
  R_Date("P7a", 634, 16);
  R_Date("P7", 623, 16);
 };
 Boundary();
};
```

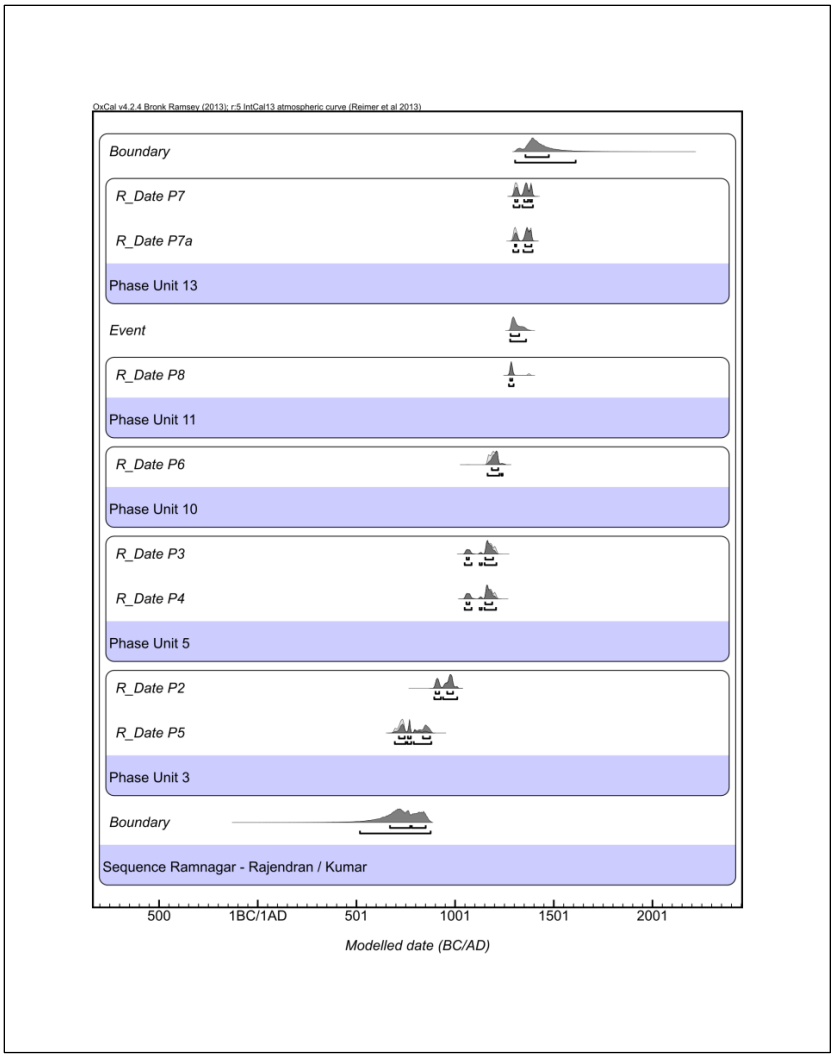
OxCal v4.2.4 Bronk Ramsey (2013); r:5 IntCal13 atmospheric curve (Reimer et al 2013)
Boundary
R_Date P7
R_Date P7a
Phase Unit 13
Event
R_Date P8
Phase Unit 11
R_Date P6
Phase Unit 10
R_Date P3
R_Date P4
Phase Unit 5
R_Date P2
R_Date P5
Phase Unit 3
Boundary
Sequence Ramnagar - Rajendran / Kumar
500
1BC/1AD
501
1001
1501
2001
Modelled date (BC/AD)

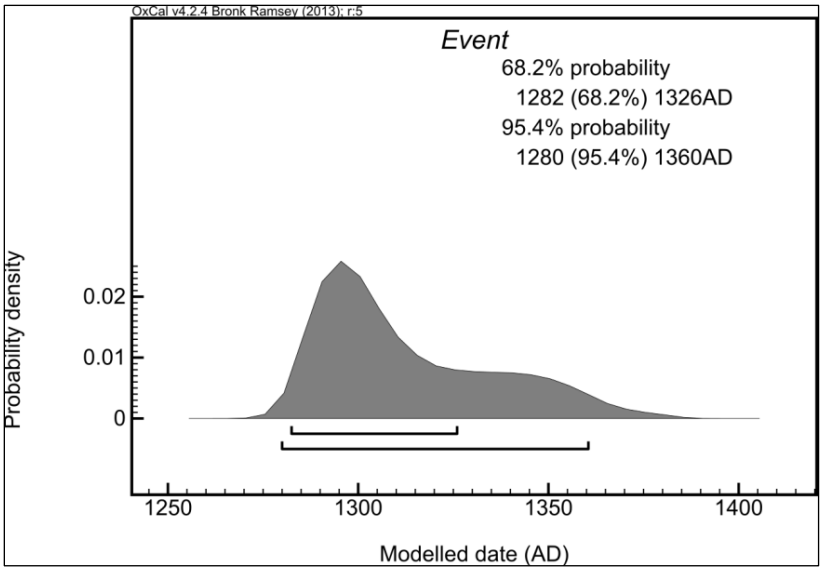
OxCal v4.2.4 Bronk Ramsey (2013); r:5
Event
68.2% probability
1282 (68.2%) 1326AD
95.4% probability
1280 (95.4%) 1360AD
Probability density
0.02
0.01
0
1250
1300
1350
1400
Modelled date (AD)

APPENDIX B

SUPPLEMENTARY MATERIALS – CHAPTER 3

Strat. Unit	Sample ID	Lab ID	Radiocarbon Age (BP)	Margin of Error (+/-)	Calibrated/Modeled Calendar Age (2σ)
3	LDT1S-C23	D-AMS 016004	818	47	1192-1273 CE
3	LDT1S-C01	D-AMS 015998	760	41	1212-1275 CE
4	LDT1-C38	D-AMS 015994	786	25	1236-1281 CE
6a	LDT1S-C19	D-AMS 016003	654	25	1277-1325 CE, 1350-1366 CE
6a	LDT1-C39	D-AMS 015995	578	23	1300-1351 CE
6b	LDT1S-C11	D-AMS 015999	615	27	1305-1377 CE
7a	LDT1S-C13	D-AMS 016000	605	30	1339-1414 CE
7a	LDT1N-C08	Poz-77708	630	30	1346-1407 CE
7a	LDT1N-C07	Poz-77707	465	30	1412-1453 CE
7b	LDT1S-C14	D-AMS 016001	696	20	Not included in model OxCal AI = 17.4
8	LDT1S-C16	D-AMS 016002	420	39	1430-1492 CE
8	LDT1N-C10	Poz-77709	350	30	1442-1518 CE
9a	LDT1S-C18	CAMS 180268	405	30	1452-1524 CE, 1575-1584 CE 1590-1620 CE
Contact 2/3 (Pit)	LDP1-C03	CAMS 179134	980	35	993-1155 CE
6 (Pit)	LDP1-C08	CAMS 179609 CAMS 179612	610 630	30 30	1294-1398 CE (Combined)

Radiocarbon Data: Charcoal samples collected from a paleoseismic trench at Lal Dhang, Uttarakhand, India. Samples LDP1-C03 and LDP1-C08 were collected from a test pit at the top of the fault scarp. Sample LDT1S-C14 was not included in the final OxCal model due to a low Agreement Index (AI) of 17.4. D-AMS = Direct AMS,USA; Poz = Poznan Radiocarbon Laboratory, Poland; CAMS = Center for Accelerator Mass Spectrometry at Lawrence Livermore National Laboratory, USA.

Name Show all Show structure		Unmodelled (BCE/CE)			Modelled (BCE/CE)			Indices A_{model}=8.3 $A_{overall}$=9.2					Select All Visible	Page break
		from	to	%	from	to	%	A_{comb}	A	L	P	C		
					Warning! Poor agreement - A= 9.2%(A'c= 60.0%) Warning! Poor agreement - A= 8.3%(A'c= 60.0%)									
Boundary END					1452	1739	95.4					97.3	27	
R_Date LDT1S-C18		1439	1619	95.4	1451	1620	95.4		71.6			98.4	26	
Phase UNIT 9													25	
Boundary EVENT 2					1446	1570	95.4					99.3	24	
R_Date LDT1N-C10		1458	1635	95.4	1441	1516	95.4		65.7			99.6	23	
R_Date LDT1S-C16		1420	1628	95.4	1420	1490	95.4		129.3			99.6	22	
Phase UNIT 8													21	
R_Date LDT1S-C14		1270	1382	95.4	1365	1386	95.4		17.4			99.9	20	
					Warning! Poor agreement - A= 17.4%(A'c= 60.0%)									
Phase Unit 7B													19	
R_Date LDT1N-C07		1410	1465	95.4	1324	1351	95.4		0.3			99.7	18	
					Warning! Poor agreement - A= 0.3%(A'c= 60.0%)									
R_Date LDT1N-C08		1287	1399	95.4	1320	1380	95.4		98.8			99.9	17	
R_Date LDT1S-C13		1297	1406	95.4	1320	1375	95.4		105.2			99.9	16	
Phase UNIT 7A													15	
Boundary EVENT 1					1307	1344	95.4					99.7	14	
R_Date LDT1S-C11		1295	1400	95.4	1301	1337	95.4		107.3			99.7	13	
Phase UNIT 6B													12	
R_Date LDT1-C39		1306	1415	95.4	1295	1330	95.4		49.6			99.7	11	
					Warning! Poor agreement - A= 49.6%(A'c= 60.0%)									
R_Date LDT1S-C19		1281	1392	95.4	1281	1318	95.4		99.5			99.8	10	
Phase UNIT 6A													9	
R_Date LDT1-C38		1215	1276	95.4	1239	1281	95.4		90.9			99.7	8	
Phase UNIT 4													7	
R_Date LDT1S-C01		1188	1295	95.4	1215	1275	95.4		105.8			99.4	6	
R_Date LDT1S-C23		1050	1280	95.4	1199	1275	95.4		119.5			99.4	5	
Phase UNIT 3													4	
Boundary START					1160	1268	95.4					96.6	3	
Sequence LAL DHANG													2	

Tabulated Results of OxCal Model: Initial (prior to removal of sample LDT1S-C14)

Name Show all Show structure		Unmodelled (BCE/CE)			Modelled (BCE/CE)			Indices A_{model}=79.3 $A_{overall}$=85.1					Select All Visible	Page break
		from	to	%	from	to	%	A_{comb}	A	L	P	C		
Boundary END					1453	1746	95.4					98.5	25	
R_Date LDT1S-C18		1439	1619	95.4	1452	1620	95.4		69.6			99.6	24	
Phase UNIT 9													23	
Boundary EVENT 2					1447	1572	95.4					99.7	22	
R_Date LDT1N-C10		1458	1635	95.4	1442	1518	95.4		67.3			99.9	21	
R_Date LDT1S-C16		1420	1628	95.4	1430	1492	95.4		137.6			99.9	20	
Phase UNIT 8													19	
R_Date LDT1N-C07		1410	1465	95.4	1412	1453	95.4		103.4			99.9	18	
R_Date LDT1N-C08		1287	1399	95.4	1346	1407	95.4		99.3			99.8	17	
R_Date LDT1S-C13		1297	1406	95.4	1339	1414	95.4		91.1			99.9	16	
Phase UNIT 7A													15	
Boundary EVENT 1					1317	1391	95.4					99.6	14	
R_Date LDT1S-C11		1295	1400	95.4	1305	1377	95.4		99.9			99.8	13	
Phase UNIT 6B													12	
R_Date LDT1-C39		1306	1415	95.4	1300	1351	95.4		88.3			99.9	11	
R_Date LDT1S-C19		1281	1392	95.4	1277	1366	95.4		94			99.9	10	
Phase UNIT 6A													9	
R_Date LDT1-C38		1215	1276	95.4	1236	1281	95.4		93.6			99.7	8	
Phase UNIT 4													7	
R_Date LDT1S-C01		1188	1295	95.4	1212	1275	95.4		101.1			99.4	6	
R_Date LDT1S-C23		1050	1280	95.4	1192	1273	95.4		121			99.4	5	
Phase UNIT 3													4	
Boundary START					1142	1266	95.4					97	3	
Sequence LAL DHANG													2	

Tabulated Results of OxCal Model: Final.

Modeled OxCal results for individual radiocarbon samples, events, and sequence boundaries:

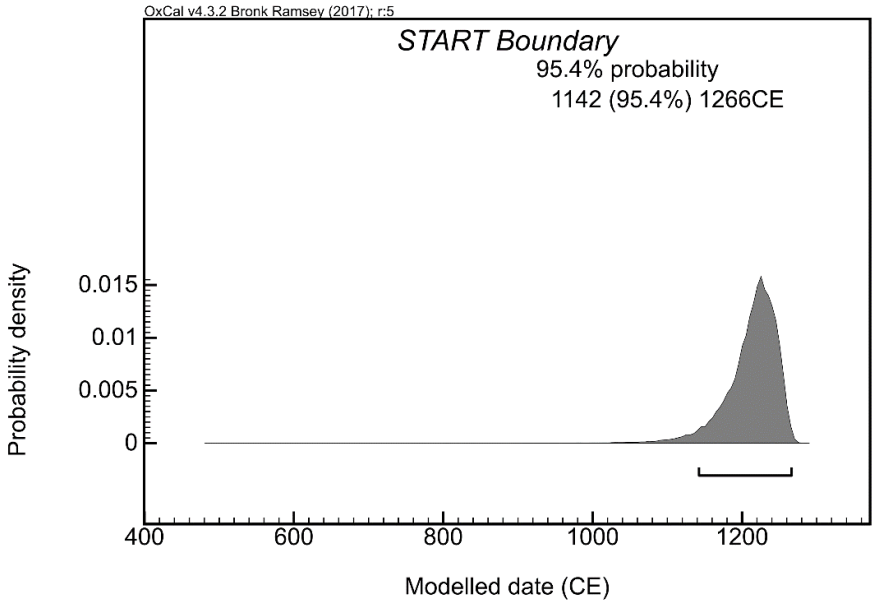

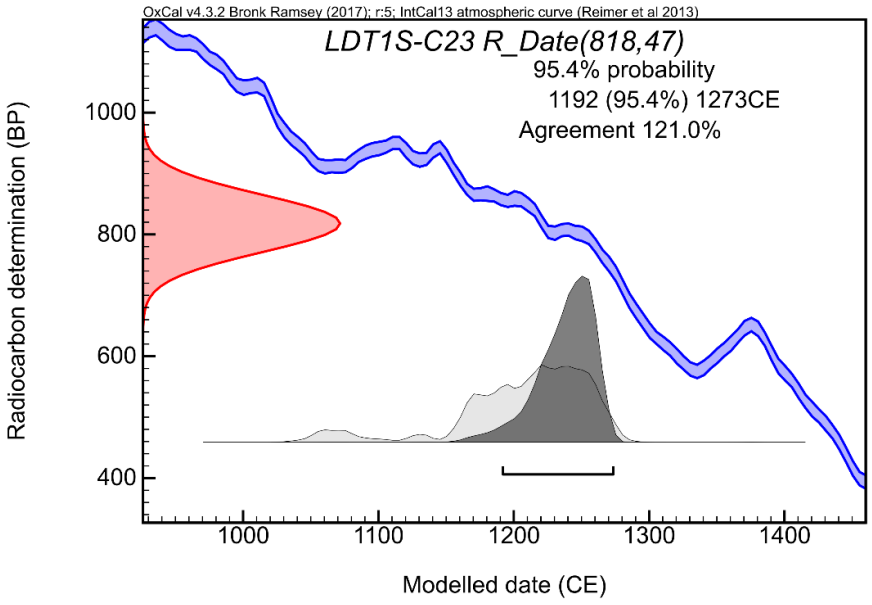

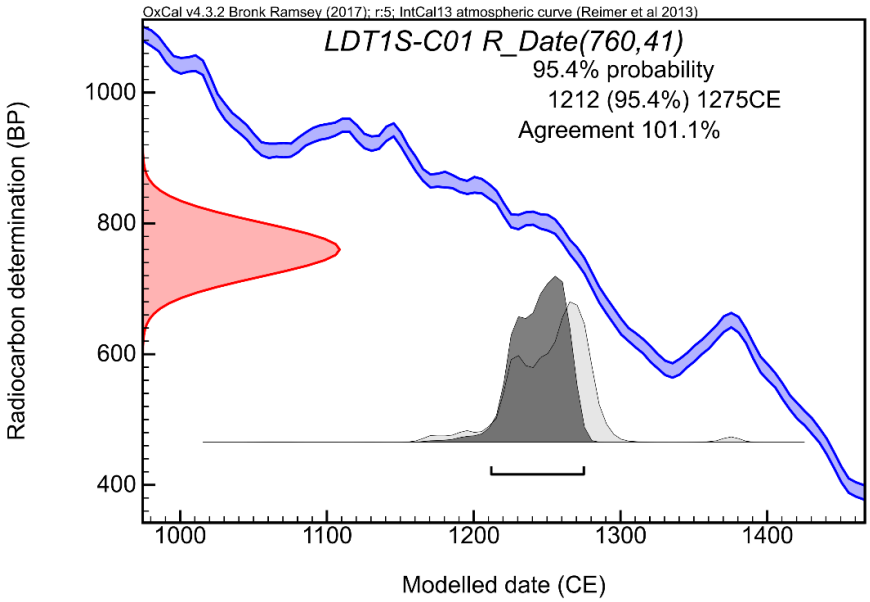
OxCal v4.3.2 Bronk Ramsey (2017); r:5; IntCal13 atmospheric curve (Reimer et al 2013)
LDT1S-C01 R_Date(760,41)
95.4% probability
1212 (95.4%) 1275CE
Agreement 101.1%
Radiocarbon determination (BP)
1000
800
600
400
1000
1100
1200
1300
1400
Modelled date (CE)

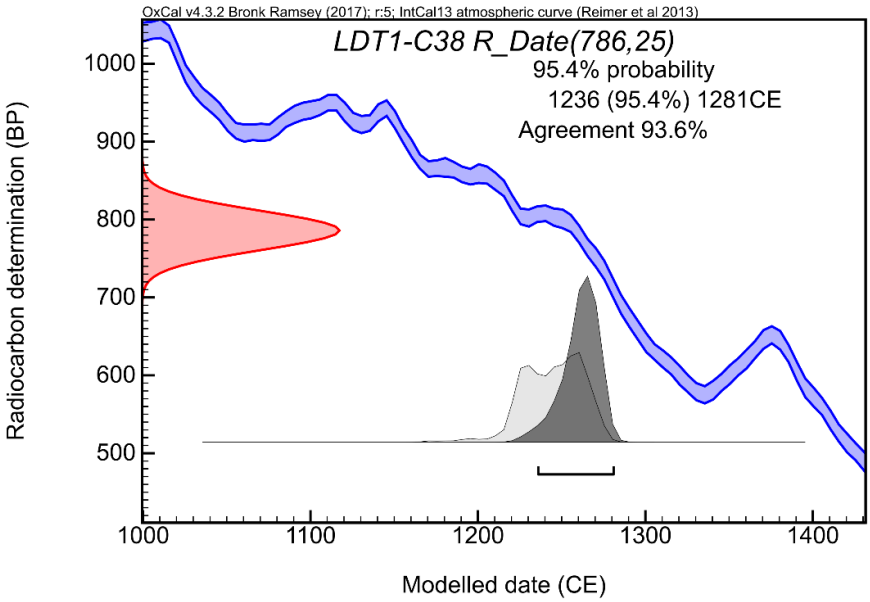
OxCal v4.3.2 Bronk Ramsey (2017); r:5; IntCal13 atmospheric curve (Reimer et al 2013)
LDT1-C38 R_Date(786,25)
95.4% probability
1236 (95.4%) 1281CE
Agreement 93.6%
Radiocarbon determination (BP)
1000
900
800
700
600
500
1000
1100
1200
1300
1400
Modelled date (CE)

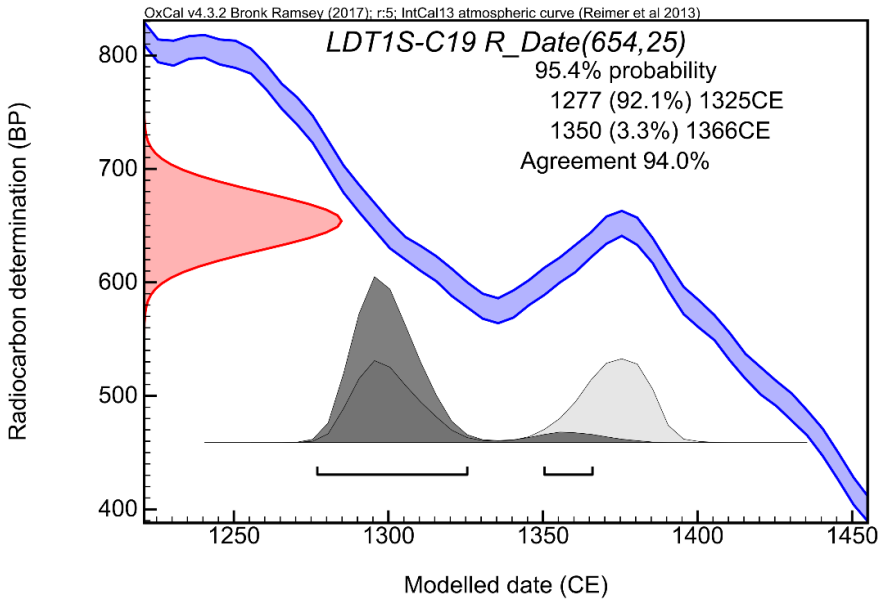
OxCal v4.3.2 Bronk Ramsey (2017); r:5; IntCal13 atmospheric curve (Reimer et al 2013)
LDT1S-C19 R_Date(654,25)
95.4% probability
1277 (92.1%) 1325CE
1350 (3.3%) 1366CE
Agreement 94.0%
Radiocarbon determination (BP)
800
700
600
500
400
1250
1300
1350
1400
1450
Modelled date (CE)

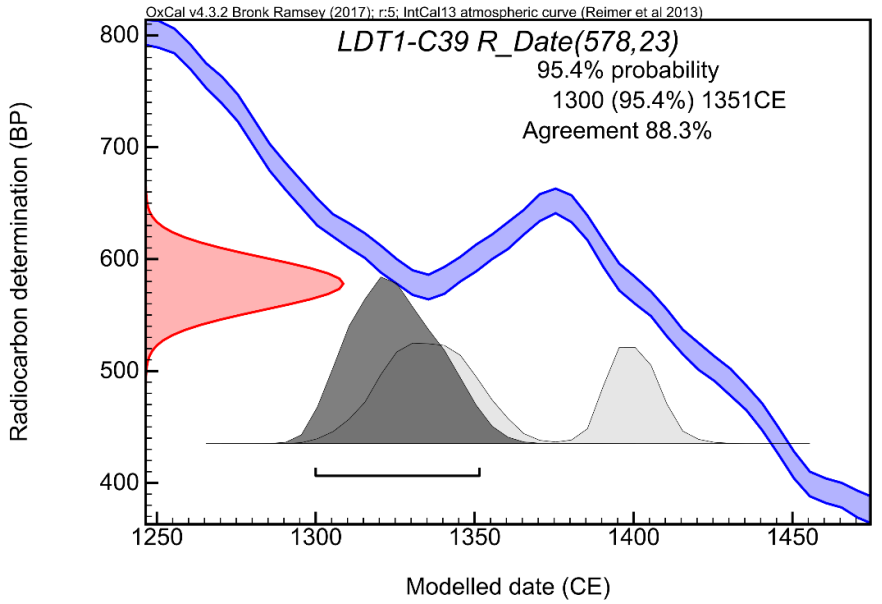
OxCal v4.3.2 Bronk Ramsey (2017); r:5; IntCal13 atmospheric curve (Reimer et al 2013)
LDT1-C39 R_Date(578,23)
95.4% probability
1300 (95.4%) 1351CE
Agreement 88.3%
Radiocarbon determination (BP)
800
700
600
500
400
1250
1300
1350
1400
1450
Modelled date (CE)

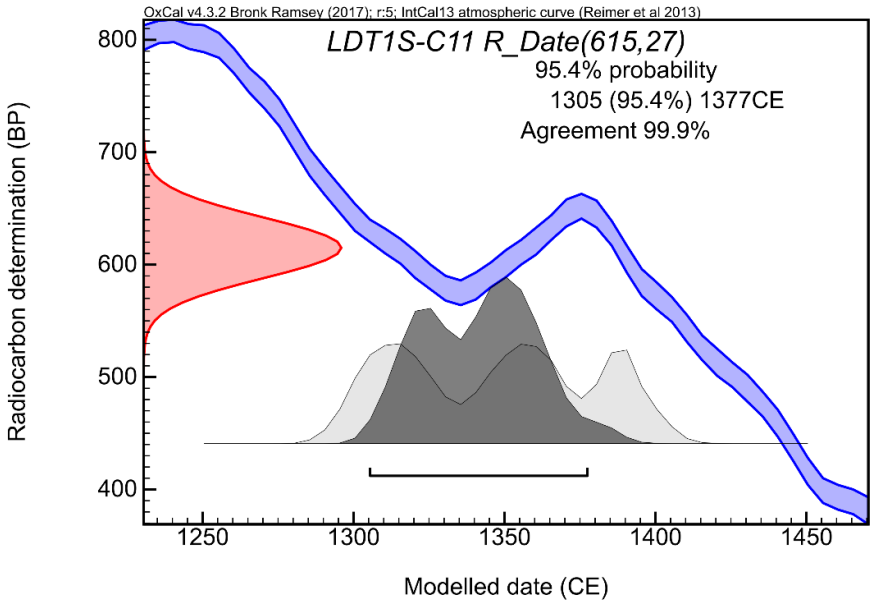
OxCal v4.3.2 Bronk Ramsey (2017); r:5; IntCal13 atmospheric curve (Reimer et al 2013)
LDT1S-C11 R_Date(615,27)
95.4% probability
1305 (95.4%) 1377CE
Agreement 99.9%
Radiocarbon determination (BP)
800
700
600
500
400
1250
1300
1350
1400
1450
Modelled date (CE)

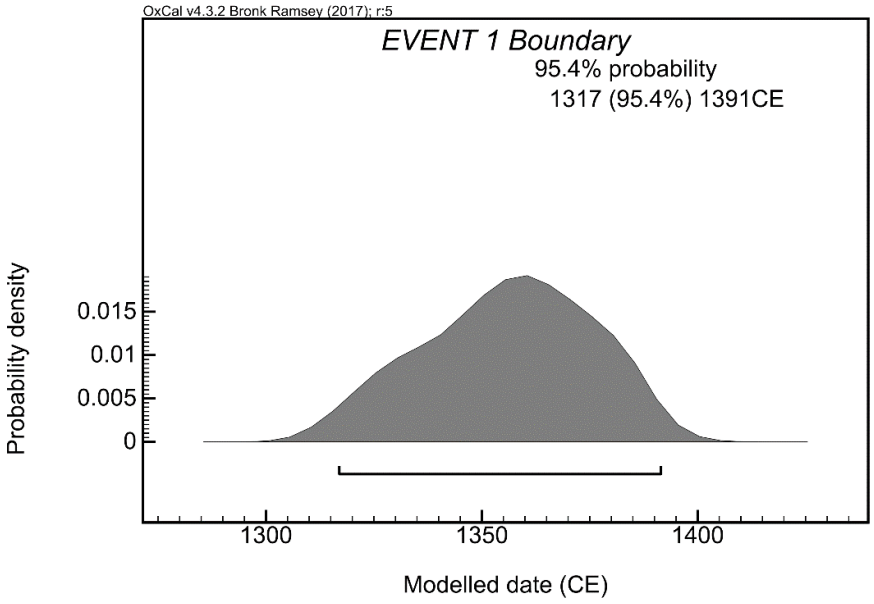
OxCal v4.3.2 Bronk Ramsey (2017); r:5
EVENT 1 Boundary
95.4% probability
1317 (95.4%) 1391CE
Probability density
0.015
0.01
0.005
0
1300
1350
1400
Modelled date (CE)

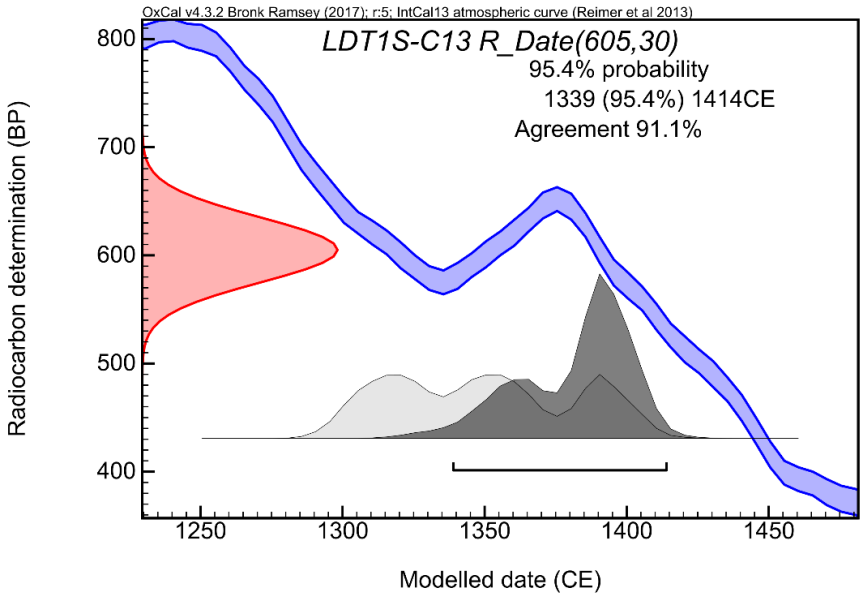
OxCal v4.3.2 Bronk Ramsey (2017); r:5; IntCal13 atmospheric curve (Reimer et al 2013)
LDT1S-C13 R_Date(605,30)
95.4% probability
1339 (95.4%) 1414CE
Agreement 91.1%
Radiocarbon determination (BP)
800
700
600
500
400
1250
1300
1350
1400
1450
Modelled date (CE)

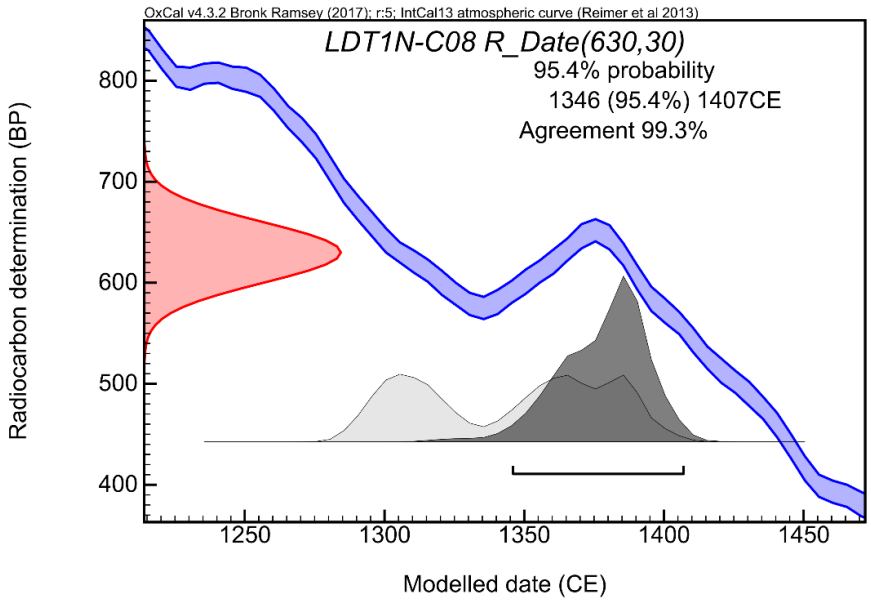
OxCal v4.3.2 Bronk Ramsey (2017); r:5; IntCal13 atmospheric curve (Reimer et al 2013)
LDT1N-C08 R_Date(630,30)
95.4% probability
1346 (95.4%) 1407CE
Agreement 99.3%
Radiocarbon determination (BP)
800
700
600
500
400
1250
1300
1350
1400
1450
Modelled date (CE)

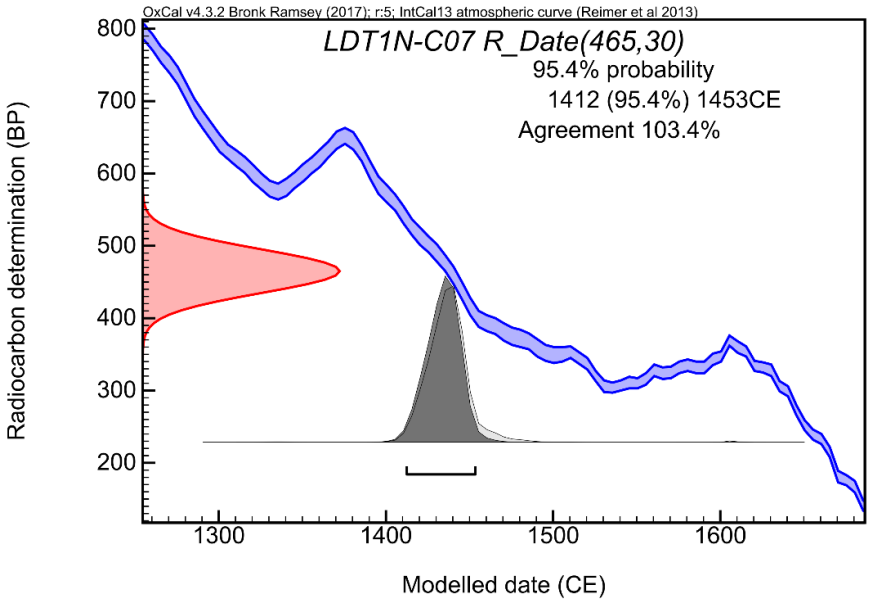
OxCal v4.3.2 Bronk Ramsey (2017); r:5; IntCal13 atmospheric curve (Reimer et al 2013)
LDT1N-C07 R_Date(465,30)
95.4% probability
1412 (95.4%) 1453CE
Agreement 103.4%
Radiocarbon determination (BP)
800
700
600
500
400
300
200
1300
1400
1500
1600
Modelled date (CE)

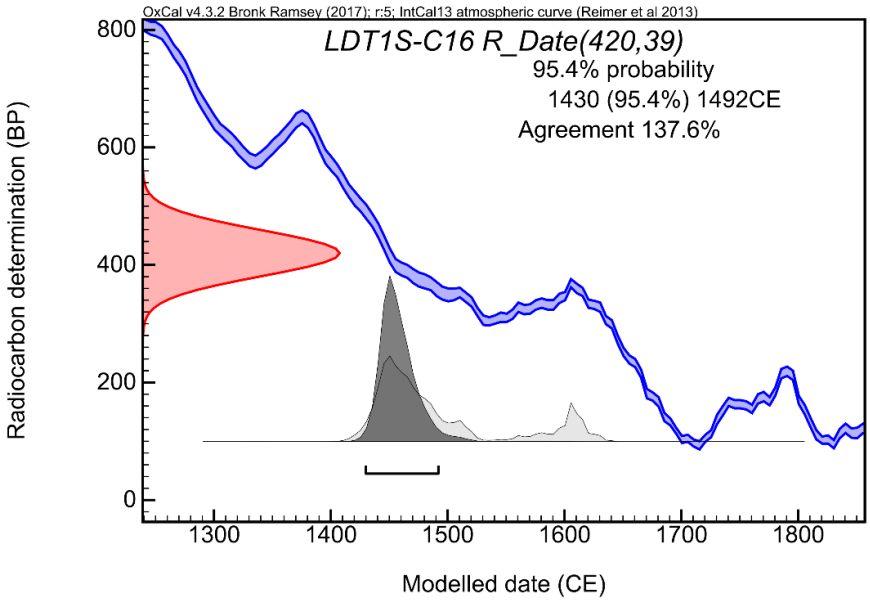
OxCal v4.3.2 Bronk Ramsey (2017); r:5; IntCal13 atmospheric curve (Reimer et al 2013)
LDT1S-C16 R_Date(420,39)
95.4% probability
1430 (95.4%) 1492CE
Agreement 137.6%
Radiocarbon determination (BP)
800
600
400
200
0
1300
1400
1500
1600
1700
1800
Modelled date (CE)

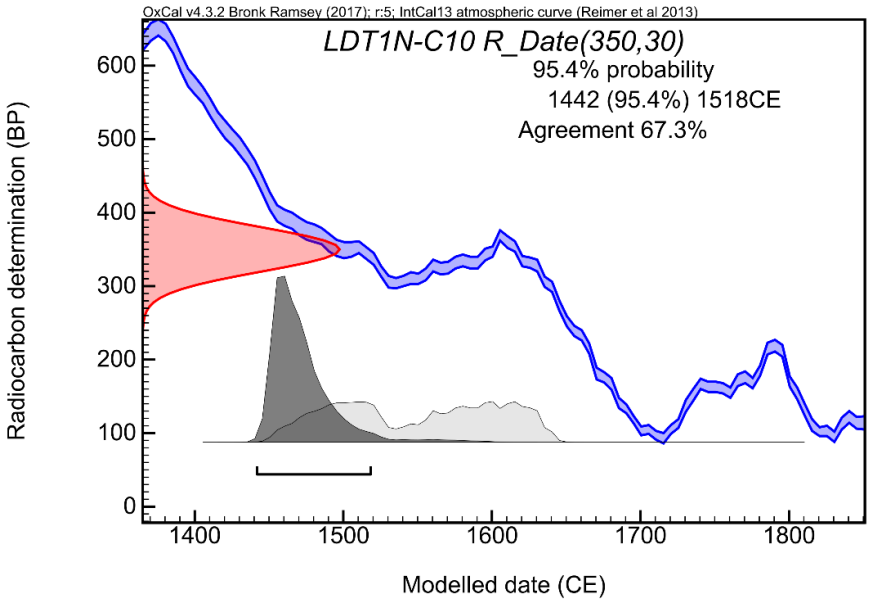
OxCal v4.3.2 Bronk Ramsey (2017); r:5; IntCal13 atmospheric curve (Reimer et al 2013)
LDT1N-C10 R_Date(350,30)
95.4% probability
1442 (95.4%) 1518CE
Agreement 67.3%
Radiocarbon determination (BP)
600
500
400
300
200
100
0
1400
1500
1600
1700
1800
Modelled date (CE)

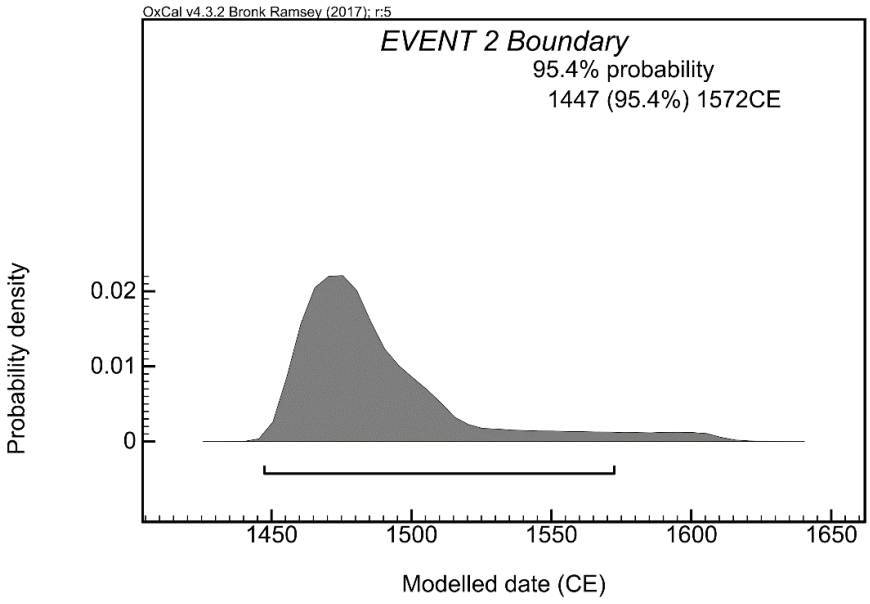
OxCal v4.3.2 Bronk Ramsey (2017); r:5
EVENT 2 Boundary
95.4% probability
1447 (95.4%) 1572CE
Probability density
0.02
0.01
0
1450
1500
1550
1600
1650
Modelled date (CE)

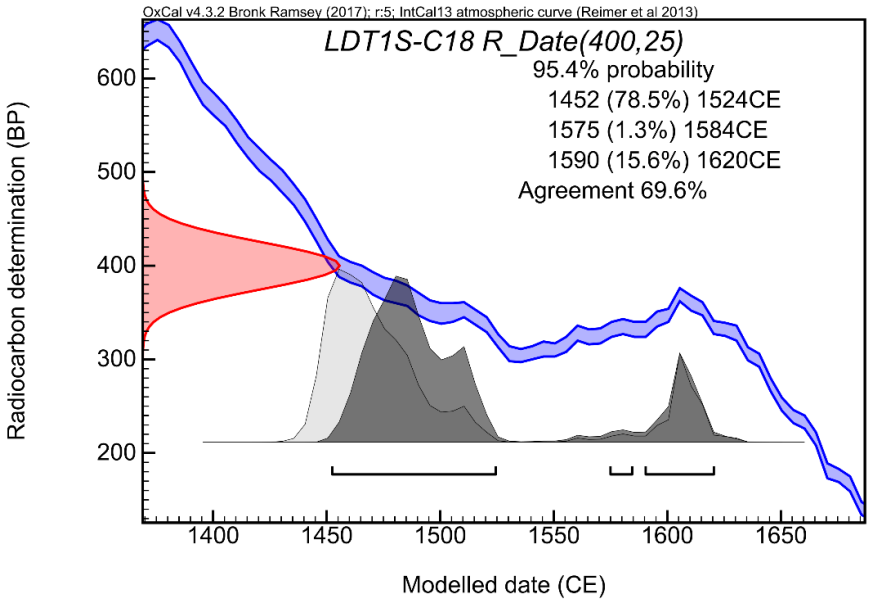
OxCal v4.3.2 Bronk Ramsey (2017); r:5; IntCal13 atmospheric curve (Reimer et al 2013)
LDT1S-C18 R_Date(400,25)
95.4% probability
1452 (78.5%) 1524CE
1575 (1.3%) 1584CE
1590 (15.6%) 1620CE
Agreement 69.6%
Radiocarbon determination (BP)
600
500
400
300
200
1400
1450
1500
1550
1600
1650
Modelled date (CE)

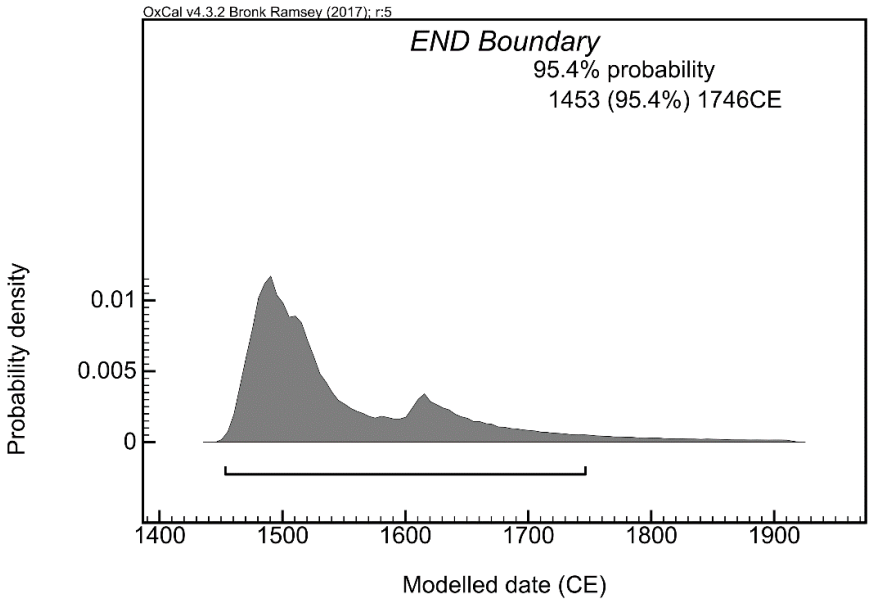
OxCal v4.3.2 Bronk Ramsey (2017); r:5
END Boundary
95.4% probability
1453 (95.4%) 1746CE
Probability density
0.01
0.005
0
1400
1500
1600
1700
1800
1900
Modelled date (CE)

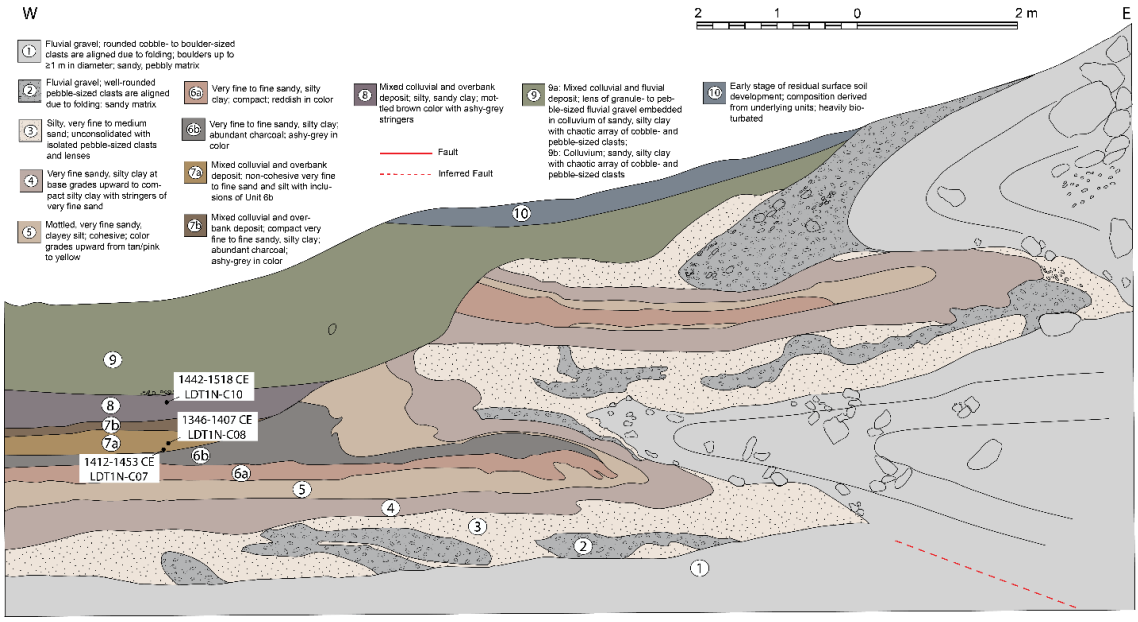

Trench log depicting the north wall of the paleoseismic trench at Lal Dhang, Uttarakhand, India. Sample collection locations for samples LDT1N-C07, LDT1N-C08 and LDT1N-C10 are shown. Units are the same as those defined in the south wall trench log legend (Fig. 3).

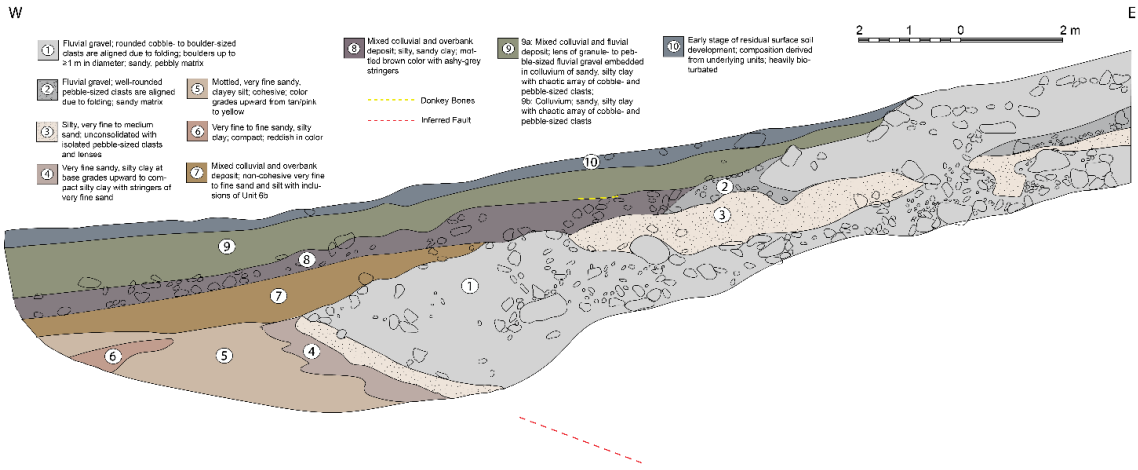

Trench log depicting north wall of a second paleoseismic trench at Lal Dhang, Uttarakhand, India. Evidence supports findings from initial trench (above and Fig. 3). Thrust fault tip lies below and behind the lowermost fold, outside of the area of the trench log. Deformational sequence is incomplete due to heavy erosion and anthropogenic disturbance of the stratigraphy. Logistical limitations prevented further excavation. Dashed red line marks location of a horse burial. Units are not labeled, as correlation with units in the initial trench were not confirmed through radiocarbon analysis.

REFERENCES

Ader, T., Avouac, J., Liu-Zeng, J., Lyon-Caen, H., Bollinger, L., Galetzka, J,…Flouzat, M. (2012). Convergence rate across the Nepal Himalaya and interseismic coupling on the Main Himalayan Thrust: Implications for seismic hazard. *Journal of Geophysical Research, 117*, B04403. doi:10.1029/2011JB009071.

Agard, P., Omrani, J., Jolivet, L., & Mouthereau, F. (2005). Convergence history across Zagros (Iran), constraints from collisional and earlier deformation. *International Journal of Earth Sciences, 94*, 401–419.

Ambraseys, N. (2000). Reappraisal of north-India earthquakes at the turn of the 20th century. *Current Science, 70*, 1237-1250.

Ambraseys, N., & Bilham, R. (2003). Reevaluated intensities for the Great Assam Earthquake of 12 June 1897, Shillong, India. *Bulletin of the Seismological Society of America, 93*(2), 655-673.

Ambraseys, N., & Jackson, D. (2003). A note on early earthquakes in northern India and southern Tibet. *Current Science, 84*(4), 570-582.

Ambraseys, N., & Douglas, J. (2004). Magnitude calibration of north Indian earthquakes. *Geophysical Journal International, 159*, 165-206. http://doi.org/10.1111/j.1365-246X.2004.02323.x.

Ando, M. (1975). Source mechanisms and tectonic significance of historical earthquakes along the Nankai trough, Japan. *Tectonophysics*, *27*(2), 119-140. https://doi.org/10.1016/0040-1951(75)90102-X.

Banerjee, P., & Bürgmann, R. (2002). Convergence across the northwest Himalaya from GPS measurements. *Geophysical Research Letters, 29*(13), 30 1-4. http://dx.doi.org/10.1029/2002GL015184.

Bayes, T. R. (1763). An essay towards solving a problem in the doctrine of chances. *Philosophical Transactions of the Royal Society, 53*, 370-418.

Bettinelli, P., Avouac, J. P., Flouzat, M., Jouanne, F., Bollinger, L., Willis, P., & Chitrakar, G. R. (2006). Plate motion of India and interseismic strain in the Nepal Himalaya from GPS an DORIS measurements. *Journal of Geodesy, 80*, 567-589. http://dx.doi.org/10.1007/s00190-006-0030-3.

Bilek, S. L. (2007). Influence of subducting topography on earthquake rupture. In: Dixon, T.H., Moore, J.C., (Eds.), *The Seismogenic Zone of Subduction Thrust Faults* (123-146). New York, NY: Columbia University Press.

Bilham, R., Larson, K., Freymueller, J., & Project Idylhim members. (1997). GPS measurements of present-day convergence across the Nepal Himalaya. *Nature, 386*(6), 61-64.

Bilham, R. (2004). Earthquakes in India and the Himalaya: tectonics, geodesy and history. *Annals of Geophysics, 47*(2/3), 839-858.

Bilham, R., & Ambraseys, N. (2005). Apparent Himalayan slip deficit from the summation of seismic moments for Himalayan earthquakes, 1500-2000. *Current Science, 88*(10), 1658-1663.

Bilham, R. (2019). Himalayan earthquakes: a review of historical seismicity and early 21st century slip potential. *Geological Society of London*, *483*(1), 423-482. https://doi.org/10.1144/sp483.16.

Bollinger, L., Sapkota, S. N., Tapponnier, P., Klinger, Y., Rizza, M., Van der Woerd, J,…Bes de Berc, S. (2014). Estimating the return times of great Himalayan earthquakes in eastern Nepal: Evidence from the Patu and Bardibas strand of the Main Frontal Thrust. *Journal of Geophysical Research, 119*, 7123–7163.

Bollinger, L., Tapponnier, P., Sapkota, S. N., & Klinger, Y. (2016). Slip deficit in central Nepal: omen for a repeat of the 1344 AD earthquake? *Earth, Planets and Space, 68*(12), doi:10.1186/s40623-016-0389-1

Bronk Ramsey, C. (2009a). Bayesian analysis of radiocarbon dates. *Radiocarbon, 51*(1), 337-360.

Bronk Ramsey, C. (2009b). Dealing with outliers and offsets in radiocarbon dating. *Radiocarbon, 51*(3), 1023-1045.

Castellarin, A., & Cantelli, L. (2000). Neo-Alpine evolution of the Southern Eastern Alps. *Journal of Geodynamics, 30*, 251–274.

Cèlèrier, J., Harrison, T. M., Webb, A., & Yin, A. (2009). The Kumaun and Garhwal Lesser Himalaya, India: Part 1. Structure and stratigraphy. *GSA Bulletin, 121* (9/10), 1262-1280. http://dx.doi.org/10.1130/B26344.1.

Dasgupta, S., & Mukhopadhyay, B. (2014). 1803 earthquake in Garhwal Himalaya-archival materials with commentary. *Indian Journal of History of Science, 49*(1), 21-33.

Dingle, E. H., Sinclair, H., Attal, M., Milodowski, D., & Singh, V. (2016). Subsidence control on river morphology and grain size in the Ganga Plain. *American Journal of Science*, 316, 778–812. https://doi.org/10.2475/08.2016.03.

Feldl, N., & Bilham, R. (2006). Great Himalyan earthquakes and the Tibetan plateau. *Nature, 444*, 165-170, doi:10.1038/nature05199

Gupta, H. K., & Gahalaut, V. K. (2015). Can an earthquake of M_w~9 occur in the Himalayan region? In: Mukherjee, S., Carosi, R., Van der Beek, P. A., Mukherjee, B. K., Robinson, D. M. (Eds.), Tectonics of Himalaya. *Geological Society, London, Special Publications, 412*, 43-53. http://dx.doi.org/10.1144/SP412.10.

Iyengar, R. N., Sharma, D., & Siddiqui, J. M. (1999). Earthquake history of India in Medieval times. *Indian Journal of History of Science, 34*(3), 181-237.

Jackson, D. (2002). The great western-Himalayan earthquake of 1505: A rupture of the Central Himalayan Gap? In: H. Blezer, A. McKay, C. Ramble (Eds.), *Brill's Tibetan Studies Library, 2/1* (147-159). Leiden, The Netherlands: Koninklijke Brill NV.

Jayangondaperumal, R., Mugnier, J. L., & Dubey, A. K. (2013). Earthquake slip estimation from the scarp geometry of Himalayan Frontal Thrust, western Himalaya: Implications for seismic hazard assessment. *International Journal of Earth Sciences, 102*, 1937–1955. http://dx.doi.org/10.1007/s00531-013-0888-2

Jayangondaperumal, R., Kumahara, Y., Thakur, V. C., Kumar, A., Srivastava, P., Shubhanshu, D.,…Dubey, A. K., (2017a). Great earthquake surface ruptures along backthrust of the Janauri anticline, NW Himalaya. *Journal of Asian Earth Sciences, 133*, 89-101.

Jayangondaperumal, R., Daniels, R. L., & Niemi, T. M. (2017b). A paleoseismic age model for large-magnitude earthquakes on fault segments of the Himalayan Frontal Thrust in the Central Seismic Gap of northern India. *Quaternary International, 462*, 130-137. http://dx.doi.org/10.1016/j.quaint.2017.04.008.

Jayangondaperumal, R., Thakur, V. C., Joevivek, V., Rao, P. S., & Gupta, A. K. (2018). *Active Tectonics of Kumaun and Garhwal Himalaya.* Singapore: Springer Natural Hazards.

Khattri, K. N., & Tyagi, A. K. (1983). The transverse tectonic features in the Himalaya. *Tectonophysics, 96*, 19-29.

Khattri, K. N. (1987). Great earthquakes, seismicity gaps and potential for earthquake disaster along the Himalaya plate boundary. *Tectonophysics, 138*, 79-92.

Konca, A. O., Avouac, J. P., Sladen, A., Meltzner, A. J., Sieh, K., Fang, P.,…Helmberger, D. V. (2008). Partial rupture of a locked patch of the Sumatra megathrust during the 2007 earthquake sequence. *Nature*, *456*(7222), 631–635. https://doi.org/10.1038/nature07572.

Kumahara, Y., & Jayangondaperumal, R. (2013). Paleoseismic evidence of a surface rupture along the northwestern Himalayan Frontal Thrust (HFT). *Geomorphology, 180-181*, 47-56. http://dx.doi.org/10.1016/j.geomorph.2012.09.004

Kumar, S., Wesnousky, S. G., Rockwell, T. K., Ragona, D., Thakur, V. C., & Seitz, G. G. (2001). Earthquake recurrence and rupture dynamics of Himalayan Frontal Thrust, India. *Science, 294*, 2328–2331.

Kumar, S., Wesnousky, S. G., Rockwell, T. K., Briggs, R. W., Thakur, V. C., & Jayangondaperumal, R. (2006). Paleoseismic evidence of great surface rupture earthquakes along the Indian Himalaya. *Journal of Geophysical Research, 111*, B03304. doi:10.1029/2004JB003309

Kumar, S., Wesnousky, S. G., Jayangondaperumal, R., Nakata, T., Kumahara, Y., & Singh, V. (2010). Paleoseismological evidence of surface faulting along the northeastern Himalayan front, India: Timing, size, and spatial extent of great earthquakes. *Journal of Geophysical Research, 115*, B12422. http://dx.doi.org/10.1029/2009JB006789

Lavè, J., & Avouac, J. P. (2000). Active folding of fluvial terraces across the Siwaliks Hills, Himalayas of central Nepal. *Journal of Geophysical Research, 105*(B3), 5735-5770.

Lavè, J., & Avouac, J. P. (2001). Fluvial incision and tectonic uplift across the Himalayas of central Nepal. *Journal of Geophysical Research, 106*(B11), 26561-26591.

Lavé, J., Yule, D., Sapkota, S., Bassant, K., Madden, C., Attal, M., & Pandey, R. (2005). Evidence for a great medieval Earthquake (1100 AD) in the Central Himalayas, Nepal. *Science, 307*, 1302–1305.

Lienkaemper, J. J., & Bronk Ramsey, C. (2009). OxCal: versatile tool for developing paleoearthquake chronologies—a primer. *Seismological Research Letters, 80*(3), 431-434.

Malik, J. N., Sahoo, A. K., Shah, A. A., Shinde, D. P., Juyal, N., & Singhvi, A. K. (2010). Paleoseismic evidence from trench investigation along Hajipur fault, Himalayan Frontal Thrust, NW Himalaya: Implications of the faulting pattern on landscape evolution and

seismic hazard. *Journal of Structural Geology, 32*, 350-361. http://dx.doi.org/10.1016/j.jsg.2010.01.005

Malik, J. N., Naik, S. P., Sahoo, S., Okumura, K., & Mohanty, A. (2017). Paleoseismic evidence of the CE 1505 (?) and CE 1803 earthquakes from the foothill zone of the Kumaon Himalaya along the Himalayan Frontal Thrust (HFT), India. *Tectonophysics, 714-715*, 133-145. http://dx.doi.org/10.1016/j.tecto.2016.07.026.

Martin, S., Szeliga, W. (2010). A catalog of felt intensity data for 570 earthquakes in India from 1636 to 2009. *Bulletin of the Seismological Society of America*, *100*(2), 562–569.

Mishra, R. L., Singh, I., Pandey, A., Rao, P. S., Sahoo, H. K., & Jayangondaperumal, R. (2016). Paleoseismic evidence of a giant medieval earthquake in the eastern Himalaya. *Geophysical Research Letters, 43*. doi:10.1002/2016GL068739.

Mohan, K., Sharma, B., Mishra, O. P. (2023). Re-estimation of the location and size of the pre-instrumented 1 September 1803 Garhwal–Kumaon Himalaya earthquake: Evidence from site characterization and strong motion seismology. *Earth-Science Reviews*, *237*(104299), 1–29. https://doi.org/10.1016/j.earscirev.2022.104299.

Mugnier, J. L., Huyghe, P., Gajurel, A. P., & Becel, D. (2005). Frontal and piggy-back seismic ruptures in the external thrust belt of western Nepal. *Journal of Asian Earth Sciences*, *25*, 707-717.

Mugnier, J. L., Gajurel, A., Huyghe, P., Jayagondaperumal, R., Jouanne, F., & Upreti, B. (2013). Structural interpretation of the great earthquakes of the last millennium in the central Himalaya. *Earth Science Reviews, 127*, 30–47. http://dx.doi.org/10.1016/j.earscirev.2013.09.003.

Mukherjee S. (2015). A review on out-of-sequence deformation in the Himalaya. In: Mukherjee, S., Carosi, R., van der Beek, P., Mukherjee, B.K., Robinson, D. (Eds), Tectonics of the Himalaya. *Geological Society of London, 412*, 67-109.

Nakata, T., Kumura, K., & Rockwell, T. (1998). First successful paleoseismic trench study on active faults in the Himalaya. *EOS Transactions, 79*(45), F615.

Nanayama, F., Satake, K., Furukawa, R., Shimokawa, K., Atwater, B. F., Shigeno, K., & Yamaki, S. (2003). Unusually large earthquakes inferred from tsunami deposits along the Kuril trench. *Nature*,*424*(6949), 660–663. https://doi.org/10.1038/nature07572.

Pandey, M. R., & Tandukar, R. P. (1995). Interseismic strain accumulation on the Himalayan Crustal Ramp (Nepal). *Geophysical Research Letters, 22*(7), 751-754.

Pant, M. J. (2002). A step towards a historical seismicity of Nepal. *Adarsa, 2*, 29-60.

Philip, H., Rogozhin, E., Cisternas, A., Bousquet, C., Borisov, B., & Karakhanian, A. (1992). The Armenian earthquake of 1988 December 7: faulting and folding, neotectonics and palaeoseismicity. *Geeophys J Int, 110*, 141-158.

Philip, G., Bhakuni, S. S., & Suresh, N. (2012). Late Pleistocene and Holocene large magnitude earthquakes along Himalayan Frontal Thrust in the Central Seismic Gap in NW Himalaya, Kala Amb, India. *Tectonophysics, 580*, 162-177. http://dx.doi.org/10.1016/j.tecto.2012.09.012.

Rajendran, C. P., Rajendran, K., Sanwal, J., & Sandiford, M. (2013). Archeological and historical database on the medieval earthquakes of the central Himalaya: ambiguities and inferences. *Seismological Research Letters, 84*(6), 1098-1108. http://dx.doi.org/10.1785/0220130077.

Rajendran, C. P., John, B., & Rajendran, K. (2015). Medieval pulse of great earthquakes in the central Himalaya: Viewing past activities on the frontal thrust. *Journal of Geophysical Research: Solid Earth, 120*, 1623-1641. http://dx.doi.org/10.1002/2014JB011015.

Rajendran, C. P., Sanwal, J., John, B., Anandasabari, K., Rajendran, K., Kumar, P.,…Chopra, S. (2018). Footprints of an elusive mid-14th century earthquake in central Himalaya: Consilience of evidence from Nepal and India. *Geological Journal, 2018*, 1-18.

Rana, B. S. (1935). *Mahabhukampa*. Bhar Mahal BS 1992, Kathmandu, pp. 1-250.

Reimer, P. J., Bard, E., Bayliss, A., Beck, J. W., Blackwell, P. G., Bronk Ramsey, C.,… van der Plicht, J. (2013). IntCal13 and Marine13 Radiocarbon Age Calibration Curves 0-50,000 Years cal BP. *Radiocarbon, 55*(4).

Rundle, J. B., Kanamori, H. H., & McNally, K. C. (1984). An inhomogeneous fault model for gaps, asperities, barriers, and seismicity migration. *Journal of Geophysical Research, 89*, 10219-10231. http://dx.doi.org/10.1029/JB089iB12p10219.

Sapkota, S. N., Bollinger, L., Klinger, Y., Tapponnier, P., Gaudemer, Y., & Tiwari, D. (2013). Primary surface ruptures of the great Himalayan earthquakes in 1934 and 1255. *Nature Geoscience, 6*, 71-76. doi:10.1038/NGEO1669.

Shaw, B. E., & Dieterich, J. H. (2007). Probabilities for jumping fault segment stepovers. *Geophysical Research Letters, 34*, L01307. http://dx.doi.org/10.1029/2006GL027980.

Shennan, I., Bruhn, R., Plafker, G. (2009). Multi-segment earthquakes and tsunami potential of the Aleutian megathrust. *Quaternary Science Reviews*, *28*(1), 7–13. https://doi.org/10.1016/j.quascirev.2008.09.016.

Singh, I. B. (1996). Geological evolution of Ganga Plain - an overview. *Journal of the Palaeontological Society of India, 41*, 99–137.

Sinha, R., Friend, P. F., & Switsur, V. R. (1996). Radiocarbon dating and sedimentation rates in the Holocene alluvial sediments of the northern Bihar plains, India. *Geological Magazine*, *133*(1), 85–90. https://doi.org/10.1017/S0016756800007263.

Srivastrava, P., & Misra, D. K. (2012). Optically Stimulated Luminescence Chronology of Terrace Sediments of Siang River, Higher NE Himalaya: Comparison of Quartz and Feldspar Chronometers. *Journal Geological Society of India, 79*, 252-258.

Stevens, V. L., & Avouac, J. P. (2015). Interseismic coupling on the main Himalayan thrust. *Geophysical Research Letters, 42*, 5828-5837. http://dx.doi.org/10.1002/2015GL064845.

Stevens, V. L., & Avouac, J. P. (2016). Millenary M_w>9.0 earthquakes required by geodetic strain in the Himalaya. *Geophysical Research Letters, 43*, 1118-1123. http://dx.doi.org/10.1002/2015GL067336.

Storti, F., Salvini, F., McClay, K. (1997). Fault-related folding in sandbox analogue models of thrust wedges. *Journal of Structural* Geology, *19*(3–4), 583–602.

Thakur, V. C., Joshi, M., Sahoo, D., Suresh, N., Jayangondaperumal, R., & Singh, A. (2014). Partitioning of convergence in Northwest Sub-Himalaya: estimation of late Quaternary uplift and convergence rates across the Kangra reentrant, North India. *International Journal of Earth Sciences, 103*, 1037-1056. http://dx.doi.org/10.1007/s00531-014-1016-7.

Uchida, N., & Bürgmann, R. (2021). A decade of lessons learned from the 2011 Tohoku-Oki earthquake. *Reviews of Geophysics,* 59(e2020RG000713), 1–44. https://doi.org/10.1029/2020RG000713.

Uchida, N., Matsuzawa, T., Ellsworth, W. L., Imanishi, K., Okada, T., & Hasegawa, A. (2007). Source parameters of a M4.8 and its accompanying repeating earthquakes off Kamaishi, NE Japan: Implications for the hierarchical structure of asperities and earthquake cycle. *Geophysical Research Letters, 34*. https://doi.org/10.1038/nature07572.

Wesnousky, S. (2020). Great pending Himalaya Earthquakes. *Seismological Research Letters, 91*(6), 3334–3342.

Wyss, M., Gupta, S., & Rosset, P. (2018). Casualty estimates in repeat Himalayan earthquakes in India. *Bulletin of the Seismological Society of America, 108*(5A), 2877-2893. http://dx.doi.org/10.1785/0120170323.

Xiong, W., Tan, K., Qiao, X., Liu, G., Zhaosheng, N., & Yang, S. (2017). Coseismic, postseismic and interseismic coulomb stress evolution along the Himalayan Main Frontal Thrust since 1803. *Pure Applied Geophysics, 174*, 1889-1905. http://dx.doi.org/10.1007/s00024-017-1525-y.

Yadav, R. K., Gahalaut, V. K., Bansal, A. K., Sati, S. P., Catherine, J., Gautam, P.,…Rana, N. (2019). Strong seismic coupling underneath Garhwal-Kumaun region, NW Himalaya, India. *Earth and Planetary Science Letters, 506*, 8-14.

Yule, D., Dawson, S., Lave, J., Sapkota, S., & Tiwari, D. (2006). Possible evidence for surface rupture of the Main Frontal Thrust during the great 1505 Himalayan earthquake, Far-Western Nepal. *EOS Transactions,* 87(52).

Zhang, Z., & Klemperer, S. (2010). Crustal Structure of the Tethyan Himalaya, southern Tibet: new constraints from old wide-angle seismic data. *Geophysical Journal International, 181*, 1247-1260. doi: 10.1111/j.1365-246X.2010.04578.x

VITA

Robyn Lauren Daniels was born on August 31, 1975 in Kansas City, Missouri. She attended public schools in Lee's Summit, Missouri and graduated from Lee's Summit High School with an International Baccalaureate certificate in English in 1993. She received a Bright Flight Scholarship from the State of Missouri and attended Avila University from 1995-1997.

After working in her local community as an administrator for eleven years, Ms. Daniels enrolled at the University of Missouri-Kansas City (UMKC) in 2012 to complete her undergraduate degree. While pursuing her degree, Ms. Daniels worked as a student research assistant on a geologic mapping project and became an author on the map, which is published with the United States Geological Survey. She graduated summa cum laude from UMKC with a Bachelor of Science in Geology in 2014.

Following her graduation in August 2014, Ms. Daniels began a doctoral program in Geosciences and Chemistry at UMKC. While pursuing her Interdisciplinary Ph.D., she served as a Graduate Teaching Assistant in the UMKC Department of Geosciences and was hired as an Adjunct Instructor of structural geology for the department in the spring of 2019. During her graduate program, Ms. Daniels participated in the University of Missouri System's Graduate Student Leadership Development Program, became an author on a second geologic map published with the United States Geological Survey, published journal articles based on her research, and was awarded several research and travel grants that provided assistance for her research pursuits in northern India.

Ms. Daniels holds a Registered Geologist license with the State of Missouri and will begin teaching Geoscience courses at the University of Central Missouri in August, 2019. She is a member of the Geological Society of America, the American Geophysical Union, and the Association of Environmental and Engineering Geologists.